CHARACTERIZATION OF VADOSE ZONE IN-SITU MOISTURE CONTENT AND AN ADVANCING WETTING FRONT USING CROSS-BOREHOLE GROUND PENETRATING RADAR

by

LEE TAYLOR PAPROCKI

Submitted in Partial Fulfillment of the Requirements for the Degree of Master of Science in Hydrology

February 2000

New Mexico Institute of Mining and Technology
Socorro, New Mexico

ABSTRACT

The need for effective methods of containing and remediating contamination has become increasingly important as both our reliance on groundwater for drinking water and the occurrence of contaminated vadose zone sites has increased. Flow and transport within the vadose zone is dependent upon the in-situ moisture content distribution, which is often inadequately characterized by sparse hydrological measurements. Cross-borehole ground penetrating radar (GPR) is a high resolution, rapid-acquisition geophysical method that can obtain detailed measurements of the subsurface. Ground penetrating radar estimates the velocity of electromagnetic (EM) waves in the subsurface. This velocity can be converted to an image of moisture content since it depends primarily upon the moisture content (Topp et al., 1980).

At a vadose zone field site the feasibility of using cross-borehole GPR to image the 2-D in-situ moisture content distribution was tested. Then, during an infiltration experiment cross-borehole GPR was tested to see if it could accurately image the advancing wetting front. GPR measurements were taken along an 11-m profile consisting of five boreholes, with a 3-by 3-m infiltrometer in the center that emitted water at a rate of 2.7 cm/d. Two-dimensional GPR moisture content images were produced for pre-infiltration and infiltration conditions. The GPR images were compared to neutron moisture content measurements and to two stratigraphic columns. The neutron measurements were collected in the same five boreholes and the stratigraphic columns were constructed from continuous core samples taken several meters from the boreholes.

Overall, the GPR 2-D in-situ moisture content distribution image correlated well with the neutron probe and stratigraphic column data. By taking multiple data sets, one is able to quantify the GPR repeatability error. The average traveltime error was 1.08 ns which in a general sense translated to an average moisture content error of ± 2%. Both errors were calculated by taking two standard deviations. The overall error was highest in areas of high moisture content and low ray density. Results indicate that the GPR moisture content figures represent a smoothly varying image that maintains the general trend of the moisture content distribution as compared to the neutron probe and stratigraphic column data. Equipment failures led to inaccurate estimation of moisture content in at least two data sets. However, this study showed that cross-borehole GPR can be an effective and feasible technique for characterizing the vadose zone.

ACKNOWLEDGEMENTS

This Masters Thesis is dedicated to Norman Williams, a dear friend who always stressed the importance of higher education and encouraged me to strive to be my best. Thank you.

I'd like to thank the Department of Energy (DOE) who funded this project under the Environmental Science Management Program. I'd like to thank my advisors, Drs. David Alumbaugh, Robert Bowman, Harold Tobin, and Brian McPherson for their support and encouragement during the last two and a half years. I'd also like to thank Jim Brainard, Kristine Baker, Talon Newton, and Doug McGhee for their instrumental roles in this project, their support and most of all their sense of humor to carry on when things were not going well. Special thanks to Jim Brainard for his description of the field site. In addition, I would like to thank Greg Deickman for writing the neutron data reduction programs and installing my computer and the associated programs. Special thanks to Allan Gutjahr for his help with the neutron moisture content error analysis. I'd also like to acknowledge Chris Rautman for his design of the TDR calibration set-up and TDR data reduction programs and Frank Black for performing the TDR calibrations. Special thanks to Erwin Melis and Alana Furier for their help in editing my thesis. Thanks to my parents, sister, cousins, and friends for their encouragement. I couldn't have done it without you.

TABLE OF CONTENTS

	PAGE
ABSTRACT	**ii**
ACKNOWLEDGEMENTS	**iv**
TABLE OF CONTENTS	**v**
LIST OF FIGURES	**ix-xiii**
LIST OF TABLES	**xiv**
1. INTRODUCTION AND BACKGROUND ON GROUND PENETRATING RADAR	**1**
1.1 Introduction	1
1.2 GPR Theory and Description of System	3
1.2.1 General Theory	3
1.2.2 GPR Data Acquisition System	7
1.2.3 GPR Cross-Borehole Configuration and General Data Processing	8
1.3 GPR Literature Review	10
2. FIELD SITE CHARACTERISTICS AND INFILTRATION EXPERIMENT	**12**
2.1 Site Location and General Geology	12
2.2 Site layout and Instrumentation	15

2.3 Infiltration Experiment Description 18

3. TIME DOMAIN REFLECTOMETRY (TDR) AND NEUTRON PROBE CALIBRATION PROCEDURES AND RESULTS 20

3.1 TDR Calibration 20

3.1.1 TDR Calibration Description 20

3.1.2 TDR Calibration Processing Methods 23

3.1.3 TDR Calibration Results 23

3.1.4 Evaluation of Topp's Equation 24

3.2 Neutron Probe Calibration Procedure and Results 29

3.2.1 Neutron Probe Calibration 29

3.2.2 Neutron Calibration Location, Instrument Set-up, and Procedure 30

3.2.3 Neutron Probe Calibration Results 31

3.3 TDR and Neutron Probe Error Analysis 33

4. NEUTRON AND GPR DATA ACQUISITION AND PROCESSING METHODS 36

4.1 Neutron Probe Data Acquisition and Processing Methods 36

4.1.1 Neutron Probe Data Acquisition Procedure 36

4.1.2 Neutron Data Processing Methods 36

4.1.3 Neutron Acquisition Schedule 37

4.2 GPR Data Acquisition and Processing Methods 37

4.2.1 GPR Data Acquisition Procedure 37

4.2.2 GPR Data Processing Methods 40

4.2.3 GPR Data Acquisition Schedule 42

4.2.4 GPR Instrument Problems 42

5. PRE-INFILTRATION RESULTS AND DISCUSSION 44

5.1 GPR Raw Image Results and Discussion 44

5.1.1 GPR Raw Image Results 44

5.1.2 GPR Discussion 47

5.2 Comparison of Neutron and GPR Moisture Content Results and Discussion 49

5.3 GPR Ray Density and Error Analysis 52

5.3.1 GPR Ray Density 52

5.3.2 GPR Error Analysis Results 54

6. INFILTRATION RESULTS AND DISCUSSION 60

6.1 Infiltration Schedule 60

6.2 GPR Raw Image Results and Discussion 60

6.3 GPR Normalized Image Results and Discussion 64

6.4 GPR Ray Density Image Results and Discussion 69

6.5 Comparison of GPR and Neutron Moisture Content Images 73

7. CONCLUSIONS AND RECOMMENDATIONS 88

8. REFERENCES 91

APPENDIX 1: Northwest Core Particle Size Analysis Results 93

APPENDIX 2: Neutron Moisture Content Error Analysis Derivation and Calculations 95

APPENDIX 3: Neutron Probe Operating and Downloading Procedure 105

APPENDIX 4: Four GPR Pre-Infiltration Ray Density Images 109

APPENDIX 5: GPR Moisture Content Images: Mean Pre-Infiltration Image and Seven Infiltration Images Processed without a Time Shift 113

APPENDIX 6: GPR Normalized Moisture Content Infiltration Images Processed without a Time Shift 117

LIST OF FIGURES

		Page
Figure 1a-b.	Schematic depiction of a) the real (K′) and the b) imaginary (K″) components of the dielectric constant versus frequency.	6
Figure 2.	GPR cross-borehole configuration.	9
Figure 3.	Map of New Mexico with Socorro County highlighted.	13
Figure 4.	Stratigraphic columns from the field site.	14
Figure 5.	Site layout (plan view).	16
Figure 6.	Picture of the instrumented site, infiltrometer, and neutron calibration area.	17
Figure 7.	Close-up picture of the infiltrometer.	19
Figure 8.	Picture of the TDR calibration set-up.	21
Figure 9.	Apparent dielectric constant versus moisture content for four wetting experiments and one drainage experiment for TDR probe 1.	25
Figure 10.	Apparent dielectric constant versus moisture content for three wetting experiments and one drainage experiment for TDR probe 2.	25
Figure 11.	Apparent dielectric constant versus moisture content for three wetting experiments and one drainage experiment for TDR probe 3.	26
Figure 12.	Apparent dielectric constant versus moisture content for all three drainage experiments.	26
Figure 13.	Graphical comparison of measured moisture content versus Dielectric constant and that predicted by Topp's equation for TDR probe 1.	27

Figure 14.	Graphical comparison of measured moisture content versus Dielectric constant and that predicted by Topp's equation for TDR probe 2.	27
Figure 15.	Graphical comparison of measured moisture content versus Dielectric constant and that predicted by Topp's equation for TDR probe 3.	28
Figure 16.	Neutron probe calibration layout	30
Figure 17.	Neutron calibration equation: moisture content versus neutron count ratio.	32
Figure 18.	Regression error analysis.	34
Figure 19.	Schematic of 45-degree GPR acquisition angle.	39
Figure 20a-f.	GPR pre-infiltration moisture content images.	45-46
Figure 21.	GPR mean pre-infiltration image with geologic interpretation based upon stratigraphic column data.	48
Figure 22.	GPR mean pre-infiltration moisture content image with neutron moisture logs superimposed on image.	50
Figure 23.	GPR and neutron probe pre-infiltration moisture content measurements versus depth for access tube B.	51
Figure 24.	Ray density image for GPR pre-infiltration data taken on 11/24/98.	53
Figure 25a-d.	Pre-infiltration travel time error analysis for well pairs AB, BC, CD, and DE.	56-57
Figure 26.	Moisture content error analysis: two standard deviations for five pre-infiltration GPR moisture content images.	59

Figure 27a-i. GPR moisture content images: mean pre-infiltration to 119 days after infiltration began. 61-63

Figure 28a-h. GPR normalized moisture content images 8 to 119 days after infiltration began. 65-67

Figure 29a-h. GPR ray density images: mean pre-infiltration to 119 days after infiltration began. 70-72

Figure 30. GPR moisture content image after 8 days of infiltration with neutron moisture logs superimposed on image. 74

Figure 31. GPR moisture content image after 14 days of infiltration with neutron moisture logs superimposed on image. 77

Figure 32. GPR moisture content image after 21 days of infiltration with neutron moisture logs superimposed on image. 78

Figure 33. GPR moisture content image after 28 days of infiltration with neutron moisture logs superimposed on image. 79

Figure 34. GPR moisture content image after 35 days of infiltration with neutron moisture logs superimposed on image. 80

Figure 35. GPR moisture content image after 42 days of infiltration with neutron moisture logs superimposed on image. 81

Figure 36. GPR moisture content image after 119 days of infiltration with neutron moisture logs superimposed on image. 82

Figure 37. GPR and neutron moisture content measurements versus depth in access tube B after 8 days of infiltration. 84

Figure 38. GPR and neutron moisture content measurements versus depth in access tube B after 14 days of infiltration. 84

Figure 39. GPR and neutron moisture content measurements versus depth in access tube B after 21 days of infiltration. 85

Figure 40. GPR and neutron moisture content measurements versus depth in access tube B after 28 days of infiltration. 85

Figure 41. GPR and neutron moisture content measurements versus depth in access tube B after 35 days of infiltration. 86

Figure 42. GPR and neutron moisture content measurements versus depth in access tube B after 42 days of infiltration. 86

Figure 43. GPR and neutron moisture content measurements versus depth in access tube B after 119 days of infiltration. 87

Figure A.1. Ray density image for GPR pre-infiltration data set taken on 1/22/99. 109

Figure A.2. Ray density image for GPR pre-infiltration data set taken on 2/1/99. 110

Figure A.3. Ray density image for GPR pre-infiltration data set taken on 2/11/99. 111

Figure A.4. Ray density image for GPR pre-infiltration data set taken on 2/1/899. 112

FigureA.5.a-h. GPR moisture content images: pre-infiltration to 119 days after infiltration began (no time shift applied). 114-116

Figure A.6a-g. GPR normalized moisture content images 8-119 days after Infiltration began (no time shift applied). 118-120

LIST OF TABLES

	Page
Table A-1. Northwest core particle size analysis in percent weight	94
Table A-2. Neutron measurements and variance calculations	95-96
Table A-3. TDR measurements	97-101
Table A-4a-c. Regression Analysis Summary Output	102

1.0 INTRODUCTION AND BACKGROUND ON GROUND PENETRATING RADAR

1.1 Introduction

Due to our increasing reliance on groundwater for drinking water and agriculture, groundwater contamination has become a major concern. In semi-arid environments, like New Mexico, contaminants enter the subsurface and travel through the vadose zone before reaching the water table. The vadose zone encompasses the area between the soil surface and the groundwater table, and in semi-arid environments can be ten to several hundred meters thick. To ensure that contamination does not reach the water table, effective remediation or containment techniques need to be employed within the vadose zone. Both remediation and containment techniques require an understanding of water movement and contaminant transport in the vadose zone.

In the absence of a contaminant, the presence of both air and water within the pores of a porous medium determine water movement. In saturated conditions, where the pores are filled only with water, flow is governed by the saturated hydraulic conductivity and the hydraulic gradient. In unsaturated conditions however, the unsaturated hydraulic conductivity is a function of the moisture content and the saturated hydraulic conductivity. Thus, to design effective remediation and/or containment techniques in heterogeneous vadose zones, a detailed characterization of the in-situ moisture content distribution is needed. The spatial distribution of this property is often estimated from measurements of samples collected at a limited number of boreholes. The results are then extrapolated across the region of interest using geostatistical techniques. This leads to fairly detailed knowledge of how the moisture content varies with depth, but little

information on how it varies laterally. Also, the sampling process often disturbs the material which can lead to inaccurate measurements.

A non-destructive technique for estimating the in-situ moisture content within the vadose zone, could lead to accurate estimates of water movement and to effective designs of waste containment and/or remediation methods. Ground penetrating radar (GPR) is a high resolution, rapid-acquisition geophysical method that can obtain detailed estimates of the electromagnetic (EM) wave velocity within the earth. The EM wave velocity depends primarily upon the moisture content (Topp et al., 1980). Thus, GPR measurements can be used to produce images that describe the two-dimensional distribution of the in-situ moisture content.

The Department of Energy (DOE) is investigating techniques to effectively contain and/or remediate contamination at numerous DOE sites in the arid Western U.S. Therefore, they have funded a project designed both to characterize the vadose zone and monitor contaminant transport. A hydrologic-geophysical inverse technique for characterizing the vadose zone is being developed and field-tested using field data combined with statistical information about the geologic formations. A highly instrumented field site was developed along with a controlled water application system. My specific role within this project was to test the feasibility of using cross-borehole GPR to image the subsurface moisture content at the field site. The project was divided into two main parts, including characterization of the site before water application or pre-infiltration, and during water application or infiltration. My specific pre-infiltration objectives were to: 1) image the 2-D in-situ moisture content distribution along a transect; 2) compare the in-situ GPR results with stratigraphic and neutron probe data;

and 3) determine the precision error of GPR moisture content measurements by using five pre-infiltration data sets. GPR measurements were compared to neutron measurements since neutron probe measurements are an accepted and common method of measuring moisture content (Wilson et al., 1995). My objectives during water infiltration were to: 1) use GPR to image the 2-D progression of water movement as a result of water infiltration; and 2) compare GPR image results with neutron measurements.

In the next section of this chapter, general GPR theory, the GPR data acquisition system, and a review of recent advancements in the application of GPR are discussed. In chapter 2, a description of the field site, instrumentation, and infiltration system are presented. In chapter 3, calibration procedures and results for time domain reflectometery (TDR) probes and the neutron probe are described. In chapter 4, neutron and GPR data acquisition and processing procedures are outlined. Chapter 5 contains GPR pre-infiltration moisture content images and comparisons of GPR images to stratigraphic column and neutron probe data. Chapter 6 presents GPR and neutron infiltration results. Finally, chapter 7 presents conclusions and recommendations for future work.

1.2 GPR Theory and Description of System

1.2.1 General Theory

Ground penetrating radar measures the travel time of an electromagnetic wave traveling through a porous medium or air. The velocity of the wave is primarily controlled by the medium's dielectric constant. Since the dielectric constant is a function of the water content of the medium, GPR measurements can image the in-situ moisture content distribution of the vadose zone.

The following discussion of GPR theory relies heavily upon Annan (1999) and Davis and Annan (1989) and the reader is referred to these sources for additional information.

The GPR system transmits a pulse of high-frequency electromagnetic energy, between 10-200 MHz, through the air and the ground. The wave velocity depends primarily upon the electrical properties of the medium. However, in some cases where magnetic minerals are present, the magnetic permeability can affect the EM wave velocity (Annan, 1999). The electrical properties that influence the velocity and attenuation of the propagating wave are the dielectric permittivity and the electrical conductivity respectively. In response to an applied electric field, a displacement current is created whose magnitude is determined by the dielectric permittivity. A displacement current stores energy in an applied electric field and releases it when the electric field is no longer applied. Hence in a high frequency varying field, the displacement currents cause EM energy to propagate as a wave. An applied electric field also causes free ions to move as a result of the electrical conductivity of the porous medium. The movement of ions results in the dissipation of energy in the form of heat. According to Maxwell's equations, at typical GPR frequencies (10-200 MHz), the dielectric properties dominate over the conductive properties in the transfer of the EM energy (Davis and Annan, 1989).

The dielectric permittivity is a proportionality constant that relates the application of an electric field to the creation of a dipole moment as illustrated mathematically in the equation below:

$$D = \varepsilon * E \qquad (1)$$

where D is the dipole moment density ($F*V/m^2$), ε is the material dielectric permittivity (F/m), and E is the applied electric field (V/m). The dielectric constant (K), expressed below, is a ratio of the material dielectric permittivity to the permittivity in a vacuum, ε_o (8.85×10^{-12} F/m):

$$K = \varepsilon/\varepsilon_o \quad (2)$$

The dielectric constant is actually a complex number composed of real and imaginary parts as expressed below:

$$K = K' - i[K'' + (\sigma_{dc} / \omega\varepsilon_o)] \quad (3)$$

where K′ is the real part of the dielectric constant (also called the apparent dielectric constant), K″ is the imaginary part of the dielectric constant (also called the dielectric loss factor), σ_{dc} (S/m) is the electrical conductivity of the porous medium, and ω (1/sec) is the angular frequency. The real and imaginary dielectric "constants" are not true constants, because their values vary with frequency (Figure 1a and b). However, for frequencies used in GPR (10^9 Hz) the real part of the dielectric constant is essentially invariant and the imaginary part of the dielectric constant is very small (Hasted, 1972). Therefore, GPR primarily measures the real part of the dielectric constant.

Highly conductive porous media (>100 mS/m) and dissolved electrolytes in pore water both induce dielectric losses. However, for most porous media, at high frequencies, the dielectric loss due to the electrical conductivity (<100 mS/m) is considered insignificant (Davis and Annan, 1989). In this study, the electrical conductivity of the porous medium did not contribute to significant dielectric losses (i.e. signal attenuation), since I was able to obtain high quality signals using 100MHz antennas, with borehole

separation of several meters. In addition, the electrolyte concentration in most uncontaminated porous medium has a minor effect on dielectric properties (Wilson et al., 1995). Therefore, dielectric losses due to the electrical conductivity of the porous medium and the electrolyte concentration in the pore water can usually be ignored.

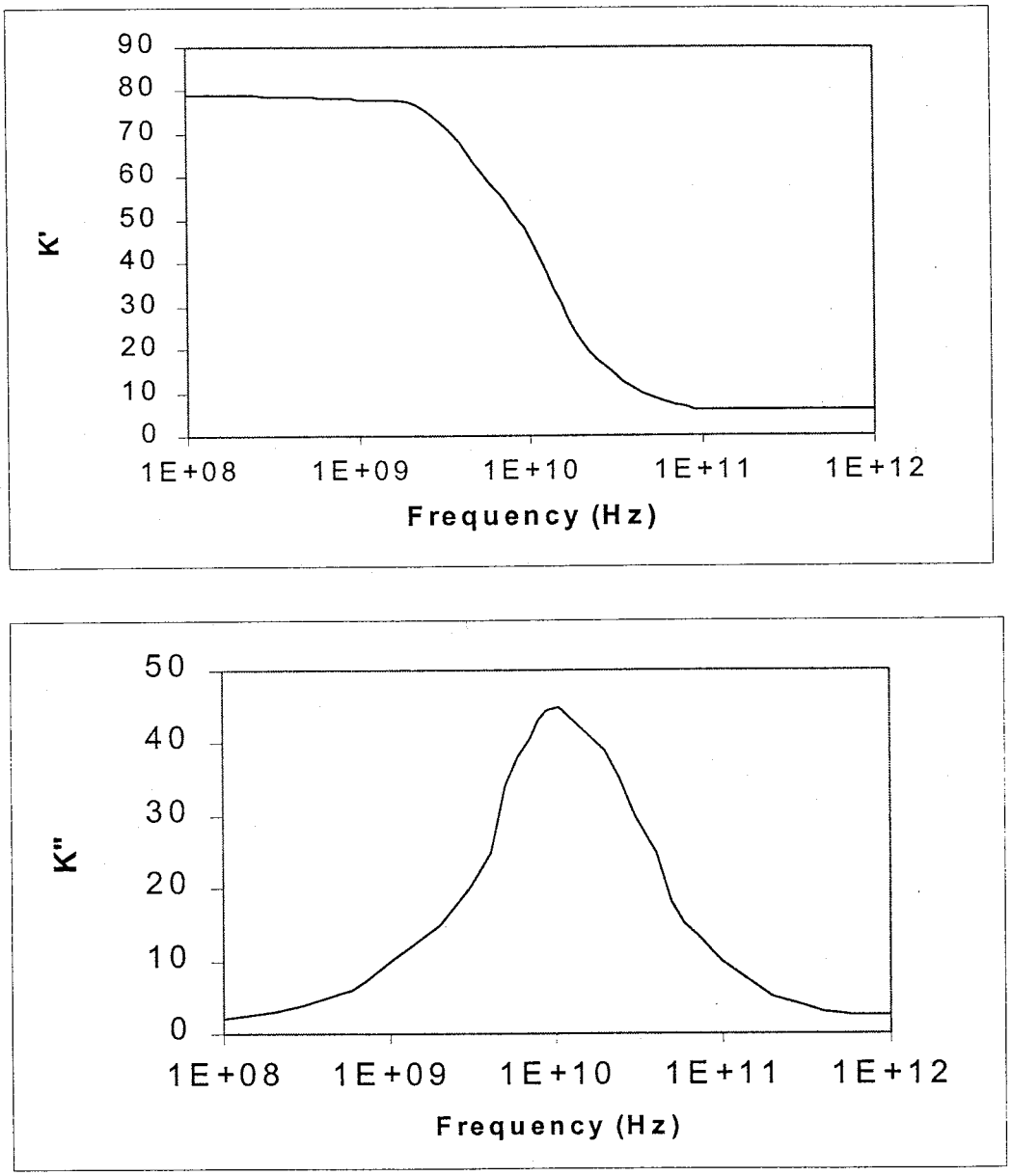

Figure 1. Schematic depiction of a) the real (K') and b) the imaginary (K'') components of the dielectric constant versus frequency (after Wilson et al., 1995)

The EM velocity is inversely related to the dielectric constant as illustrated by the following equation, assuming no magnetic minerals are present within the porous medium:

$$v = c / (K' * (1 + \{1 + \tan^2 \delta\}^{1/2})/2)^{1/2} \quad (4)$$

where $\tan \delta = \{K'' + (\sigma_{dc}/\omega\varepsilon_o)\}/ K'\}$, c is the velocity of light in a vacuum ($K'=1$), and v is the EM velocity of the medium. Both c and v have dimensions of m/ns. Tan δ represents the electric loss to the porous medium.

In practice, equation 4 is often simplified to

$$K' \cong (c/v)^2 \quad (5)$$

by making the assumption that in most porous media, tan δ is less than 1, and therefore becomes insignificant (Topp et al., 1982).

The EM velocity is predominantly influenced by the water content in porous media due to the large contrast between the apparent dielectric constant of water (80) and that of dry porous media (4-8) (Topp et al., 1980). GPR is an ideal method to image the in-situ moisture distribution within a porous medium because of this large dielectric contrast.

1.2.2 GPR Data Acquisition System

The GPR system consists of a transmitting unit, a receiving unit, two antennas, a data acquisition computer, and a console or control unit that connects the GPR network. The transmitter and receiver are connected to the console by fiber optic cables. Fiber optic cables are non-conductive fibers that reduce noise generated from electromagnetic coupling of the GPR signal to metal connection cables. GPR can be employed in one of three ways: reflection profiling mode, sounding mode (wide-angle reflection or common

midpoint mode), and in transillumination mode, otherwise known as cross-borehole configuration.

1.2.3 GPR Cross-Borehole Configuration and General Data Processing

For this experiment the GPR system has been employed in the cross-borehole configuration. In this configuration two antenna probes, a transmitter and a receiver, are placed in two separate boreholes several meters apart (Figure 2). A pulse is transmitted from the transmitter and measured by the receiver. The transmitter position remains constant while the receiver is lowered down at fixed depth intervals until the bottom of the borehole is reached. The transmitter position is then moved down one depth interval and the process is repeated. For a given transmitter-receiver pair, the datum of interest is the travel time of the direct wave from the transmitter to the receiver. The first arrivals, or EM wave travel times, are 'picked' and the travel time data inverted to produce an image of the EM wave velocity. By making measurements of the travel time for multiple transmitter and receiver pairs, the 2-D velocity distribution between boreholes can be tomographically reconstructed. A curved ray inversion scheme is often used for heterogeneous environments in order to more accurately model the physics of the ray paths as they curve around areas of low velocity (Bregman et al., 1989).

Once the velocity profile is created, it is converted to a profile of dielectric constant via equation 5. Next, the dielectric values are converted to moisture content. A commonly used empirical relationship between dielectric constant and moisture content was developed by Topp et al., (1980). The relationship was derived by making laboratory measurements of the dielectric constant on a number of different sand and clay samples over a wide range of water saturations, and then fitting the resulting data with a third-

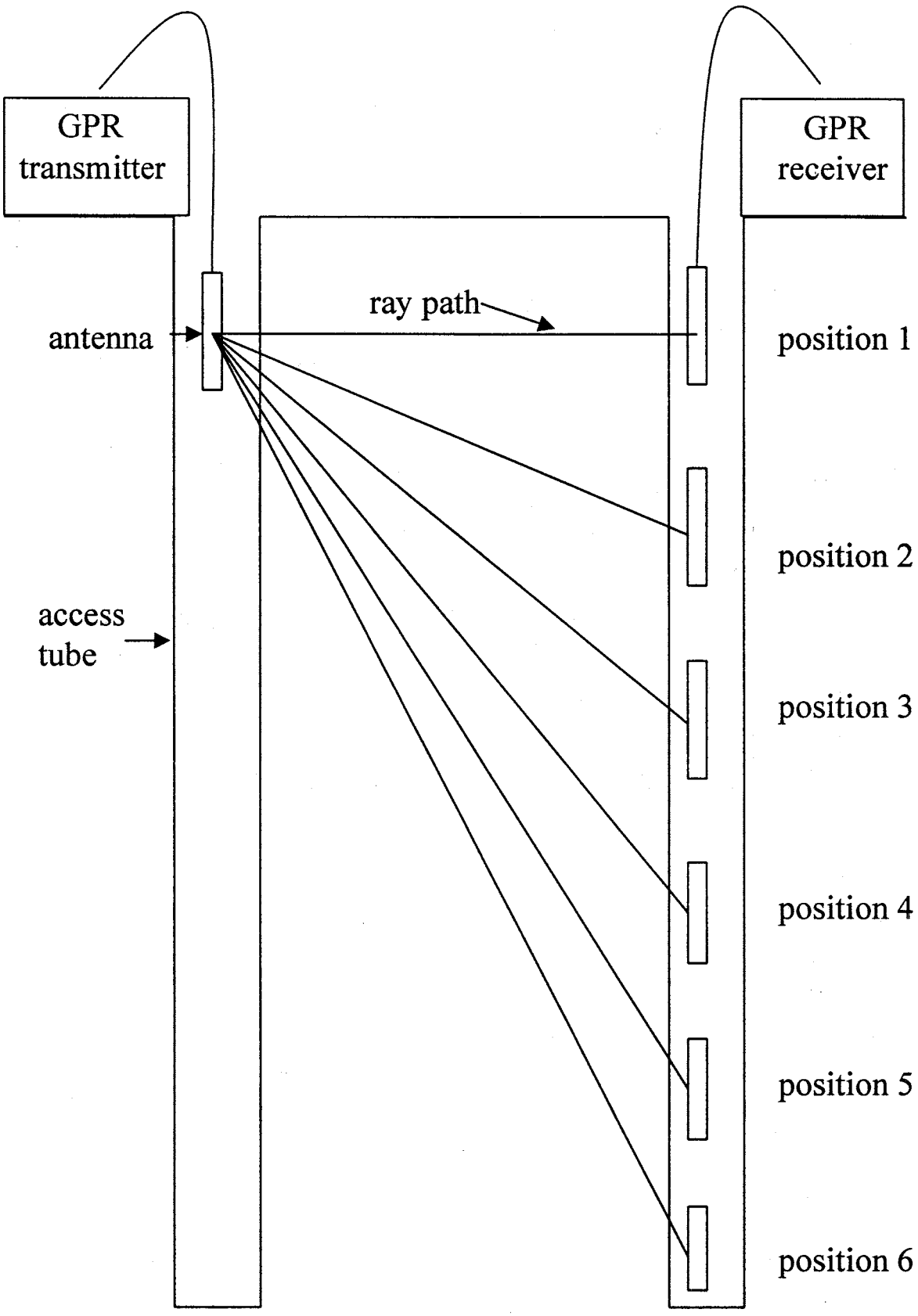

Figure 2. GPR cross-borehole configuration

order polynomial. Topp's equation is given as:

$$\theta = -5.3\text{x}10^{-2} + 2.9\text{x}10^{-2}*K' - 5.5\text{x}10^{-4}*K'^2 + 4.3\text{x}10^{-6}*K'^3 \quad (6)$$

where θ is moisture content. Note that this expression becomes zero for $K' \cong 1.8$. An advantage of Topp's equation over other dielectric constant-moisture content relationships is that no prior geological information of the porous medium is needed. However, as will be discussed in section 3.1.4, Topp's equation is not accurate for all situations.

1.3 GPR Literature Review

Using GPR to obtain in-situ moisture content is a relatively new application. Eppstein and Dougherty (1998) have used cross-borehole GPR to image relative moisture changes in three dimensions by comparing velocity changes before and after an infiltration event. Greaves et al. (1996) utilized the GPR common midpoint profiling geometry to measure the interval velocity and then converted to moisture content using three different relationships; Topp's equation, the complex refractive index method (CRIM) equation, and the Hanai-Bruggerman mixing formula. Hubbard et al. (1997) discussed the use of surface GPR data along with conventional hydrological data to obtain better estimates of saturation, permeability, and hydraulic conductivity. Rea and Knight (1998) utilized surface GPR in conjunction with geostatistics to image the heterogeneity of a porous medium. Chanzy et al. (1996) employed surface and airborne GPR to develop a relationship between GPR trace amplitudes and soil moisture. Van Overmeeren et al. (1997) used surface GPR to obtain in-situ moisture contents which compared well with capacitance probe moisture content results. They obtained detailed vertical moisture content resolution but lacked detailed lateral resolution. Lesmes et al.

(1999) compared surface GPR moisture content measurements, converted to moisture content via Topp's equation, to TDR and gravimeteric water content measurements. They found GPR values were consistently lower than the moisture content measurements obtained from the other two techniques.

Until now cross-borehole GPR has not been thoroughly examined as a method to estimate the absolute in-situ moisture content. The main goals of this thesis were to test the feasibility of cross-borehole GPR both to estimate the in-situ moisture content distribution and image an advancing wetting front produced during water infiltration.

2.0 FIELD SITE CHARACTERISTICS AND EXPERIMENTAL DESIGN

2.1 Site Location and General Geology

In order to test the effectiveness of a hybrid hydrologic/geophysical inverse technique for developing estimates of hydraulic properties within a heterogeneous vadose zone, a field test site was established in Socorro, New Mexico. Socorro is located 75 miles south of Albuquerque, New Mexico. (Figure 3). The field site has been mapped as part of the Sierra Ladrones Formation, Upper Santa Fe Group and consists of unconsolidated, heterogeneous, fluvial facies (Hawley, 1983). Figure 4 shows four stratigraphic columns, constructed from fur 13-m continuous cores. The locations of the core samples are shown in Figure 5 and a partial particle size analysis of the Northwest core is presented in Appendix 1. Complete particle size analysis is a work in progress at Sandia National Labs (Brainard et al., personal communication, 2000). The cores were drilled by a hollow-stem auger using a CME 75 high torque drill rig with a 6 1/4″ ID x 5′ length split spoon sampler and a 10 1/2″ bit. The area is primarily composed of alternating layers of sand, silt, gravel, and clay (Figure 4). The upper 2-m consists of a continuous coarse sand and gravel layer. A continuous fine sand layer follows at a depth of approximately 2 to 3.5 m. A poorly sorted silt, sand, and clay nodule layer underlies the sand to a depth of 4.8 m. The poorly sorted layer is thickest in the north but thins to the southwest and is underlain by a thin layer of fine sand from 5 to 5.5-m depth. A clay-matrix-supported conglomerate underlies the fine sand layer but this layer is discontinuous in the northeast area of the field site based on the limited data from the stratigraphic column. A thick fine sand layer occurs from 6 to 13-m depth.

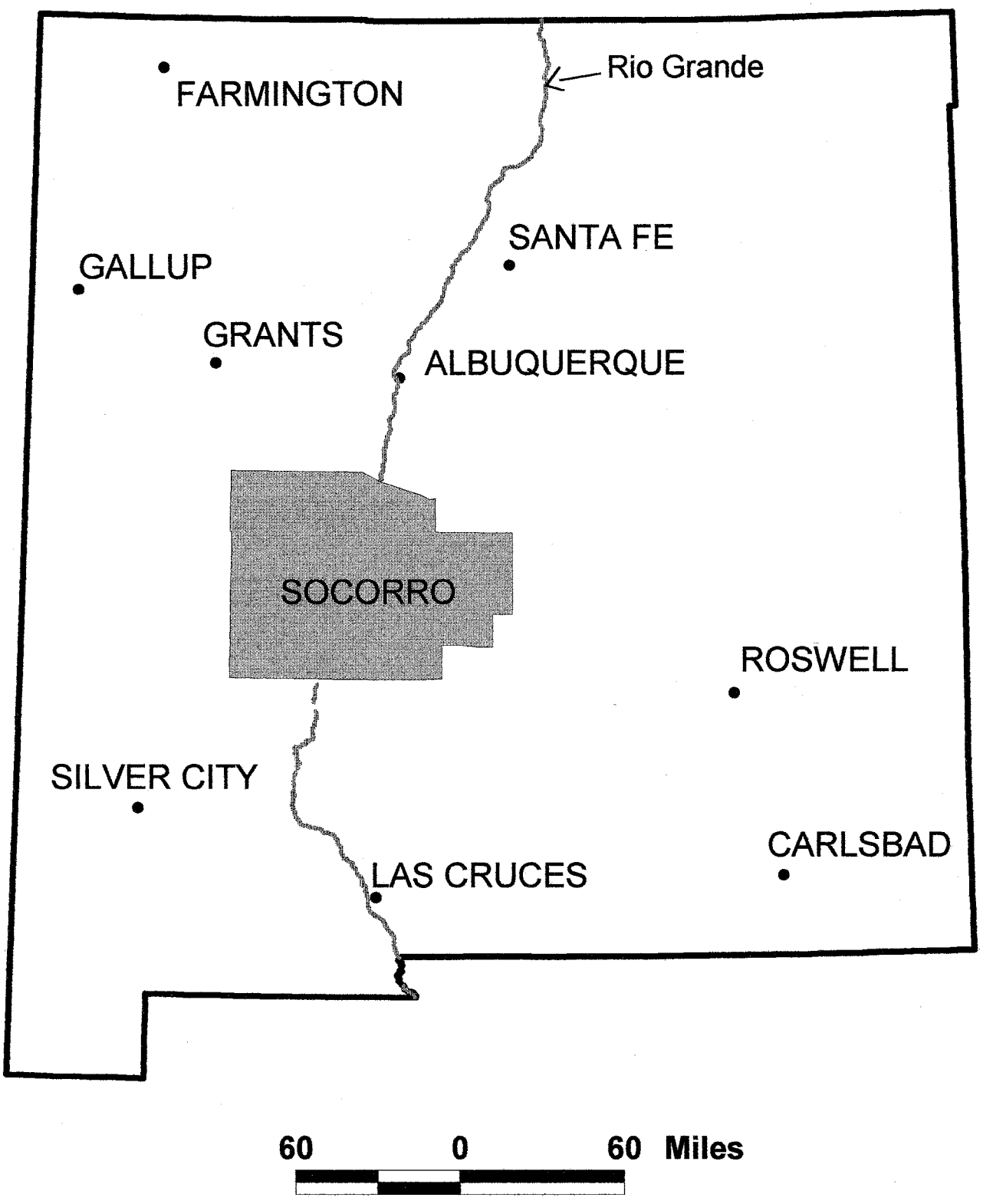

Figure 3. New Mexico State location map with Socorro County highlighted

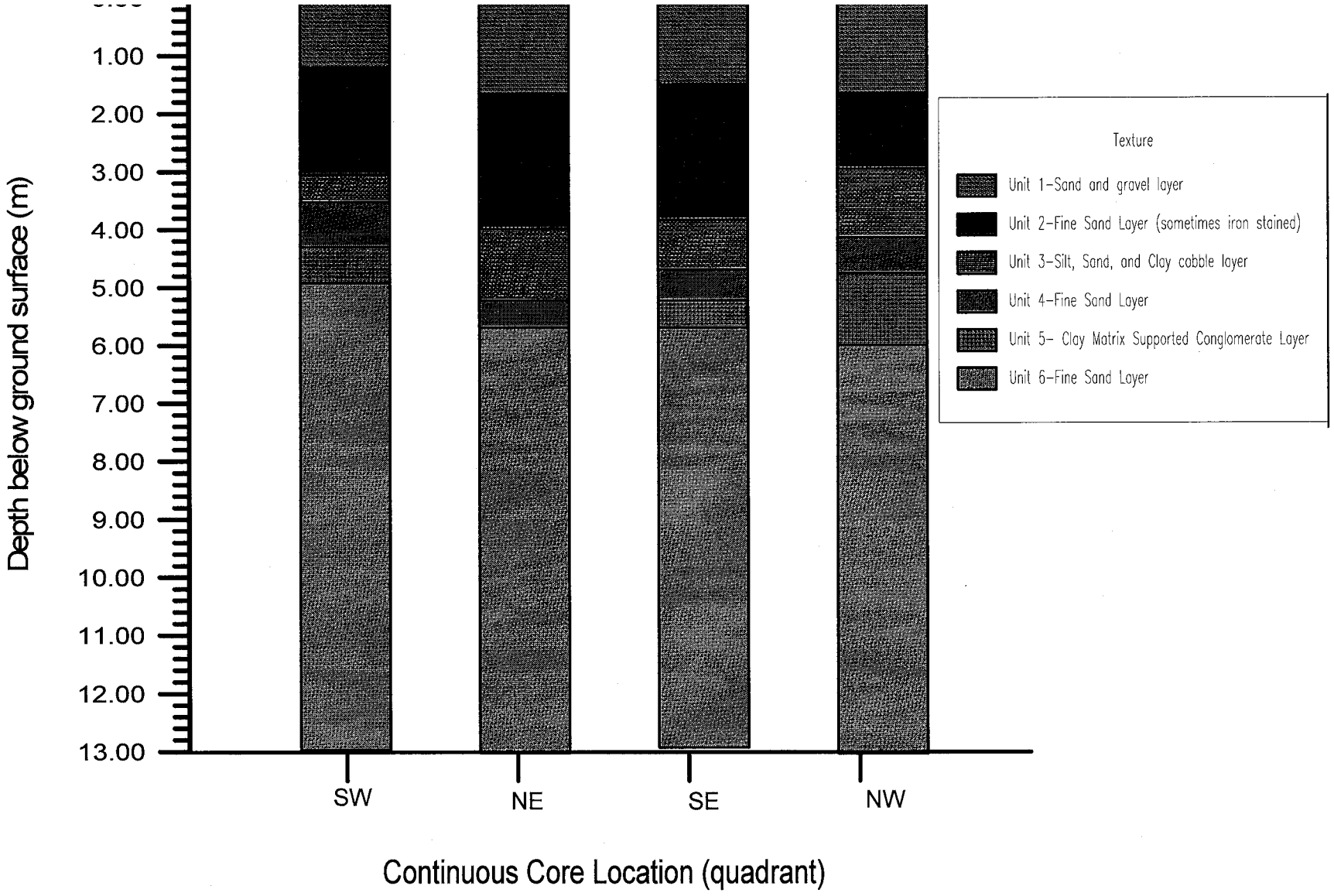

Figure 4. Stratigraphic columns from field site, constructed from continuous core samples

2.2 Site Layout and Instrumentation

The dimensions of the site are approximately 10 m by 10 m. Thirteen PVC-cased subsurface access tubes were emplaced to a maximum depth of 13 m (Figures 5 and 6). The boreholes were drilled with a small drill rig from the NM Bureau of Mines and Mineral Resources using 4-in and 6-in diameter flight augers. The 6-in auger was used in the upper 3 m to penetrate the upper gravel layer. Once past the gravels, the 4-in auger was used for the remaining depths. Two-inch PVC tubes were installed in the boreholes and the annulus was backfilled with sifted sand. Gravel was backfilled in the annulus around the access tubes at the approximate depth of the gravel layer to mimic the existing stratigraphy. The center access tube annulus was backfilled with a 20% bentonite mix from the surface to depth of 1 m. Bentonite was used in order to prevent preferential flow down the access tube during water infiltration.

Ground penetrating radar measurements were taken in five access tubes along a southwest to northeast diagonal (Figures 5 and 6). The GPR access tubes were labeled A through E from the southwest to the northeast (Figure 6). Neutron probe measurements were taken in all 13 PVC access tubes. Other instruments were installed symmetrically around the center of the site and include tensiometers, time domain reflectometry (TDR) probes, and soil suction samplers. In addition to the GPR, 3-D electrical resistivity tomography (ERT) measurements were employed to estimate moisture content. The ERT system consisted of electrodes emplaced at the surface and to a maximum depth of 13-m (Figure 5). A data acquisition building was built on site to: 1) connect the hydrological instrument and ERT cables to automatic data collection systems; 2) house computers for downloading and processing data; and 3) store tanks that provided water for infiltration.

An infiltration system was installed at the center of the site and provided a pulsed constant flux boundary condition (refer to description of infiltrometer that is given below.)

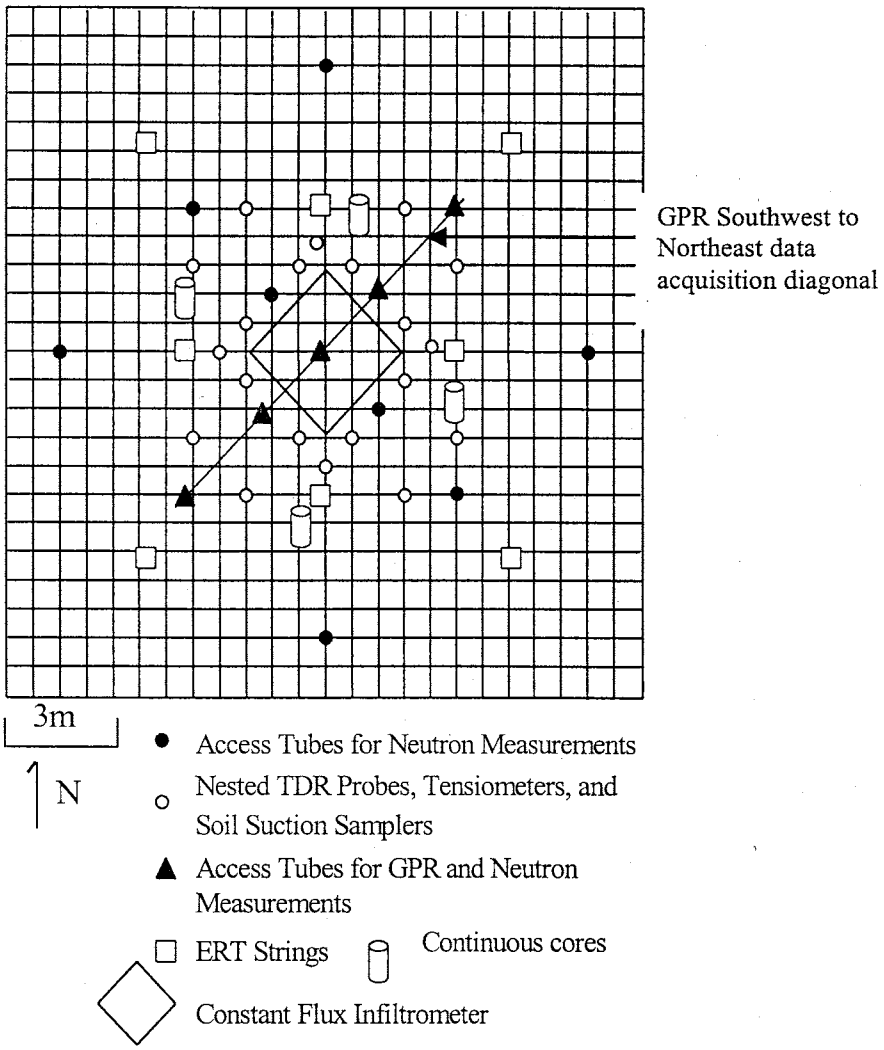

Figure 5. – Site layout (plan view) showing the locations of the hydrologic instruments, the continuous core samples, and boreholes used for neutron and cross-borehole GPR measurements.

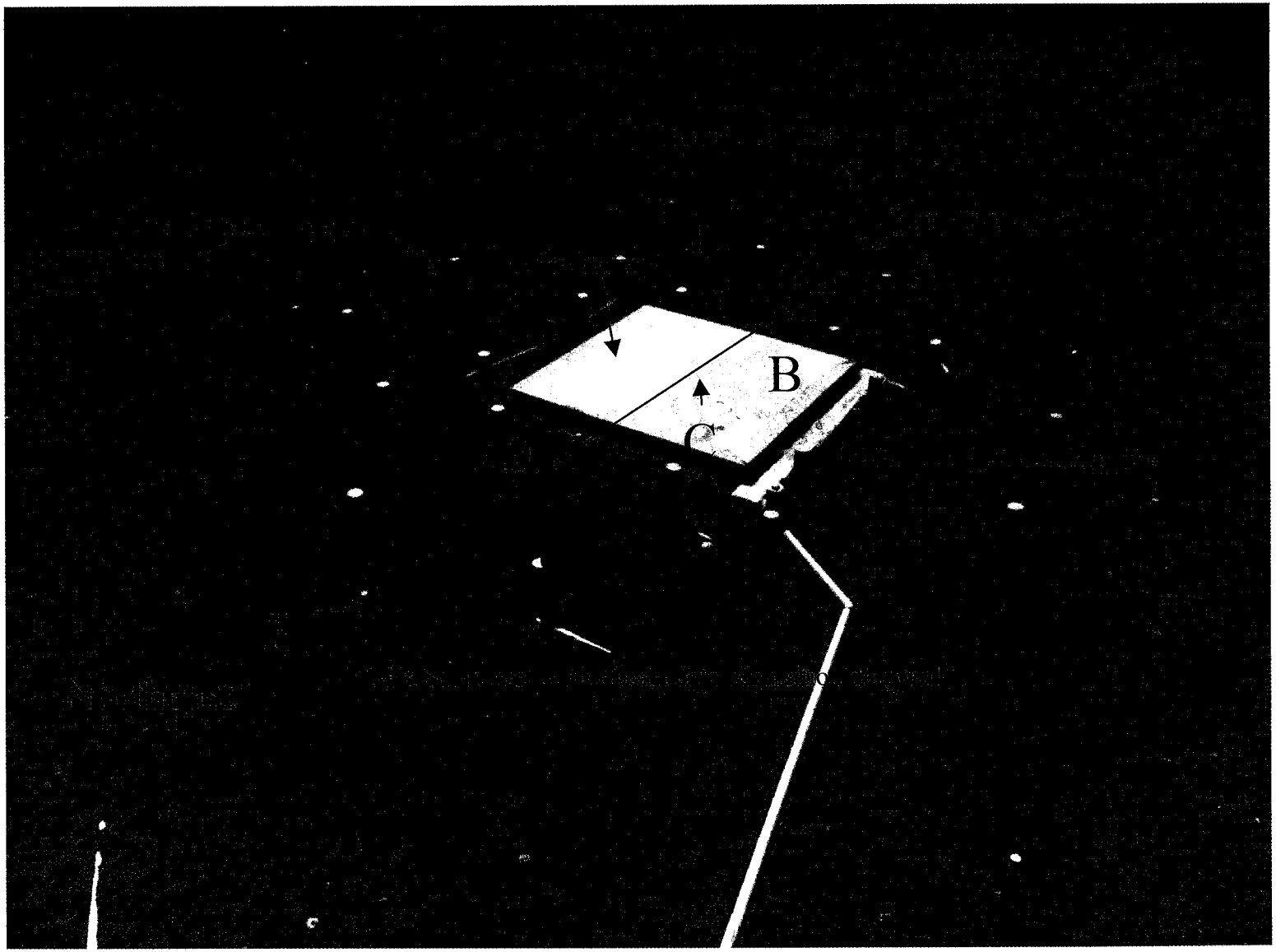

Figure 6. Picture of the instrumented site, infiltrometer and neutron calibration area. Also labeled is the diagonal along which GPR data is taken and the individual GPR access tubes (access tube C is underneath the white tarp). (picture taken by Jim Brainard)

2.3 Infiltration Experiment Description

The infiltration system or infiltrometer consisted of a square infiltration pad measuring 3 m on a side (Figure 7). The infiltrometer was further divided into 9 arrays each measuring $1m^2$. Each array contained a network of ½ " PVC pipes with 100 equally spaced 18-gauge stainless steel medical needles drilled into the pipes to distribute the water evenly. There are a total of 900 equally spaced needles over a $9m^2$ area, or 1 needle per $.01m^2$. The infiltrometer was constructed out of 2" by 12" treated lumber forming the exterior walls and interior dividers for supporting the arrays. The top of the infiltrometer was covered with 10 cm of structural insulating foam and a PVC tarp to minimize evaporation or infiltration from precipitation.

The flow rate of each infiltration array was monitored by a flow meter while pressure regulators installed in each line provided the ability to adjust flow rates to each array independently. The water supply system was housed within the data acquisition building and consisted of two 0.757 m^3 (200 gallon) water supply tanks, a shallow-well pump that supplies water to a diaphragm pressure tank, and a timer that controlled two in-line heavy duty solenoid valves. Water flow rates from the supply tanks were monitored with pressure transducers installed in the bottom of each of the tanks and with flow meters in the infiltration array supply lines. Outside of the infiltrometer, a no-flow top boundary condition was established by overlaying the whole site with a PVC tarp and 15 cm of sand to eliminate both evaporation and infiltration from precipitation.

Before infiltration began, instruments were calibrated and background data sets were taken. The next chapter contains a description of the calibration of time domain reflectometry and neutron probes.

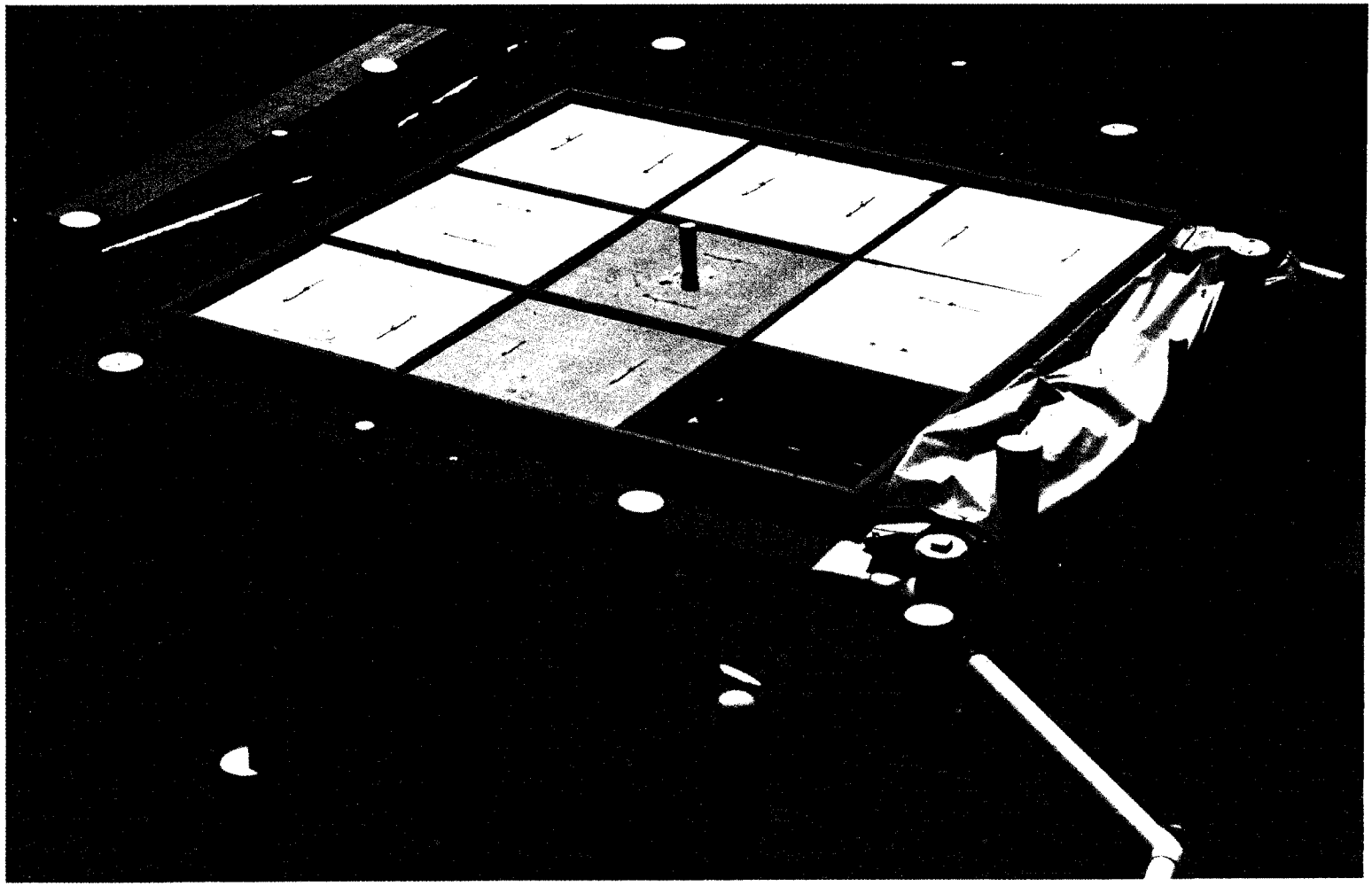

Figure 7. Close-up picture of the infiltrometer. The tarp has been removed to expose the insulation panels just above the nine infiltration arrays. The north insulation panel has been removed to provide a view of infiltration array plumbing. (picture taken by Jim Brainard)

Chapter 3 Time Domain Reflectometry (TDR) and Neutron Probe Calibration Procedures

3.1 TDR Calibration

The time domain reflectometry (TDR) probes were calibrated for two purposes. The first purpose was to obtain a conversion between medium dielectric properties and moisture content. This relationship was used to convert GPR dielectric values to moisture contents. The second purpose was to use the calibrated TDR probes to calibrate the neutron probe.

3.1.1 TDR Calibration Description

Time domain reflectometry is an electromagnetic method of measuring the moisture content of a porous medium. TDR is similar to GPR in that both methods measure travel times, which are then converted to apparent dielectric constant.

Three TDR probes were calibrated using a procedure modified from Young et al. (1997). One important modification was to calibrate the TDR probes for imbibition and draining experiments. Young et al. (1997) used the calibration method for imbibition only (also referred to as upward infiltration in their paper). The TDR calibration procedure is described below.

Sand from the field site within the upper 1.5-m depth range was oven dried for 24 h at 105°C. A 16-cm polycarbonate column was tared on a digital balance and then packed with sand to a bulk density of 1.67 g/cm (Figure 8) The bulk density value was obtained from lab measurements of sand between 0 to 1.5-m depth. The TDR probes were designed and constructed at Sandia National Labs using three parallel 0.8-cm-diameter stainless steel rods, 15.3 cm in length, spaced 2.5 cm apart which were then

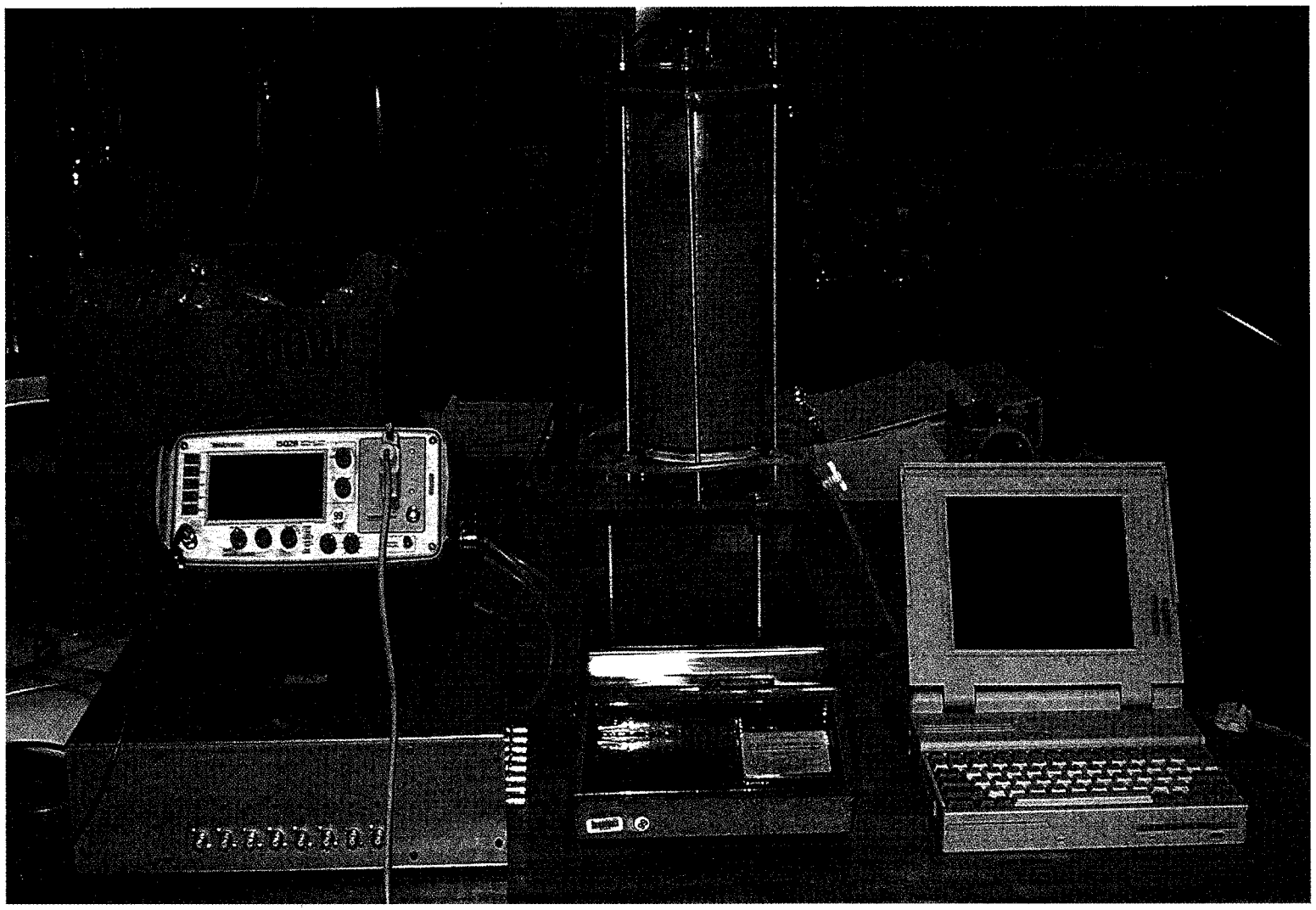

Figure 8. Picture of the TDR calibration set-up. The TDR data acquisition unit is on the left and the digital balance with the sand column are in the center.

connected to a polycarbonate block with dimensions of 7.5 by 5 by 4 cm (Wilson et al., 1995). A series of experiments was performed with each probe to determine the relationship between dielectric constant and moisture content. One probe per experiment was inserted vertically into the sand column, making sure the head of the probe was flush with the sand surface, while the end of the probe reached within 0.7 cm of the bottom of the sand column. A 0.5-in Lexan sheet lid was then fastened onto the top of the column. The TDR coaxial RG59/u cable was connected to a TDR cable tester (Model 1502B, Tektronix Corp., Beaverton, OR) which sent data to a computer via an interface. Since the sand column rested upon a digital balance, periodic weight measurements were recorded on another computer to calculate the moisture content. The two-laptop computers were synchronized in time as data acquisition began and measurements were taken at 1-min intervals. For the imbibition experiment, water was pumped in from the bottom through a porous plate at a constant rate of 6 g/min with a peristaltic pump. The porous plate allowed water to travel upward or downward while containing the sand. The column components were non-metallic in order to avoid shorts in the TDR trace which would occur if the probes came in contact with another metallic object. In addition, for the imbibition experiment, the porous plate aided in the even distribution of water. Saturation was assumed when the horizontal wetting front progressed to the top of the column and water could be seen on the majority of the top surface of the sand.

The imbibition experiment took several hours, while the drainage experiment took approximately 24 hours. For the drainage experiment, the pump was reversed and water was removed from the bottom of the chamber, until air was in contact with the bottom of

the porous plate. Unlike the constant pumping rate for the imbibition experiment, the pumping rate for the drainage experiment decreased with time. The initial pumping rate was approximately 55 g/min with a sampling interval once every five seconds. As the pumping rate decreased the length of the sampling interval was periodically increased. After 12 hours the sampling interval was once every 10 minutes. This procedure relies upon the results of Topp et al. (1982) that the TDR probe measures average moisture content in the presence of steep wetting fronts.

3.1.2 TDR Calibration Data Processing

Time domain reflectometry consists of a transmitted pulse that travels down the center TDR prong and is reflected as the wave reaches the end of the probe. Since the dielectric properties of the porous medium influence the travel time of the propagating wave, the apparent dielectric constant can be calculated. A thorough discussion of TDR theory is beyond the scope of this thesis; the reader is referred to White and Zegelin (1995) for a complete discussion. A TDR data reduction program, similar to Baker and Almarus' (1990) method, was used to convert the TDR trace to apparent dielectric constant.

3.1.3 TDR Calibration Results

The TDR-obtained dielectric values were correlated to the corresponding moisture content values, resulting in a site-specific empirical relationship between apparent dielectric constant and volumetric water content. Several experiments were run for each probe. Four imbibition experiments and one draining experiment were conducted for probe 1. For probes designated 2 and 3, three imbibition experiments and one drainage experiment were conducted for each probe. Figures 9-11 show the imbibition

(wetting curve) and the drainage (drying curve) results for all three probes in which moisture content is plotted versus apparent dielectric constant. A polynomial fit was calculated for the combined wetting curves and a linear fit was calculated for the drying curve. For both the drying and wetting curves the coefficients of determination (R^2) were 0.98 or above, indicating that the appropriate coefficients were chosen. An R^2 of 1.0 indicates a perfect fit. The noticeable difference between the wetting and drying curves is due to hysteresis. The linear fit for the drainage experiment was chosen for the empirical relationship between moisture content and apparent dielectric constant. In figure 12, all three drying curve data sets were combined to obtain an average empirical relationship. The drying curve data was chosen for the empirical relationship because it showed less variability between several experiments than the wetting curve data. The resulting relationship is:

$$\theta = 0.0136 * K - 0.033 \quad (7)$$

3.1.4 Evaluation of Topp's Equation

The accuracy of Topp's equation (Topp et al., 1980) was evaluated by comparing the moisture content calculated via this equation (Eq. 6) to the measured moisture content (Figures 13-15). For each TDR probe, the measured dielectric constant was plotted versus the moisture content. For direct comparison, both the measured moisture content and the moisture content calculated via Topp's equation were plotted on the same figure. Topp's equation overestimated the moisture content in all three cases.

The overestimation of moisture content is likely due to the assumption that no magnetic minerals are present in the porous medium, an assumption inherent to the equation relating velocity to apparent dielectric constant (see Eq. 4+5). Electromagnetic

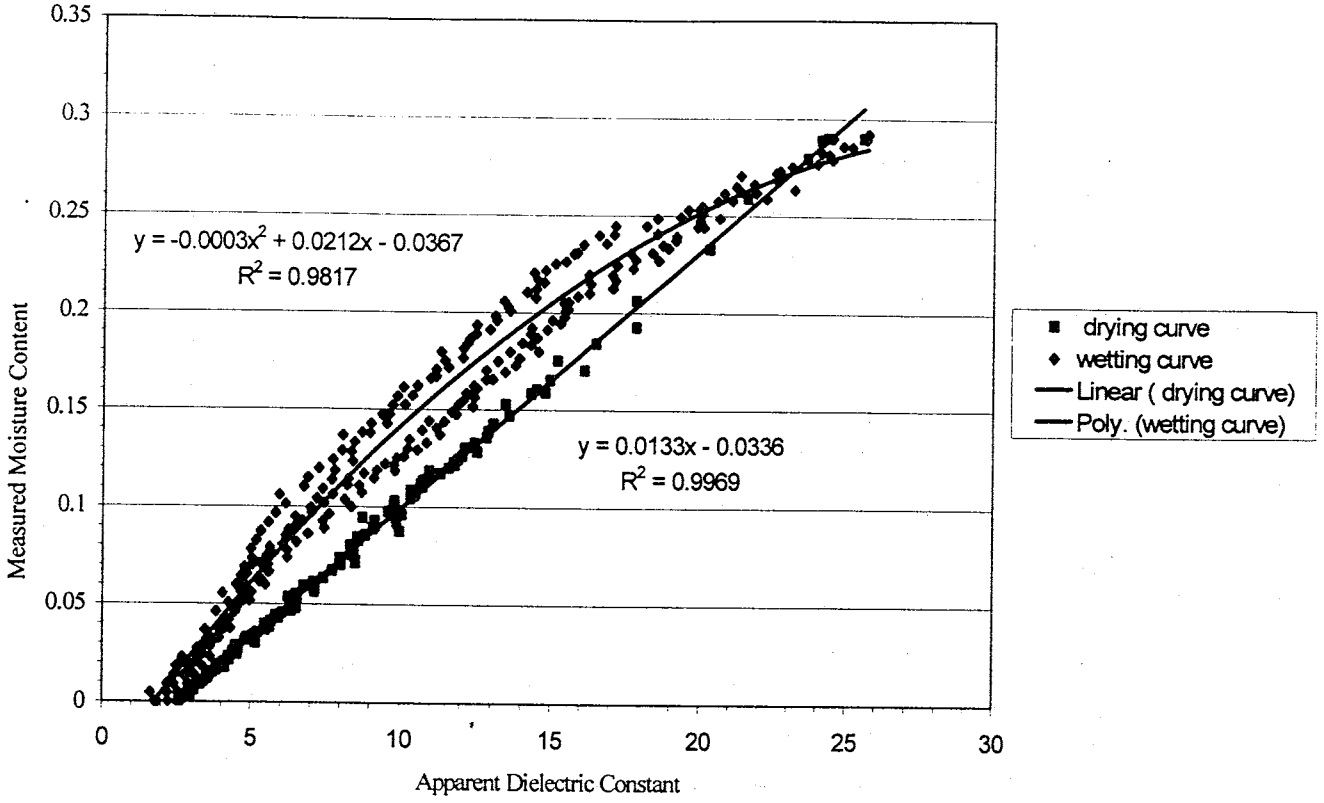

Figure 9. Apparent dielectric constant versus moisture content for four wetting experiments and one drainage experiment for TDR probe 1.

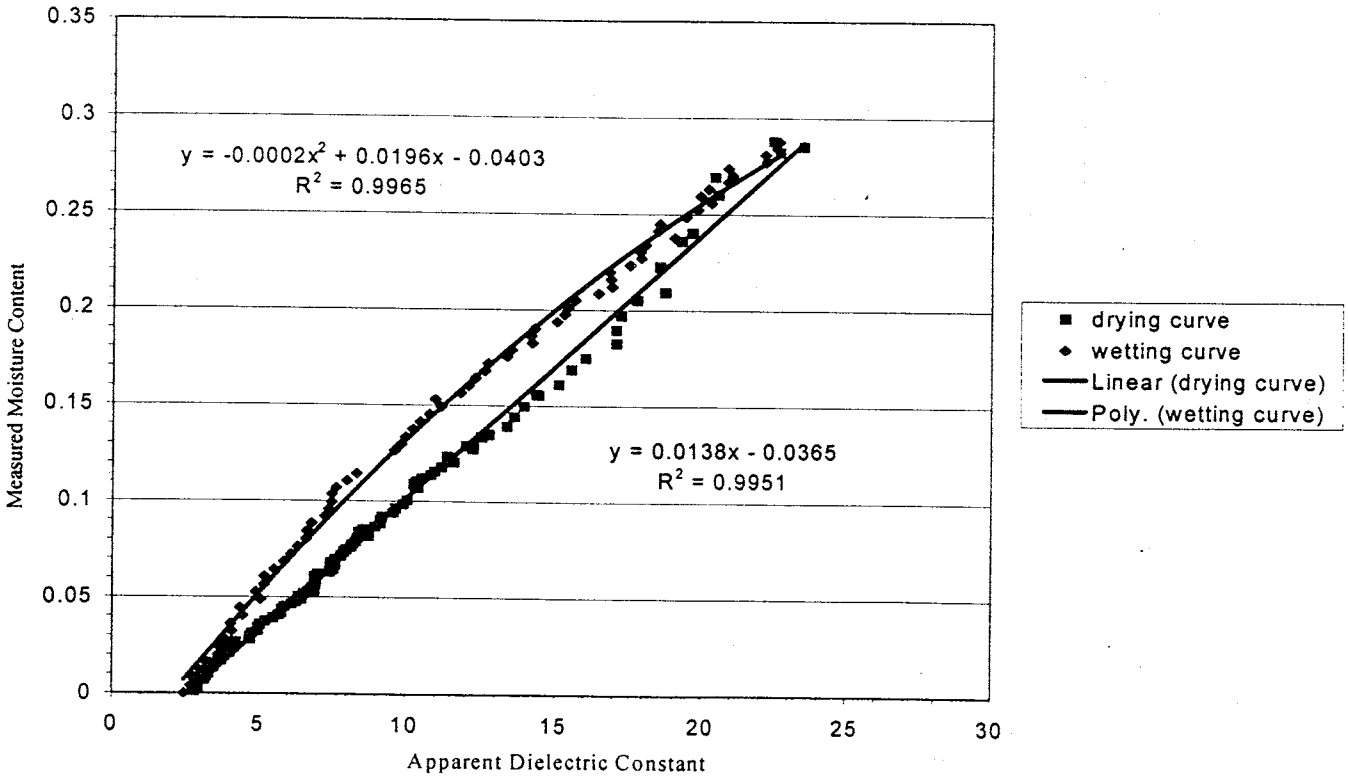

Figure 10. Apparent dielectric constant versus moisture content for three wetting experiments and one drainage experiment for probe 2.

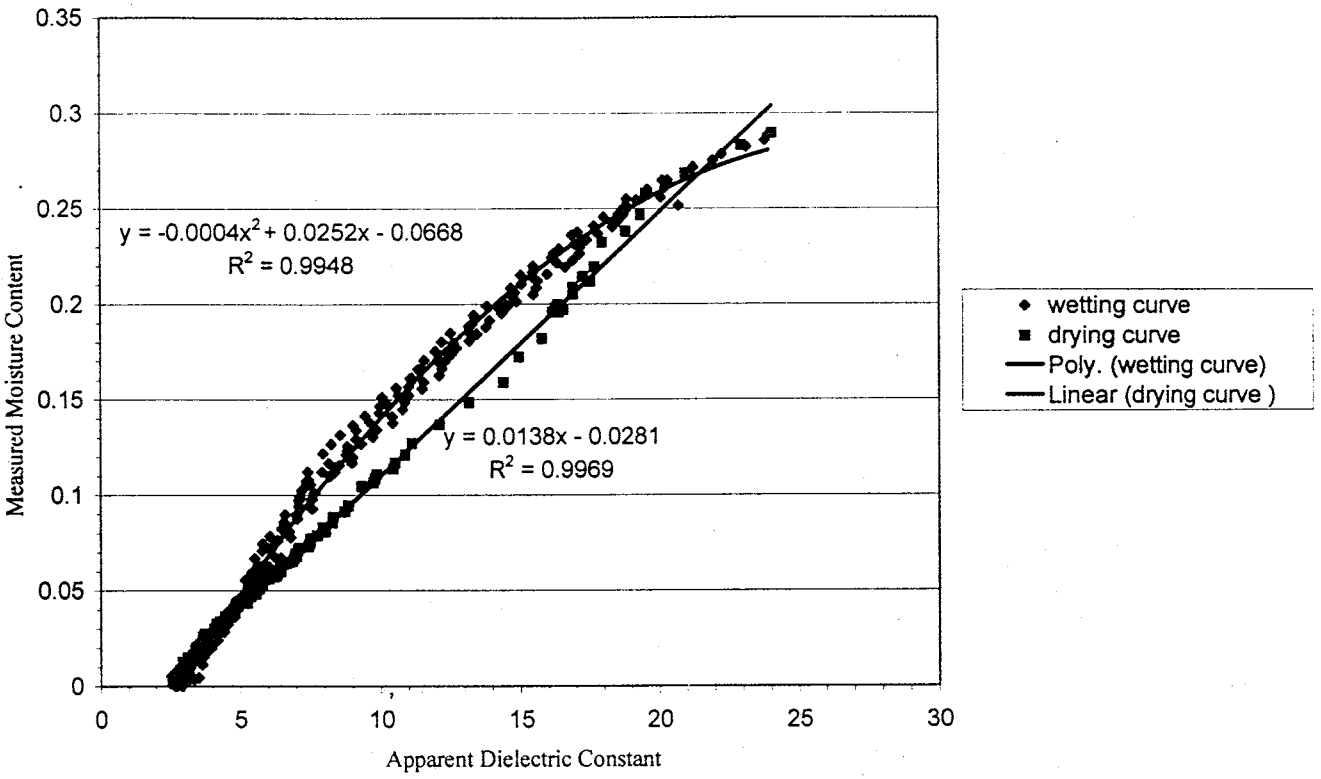

Figure 11. Apparent dielectric constant versus moisture content for three wetting experiments and one drainage experiment for probe 3.

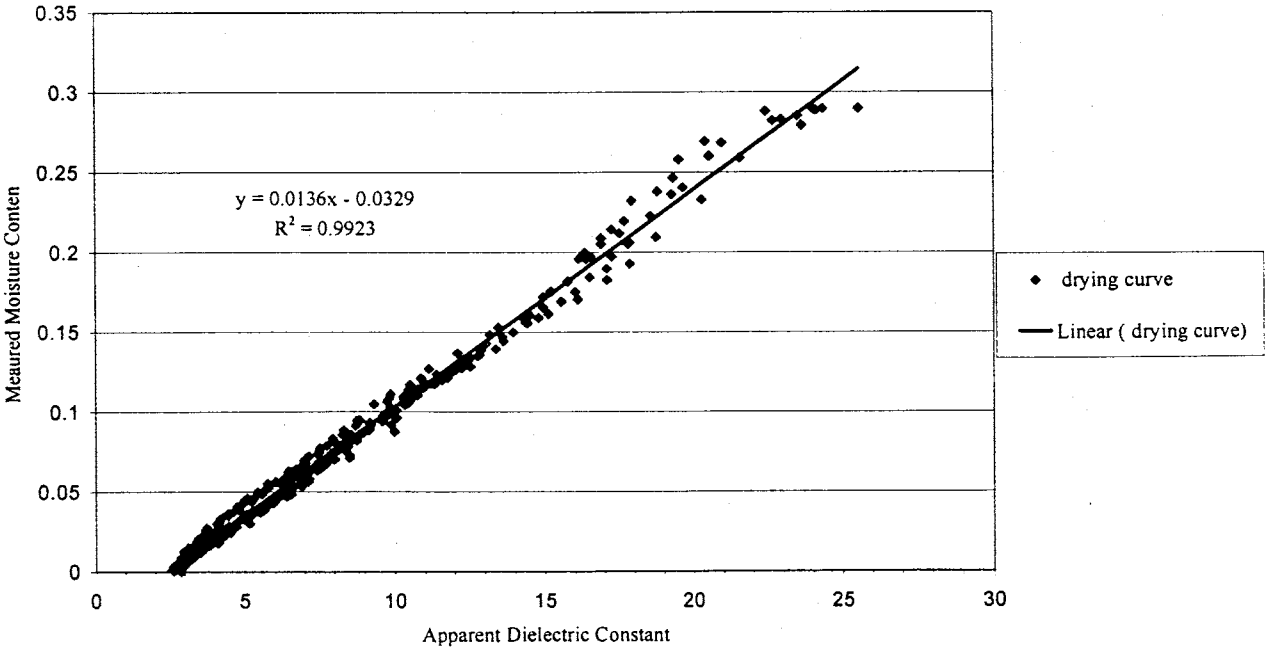

Figure 12. Apparent dielectric constant versus moisture content for all three drainage experiments.

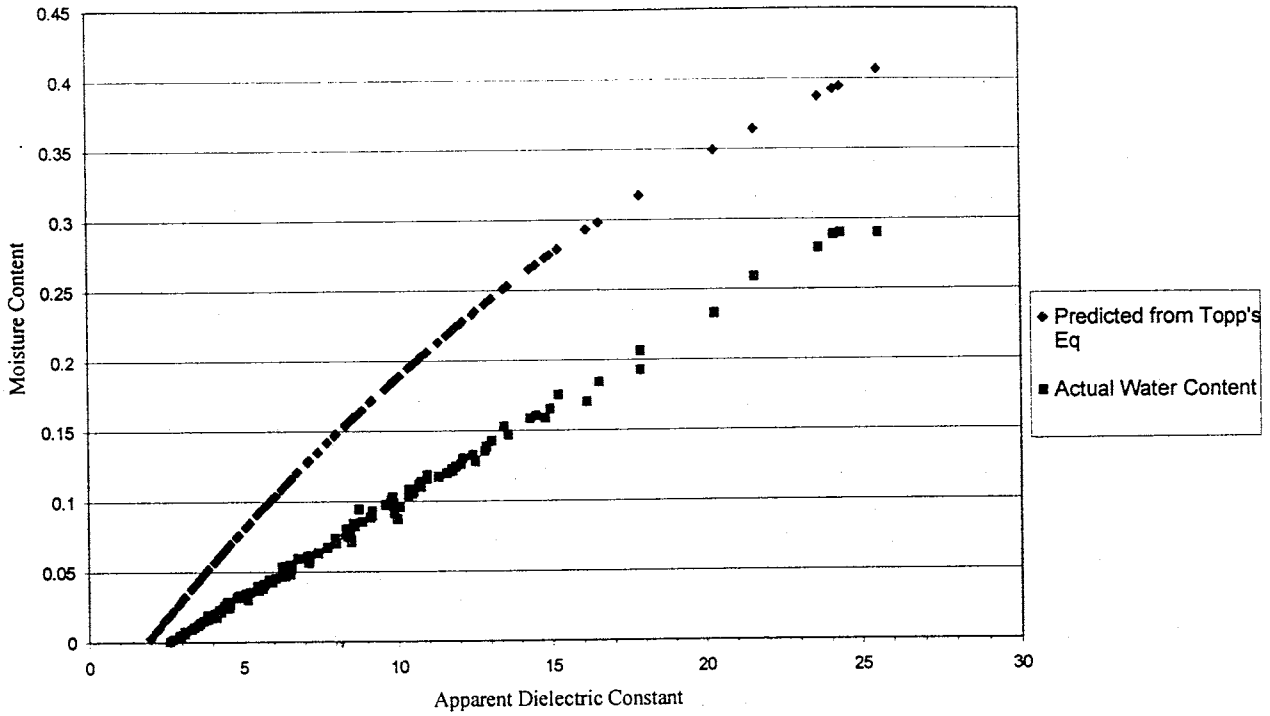

Figure 13. Graphical comparison of measured moisture content versus dielectric constant and that predicted by Topp's equation for TDR probe 1.

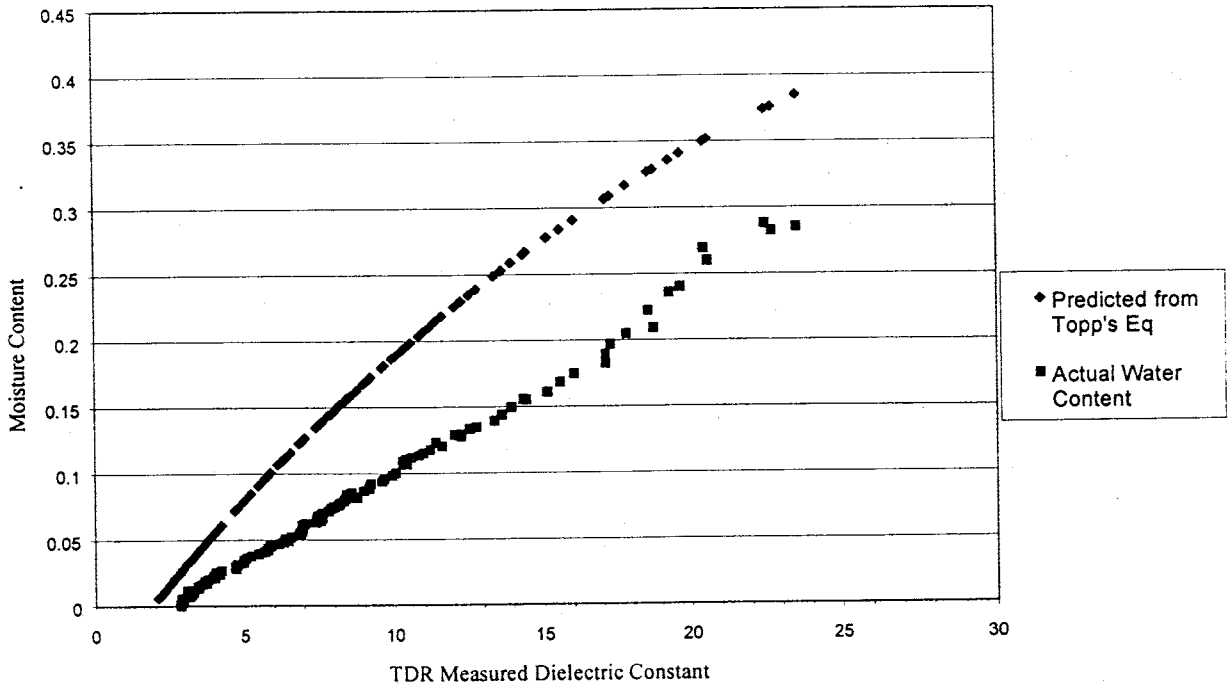

Figure 14. Graphical comparison of measured moisture content versus dielectric constant and that predicted by Topp's equation for TDR probe 2.

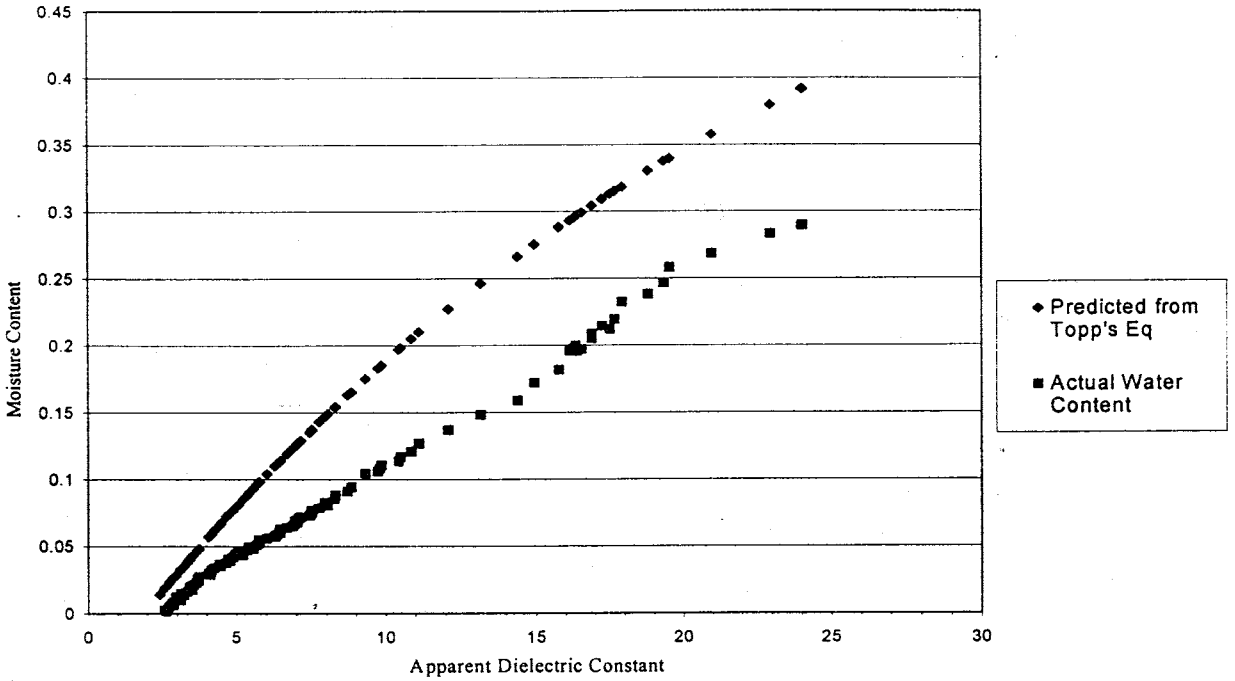

Figure 15. Graphical comparison of measured moisture content versus dielectric constant and that predicted by Topp's equation for TDR probe 3.

wave velocity is inversely affected by magnetic permeability according to the following equation (Annan, 1999):

$$v=1/(\mu * \varepsilon)^{0.5} \quad (8)$$

where μ is the magnetic permeability (H/m). In the absence of magnetic minerals the magnetic permeability is constant and equal to that of air (1e-6 H/m). However, if magnetic minerals are present, the magnetic permeability will increase and no longer be constant, thus causing a decrease in the EM velocity.

At the field site, the upper meter contains approximately 9% magnetic minerals by weight. The percentage of magnetic minerals was determined by spreading a sample of sand on a piece of paper and passing a magnet over the sample numerous times to collect any magnetic minerals present, which were then weighed. Since the dielectric constant is calculated based on the inverse of the velocity, the apparent dielectric constant value will be overestimated. In turn, moisture content will be overestimated when using Topp's equation due to the direct relationship between moisture content and apparent dielectric constant. Therefore, the TDR calibration equation (Eq. 7) was used in place of Topp's equation to convert GPR dielectric constant measurements to moisture content.

3.2 Neutron Probe Calibration Procedure and Results

3.2.1 Neutron Probe Calibration

A model 503 CPN Hydroprobe (Martinez, CA) was used in this study. A neutron probe has a radioactive source of 50mCi Americium-241/Be that emits high-energy neutrons. The neutrons are preferentially thermalized or slowed down by hydrogen atoms. A thermalized neutron detector on the neutron probe records the number of thermalized neutrons present as counts. Therefore, the higher the number of counts, the

more hydrogen (mostly in the form of water) contained in the porous medium. The neutron probe was calibrated at the field site to obtain absolute moisture content measurements.

Traditional calibration methods involve taking undisturbed porous medium samples in conjunction with neutron measurements. However, due to both the unconsolidated nature of the sediment at the site and past difficulties collecting undisturbed samples, TDR probes were suggested as an alternative way to calibrate the neutron probe. An advantage of TDR is that it allows for continuous non-destructive measurements in time.

Before neutron data was collected, a standard count was performed. A standard count is the mean of 32 measurements 8 seconds each, taken when the probe is inserted in a 30-gallon water-filled plastic barrel that represents an infinite source of hydrogen.

3.2.2 Neutron Calibration Location, Instrument Set-up, and Procedure

The neutron probe was calibrated in sand, 11.5 m southwest of the center of the test site (Figure 7). A 2-in diameter PVC access tube was installed to a depth of 0.75 m for neutron data acquisition. The three calibrated TDR probes were emplaced vertically 0.35 m from the neutron access tube at a depth of 0.75 m and buried (Figure 16).

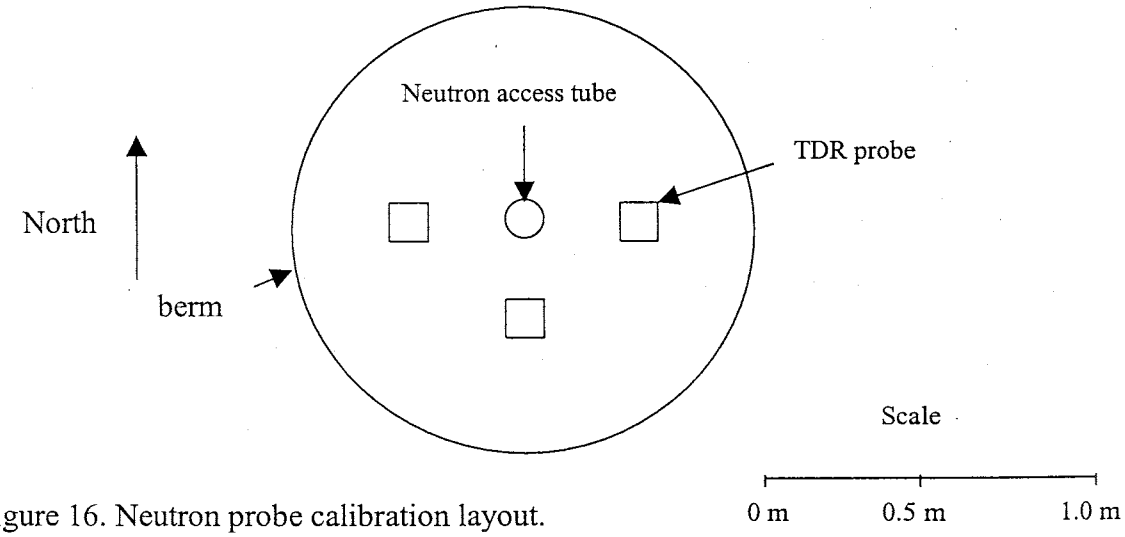

Figure 16. Neutron probe calibration layout.

The TDR probes were connected to a multiplexer, which allowed for simultaneous measurements to be taken. A berm was constructed around the instruments to contain water for infiltration.

Water was applied to the calibration site with both a standard hose and a permeable hose. The permeable hose was concentrically laid out around the area and left on for several hours to provide a slow rate of water application. The standard hose was only used for approximately 10 minutes, due to the high flow rate. The area was covered with a tarp when measurements were not being taken to prevent evaporation. After the area appeared saturated, the permeable hose was turned off and water at the surface was allowed to drain for a short time before measurements were taken. Measurements were taken frequently at early times as the area drained quickly and less frequently as the rate of change decreased. For each sampling period, three consecutive measurements were taken on the TDR and neutron probes. Each sampling period lasted for approximately 1 minute. The experiment was repeated several times in order to obtain more data points in the high moisture content range.

3.2.3 Neutron Probe Calibration Results

In Figure 17 the neutron probe results are plotted verses moisture content. The moisture content was obtained from the TDR measurements using Eq. 7 to convert apparent dielectric constant to moisture content. The average of the nine TDR measurements (3 from each probe) are plotted against the average of the 3 neutron values. The neutron count measurements are expressed as a count ratio or raw counts divided by the standard count. A linear calibration equation was obtained for the 22 data

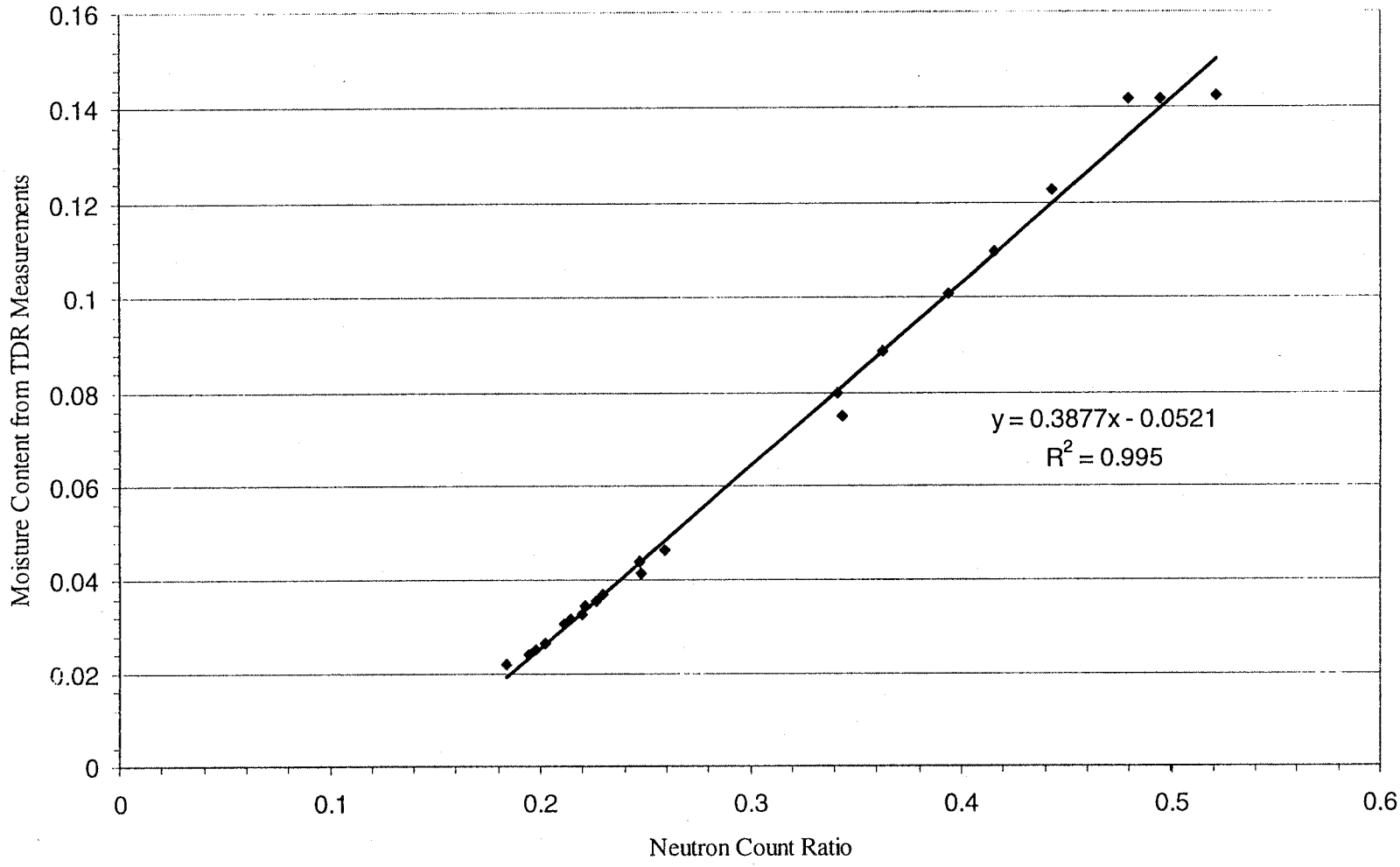

Figure 17. Neutron calibration equation: moisture content versus neutron count ratio.

points, which is expressed below:

$$\theta = 0.3877 * (\text{count ratio}) - 0.0521 \quad (9)$$

3.3 TDR and Neutron Probe Error Analysis

Every measurement has error associated with it, which should be quantified to properly evaluate the measurements. Error bars were calculated for neutron moisture content values by quantifying the error for both the TDR and neutron probe measurements since both were used to obtain neutron moisture content measurements. The method of obtaining error bars for neutron moisture content values is briefly described below, with a derivation and actual calculations contained within Appendix 2. Error bars were calculated from a regression analysis in conjunction with neutron measurement variance. Since three neutron values were recorded for every reported data point, the variance of the neutron values can be evaluated. In Figure 18, a regression was calculated by plotting the moisture content calculated from the nine individual TDR measurements (3 from each probe) versus the average neutron count ratio. The neutron values were averaged since a specific neutron value did not correspond to a specific TDR measurement. Each of the nine TDR measurements was plotted to portray the variability of the associated moisture content values. The statistical results from the regression analysis are in Appendix 2. Figure 18 illustrates a wide spread among the TDR measurements at higher moisture contents. This variability is probably due to the non-uniform movement of water through the upper meter.

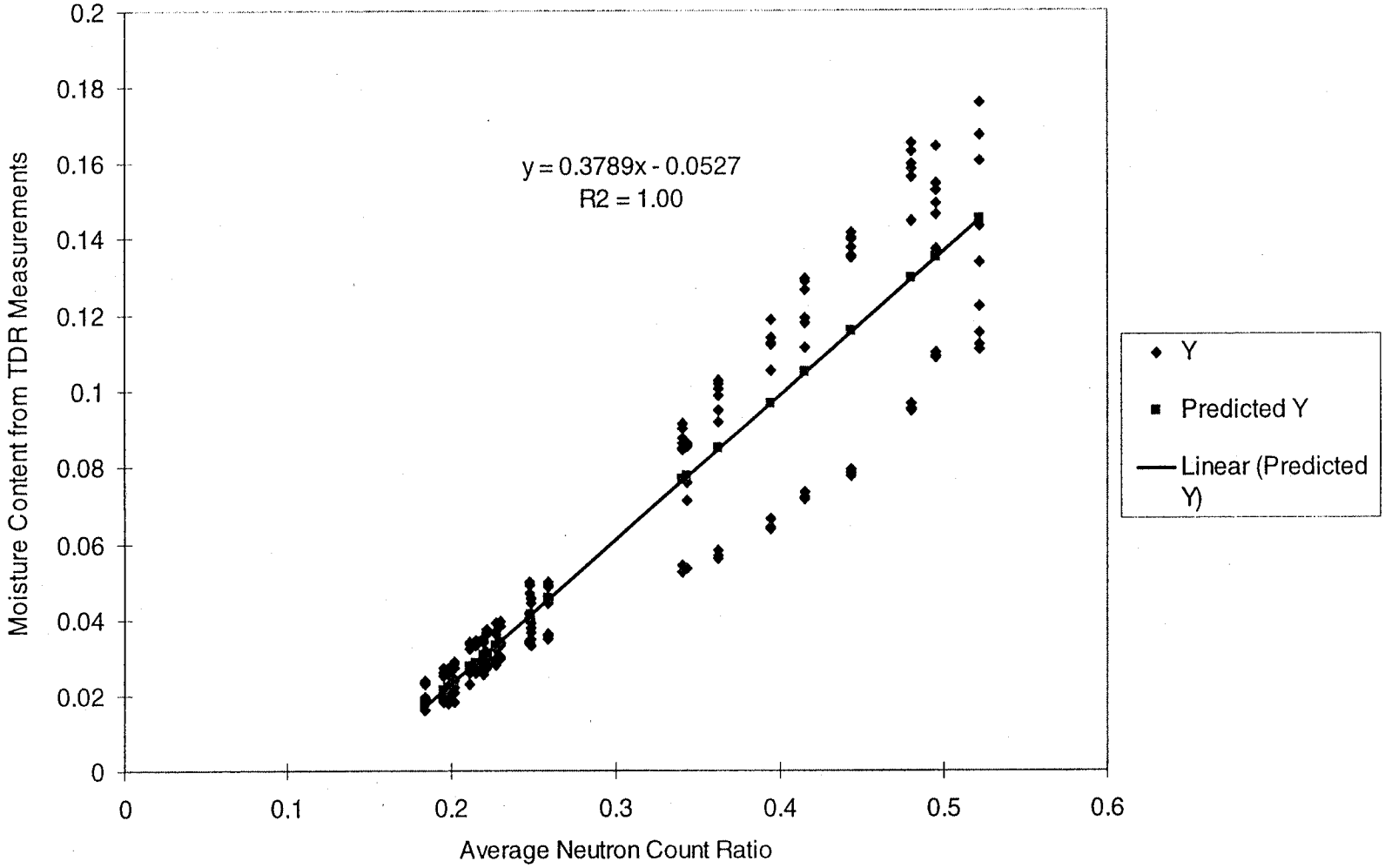

Figure 18. Regression error analysis.

The moisture content (Y) was calculated by:

$$Y = \Upsilon + b\,(x-\chi) + \varepsilon \qquad (10)$$

where Υ is the mean moisture content, b is the slope of the regression line, χ is the mean average neutron count ratio, x is specific neutron count ratio value, and ε is the measurement error. This relationship was used to obtain the variance of Y as a function of the neutron counts. Several approximations were made and the resulting equation for variance is:

$$\text{var}\,(Y) = s^2/n + s^2 + s^2(x-\chi)^2/9\Sigma(x_I-\chi)^2 + b^2(\text{var}(x) + \text{var}\,(x)/m) \qquad (11)$$

where n is the number of TDR measurements, m is the number of average neutron measurements, s^2 is the variance of the error, and var (x) is the variance of the neutron measurements. The two latter terms are quantifying the variance estimate of the slope of b. The variance of Y was solved for high moisture contents to calculate a worst case scenario. A description of the approximations made to solve for the variance are in Appendix 1.

The variance of Y for a neutron count ratio of 0.5215 was 2.32×10^{-4}. The resulting standard deviation was 0.0152 and the two standard deviations result was 0.03. Error bars were assigned based upon two standard deviations in order to represent a 95% error bar. Therefore, $\pm$ 0.03 or $\pm$ 3% is the associated error bar for neutron moisture content measurements. The neutron moisture content was initially expressed as a decimal where 1 represents 100% water by volume. Since GPR moisture content values were calculated as percent moisture content, the neutron values and the error bars have been converted to percent as well.

4.0 NEUTRON PROBE AND GPR DATA ACQUISITION AND PROCESSING METHODS

4.1 Neutron Probe Data Acquisition and Processing Methods

4.1.1 Neutron Probe Data Acquisition Procedure

Neutron probe measurements were taken in 13 PVC access tubes. Data collection parameters included a 0.25-m sampling interval with measurements starting at 0.5-m depth. The neutron data presented in this thesis were collected as follows: first, a standard count was performed before taking a data set and then a chi-squared ratio was displayed, which is a statistical means of indicating if the probe is functioning properly (CPN, 1984). A chi-squared test is the ratio of the standard deviation of the measurements just taken, divided by the ideal standard deviation. Theoretically, the ratio should be equal to one. However, for a 95% confidence interval the acceptable range of ratio values is.75 to 1.25 (CPN, 1984). If the chi-squared value fell outside of the range then the standard count was repeated. The reader is referred to the CPN neutron probe manual (CPN, 1984) for a more in-depth discussion of the standard count and relative statistics.

Next, count measurements were taken within the access tubes. Each measurement was taken over a 32-second time interval. ID numbers were assigned to each of the 13 access tubes to facilitate downloading of the data. For a complete step by step procedure of neutron data acquisition, refer to the neutron probe operating procedure in Appendix 3.

4.1.2 Neutron Probe Data Processing Methods

Data from all 13 access tubes were stored in the neutron probe memory and then downloaded onto a computer in the data acquisition building on site. Conversion

programs used the standard count along with the neutron calibration equation (Eq. 9) to convert the raw data to moisture content.

4.1.3 Neutron Acquisition Schedule

Neutron measurements were taken daily when infiltration first began, then weekly and biweekly as the wetting front progress continued to slow down. In addition, only the 5 access tubes closest to the infiltrometer were sampled when infiltration began. As infiltration continued, all 13 access tubes were sampled weekly and then biweekly.

4.2 GPR Data Acquisition and Processing Methods

4.2.1 GPR Data Acquisition Procedure

For this study a Sensors and Software Pulse Ekko 100 GPR system (Mississauga, ON) was used. The GPR data collection parameters included using a center frequency of 100 MHz and a 0.25-m spatial sampling interval for both the transmitter and the receiver. (The pulse that is transmitted is actually a range of frequencies which centers around 100 MHz, and thus just the center frequency is reported.) The 100 MHz antennas are 1 m in length with the 0-m depth, 0.5 m from the bottom of the antenna. GPR measurements began at a depth of 0.25 m. The transmitter and receiver were always in adjacent boreholes for data collection of the 4 well pairs, ie AB, BC, CD, and DE. Larger antenna separation could not be used because of attenuation of the GPR signal. The transmitter and receiver were always employed in the same locations for each well pair.

Ground penetrating radar measurements are sensitive to subsurface cables. Since hydrological cables were to be permanently installed at the field site, experiments were conducted before the cables were installed to determine the exact influence of cables on the GPR data. The experiments consisted of measurements taken between two access

tubes first without any cables present. Then, measurements were repeated with cables emplaced vertically in nearby access tubes where these cables would eventually be installed. The first arrival times were altered by the presence of the cables only when the transmitter and receiver positions made an angle greater than 45° from the horizontal. A 45°-acquisition angle occurs when the vertical distance between the transmitter and receiver is the same as the borehole separation distance. For example, if the borehole separation distance is 2.25 m, and the transmitter is at a depth of 5 m, then the receiver positions range between depths of 2.25 m and 7.25 m (Figure 19). To avoid cable influences, a 45°-acquisition angle between the transmitter and receiver was established and employed for every transmitter position ranging from 0.25 m to the bottom of the access tube. In addition, GPR measurements were only collected along the southwest-northeast diagonal, and surface cables from the hydrologic probes were routed away from the diagonal in order to avoid fast travel time paths along the cables that could bias the GPR measurements.

Before accurate data could be obtained, a series of five calibration measurements were taken. Due to "trigger delay" and instrument drift the measured travel time is greater than the true travel time. A "trigger delay" occurs because a short time interval exists between the time a signal is sent to the transmitter, and the time the transmitter actually sends out a pulse. In addition, the transmitter, receiver, and console electronics experience electronic drift which adds an additional time delay. Calibration measurements enable the instrument bias due to the "trigger delay" and the instrument drift to be subtracted from the travel time measurement in order to obtain the true travel time between the transmitter and receiver.

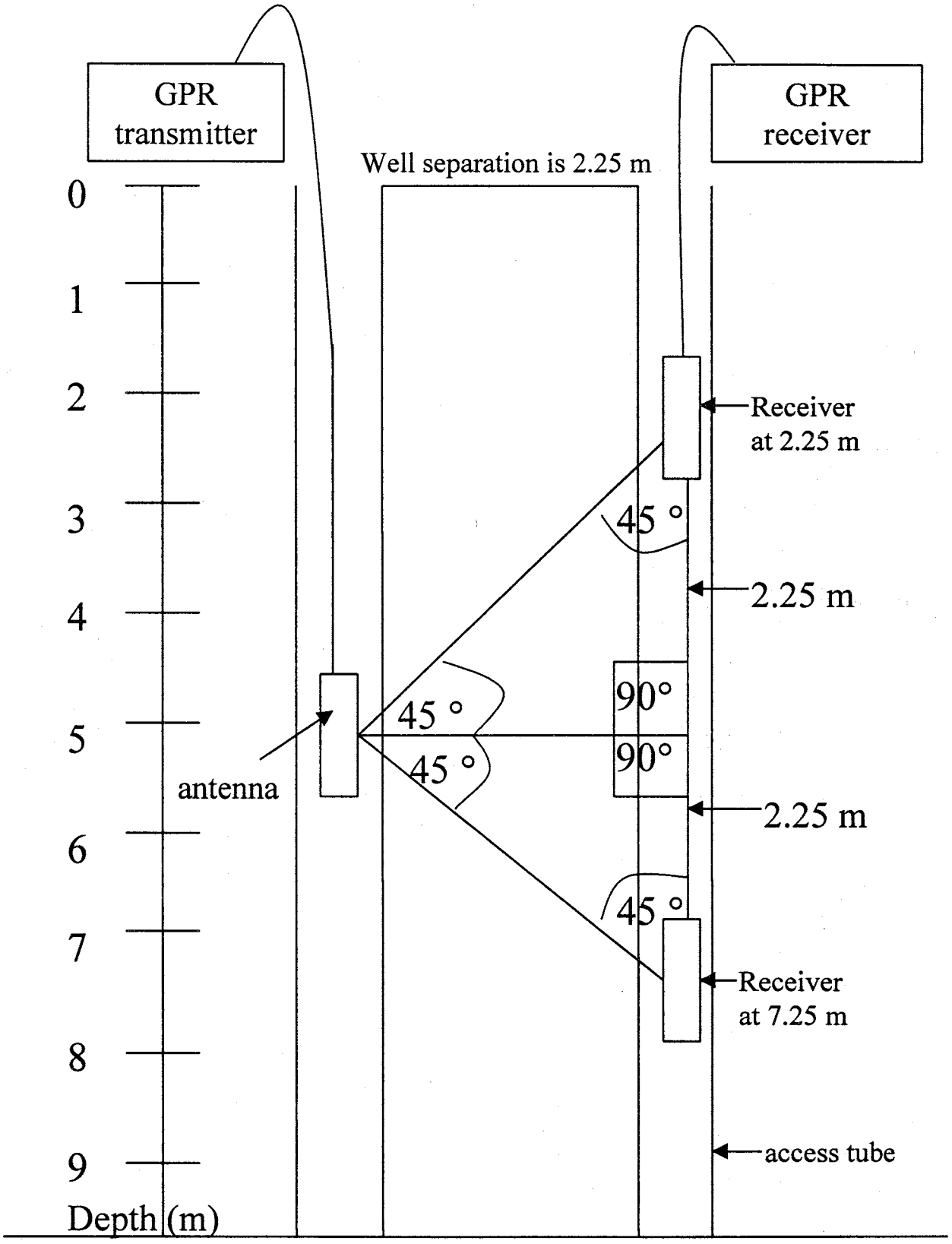

Figure 19. Schematic of 45-degree GPR acquisition angle.

To perform a calibration, the transmitter and receiver were placed at a known distance from one another and suspended vertically in air with their 0-m depth mark set 1-m above the ground surface. From the measured first arrival times, the EM velocity in air (0.33m/ns), and the separation distance, the instrument bias can be calculated and then applied to the data.

With time, temperature and other factors caused changes in the instrument bias. In order to correct for these temporal changes in the instrument bias, the instrument was recalibrated after every 10th repositioning of the transmitter. The new calibration file was applied to the ten transmitter position files taken following the calibration.

An additional check was performed in the porous medium outside of the infiltration zone of influence. Travel time measurements were taken during pre-infiltration and infiltration conditions with both the transmitter and receiver at 11.5-m depth. The travel times increased with time by about 1-3ns. Since these measurements were taken outside of the zone of influence an appropriate time shift was applied to the infiltration data to correct for the observed shift. From the five pre-infiltration data sets, an average travel time (with the instrument bias corrected for) was calculated for each well pair. During infiltration, the measured bottom travel times were compared to the average bottom pre-infiltration travel times. The time bias was then subtracted from the measured infiltration travel times as a time shift throughout the depth profile for each individual well pair to give a more accurate estimate of the true travel time.

4.2.2 GPR Data Processing Methods

After the calibration was applied to the data, the first arrivals of the direct waves, or EM wave travel times were 'picked' using Sensors and Software's Ekko42 data

processing package. Then, the travel time data were inverted using the tomography code of Aldridge and Oldenburg (1993) to produce a 2-D image of EM wave velocity. This scheme imposes constraints on the inversion in the form of horizontal and vertical first-difference regularization to produce an estimate of the velocity that varies smoothly from one point to another within the image domain (Aldridge and Oldenburg, 1993). In addition, the tomography code uses a finite-difference travel time computation of Vidale (1988), rather than a ray tracing scheme to compute travel times between the source and receiver.

Once the velocity image was obtained it was converted to an image of apparent dielectric constant via equation 5 in section 1.2.1. The apparent dielectric constant image was then converted to moisture content via equation 7 from section 3.1.3. For processing, all four well pair data sets were combined and analyzed as one complete data set.

Difficulties drilling through gravels at 1.5-m depth caused deviations from the vertical in the southwest access tubes. These deviations resulted in image artifacts at depths of greater than 7 m that were determined by plotting the residual error. Below 7 m the residual error was no longer random. Therefore the moisture content was only imaged to 7 m. The deviations are a source of error because the exact distance between the two well pairs is no longer known. However, by only imaging to 7 m the error was minimized.

Infiltration GPR images were processed with the bottom time shift explained in the previous section. In addition to the moisture content results, the ray density as a function of position was examined. A 2-D image of the GPR ray density provides an

indication of which areas are well resolved, and which are poorly resolved. Areas with a high ray density are well resolved.

4.2.3 GPR Data Acquisition Schedule

Five complete pre-infiltration data sets were taken over a course of 4 months. Once infiltration began, GPR measurements were taken approximately weekly; resulting in 7 images taken 7, 14, 21, 28, 35, 42, and 119 days after infiltration began. After 42 days of infiltration, the GPR system was malfunctioning and was sent back to the manufacturer for repairs. Upon its return another data set was collected 119 days after infiltration began.

4.2.4 GPR Instrument Problems

During the course of data acquisition several instrument problems commonly occurred. The problems were mainly with the connections, either with the fiber optic cables, antennas, or antenna cables. The fiber optic cables are the weakest link in the GPR system. The cables will not work if they become bent. However during necessary movement within the field, these cables occasionally became bent due to their fragile nature. Once bent, new cables had to be purchased before the system would work again. In addition, during normal use the fiber optic cables wear down and are no longer able to transmit and receive signals. Frequently the cables had to be recut and refitted.

An intermittent poor connection between the transmitter cable and antenna resulted in bad data. This intermittent problem was noticed 42 days after infiltration began. As mentioned earlier, the system was sent back for repairs, at which time the cables were cut back and reconnected. However, the manufacturer could never duplicate the connection problem. General connection problems occurred during data acquisition

and the system would have to be shut down and parts reconnected before it would function again.

The pre-infiltration results for both GPR and neutron measurements are discussed in the following chapter.

5.0 PRE-INFILTRATION RESULTS AND DISCUSSION

5.1 GPR Raw Image Results and Discussion

5.1.1 GPR Raw Image Results

Pre-infiltration GPR measurements were taken in order to: 1) test the feasibility of GPR both to image the spatial distribution of the in-situ moisture content and to accurately determine moisture content values; 2) determine a baseline moisture content image before infiltration began; and 3) quantify GPR measurement error.

Five two-dimensional GPR moisture content images, along with a mean image of all five data sets, are presented in Figures 20 a-f. Depth is represented by the y-axis, and the southwest to northeast GPR data acquisition line corresponds to the x-axis. Along the x-axis, 0 m corresponds to the center access tube, with the other access tubes located at -5.6 m, -2.4 m, 2.25 m, and 5.5 m. A color scale represents the percent volumetric moisture content ranging from 0 to 15%. All five images show very similar moisture content distributions; however, slight differences are present. For example, Figure 20a shows a slightly higher moisture content zone between 2 to 3 m than do any of the other images.

Within the GPR images, six moisture content zones are distinguishable and are indicated on the mean pre-infiltration image (Figure 20f). From the surface to 2-m depth, a low moisture content layer (0 to 4%) is visible. A second slightly higher moisture content zone (4 to 9%) occurs from 2-to 3.5-m depth. Two high moisture content layers (6 to 11%) are located at 4-, and 5-to 6-m depths. A discontinuous thin layer of low moisture content occurs at 4.5-to 5-m depth. Finally, a low moisture content layer occurs

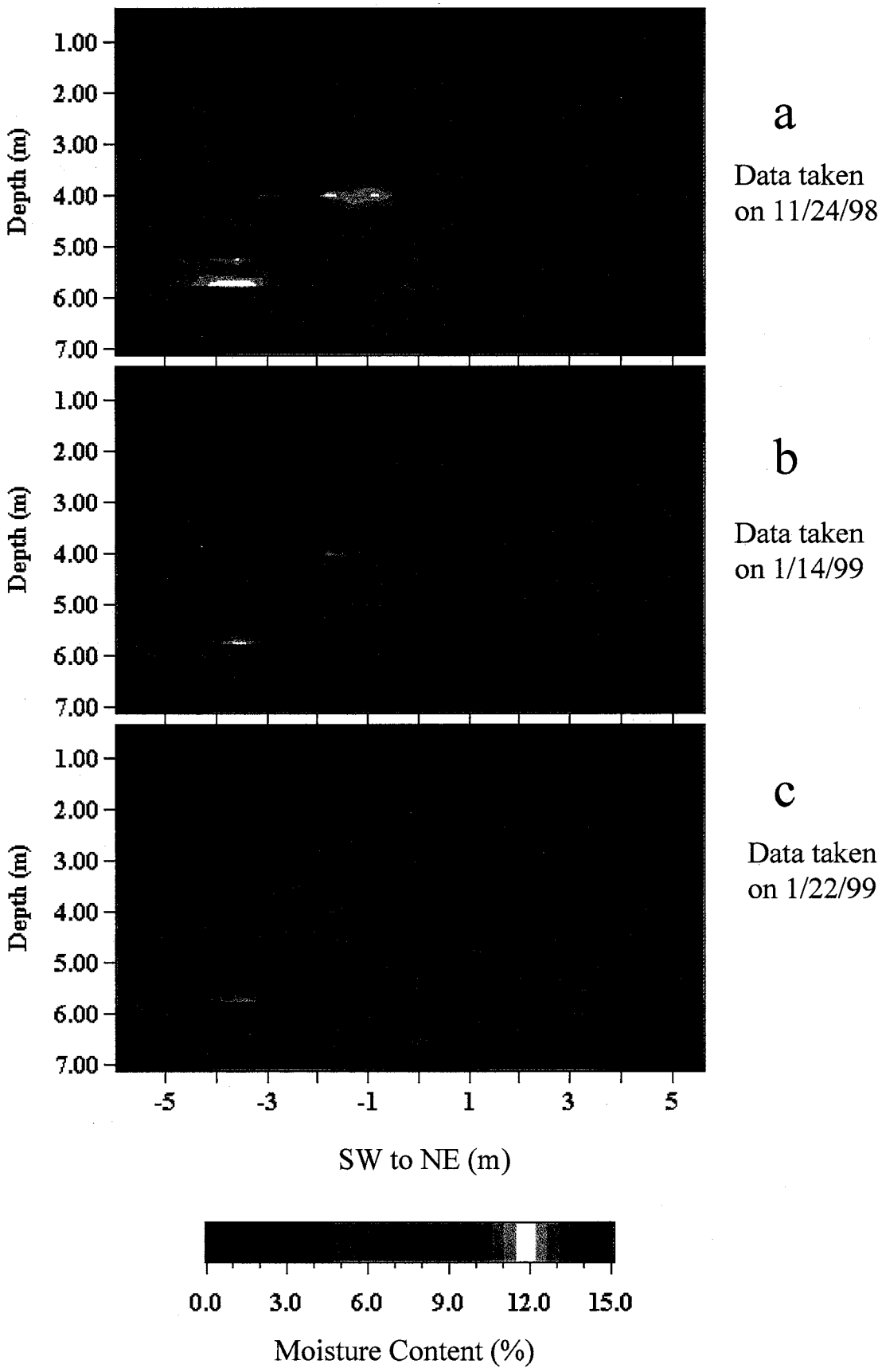

Figure 20 a-c. GPR pre-infiltration moisture content images.

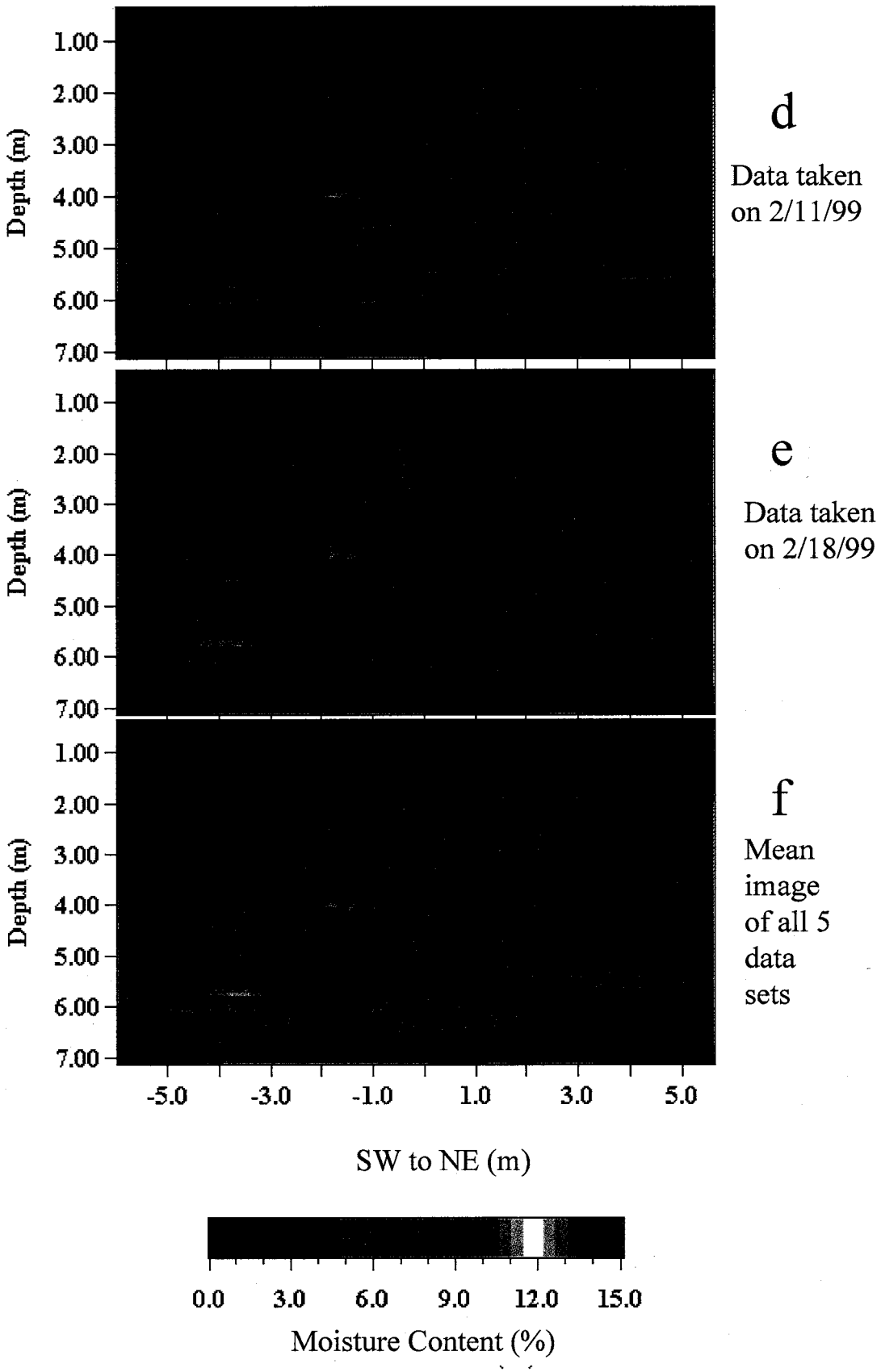

Figure 20 d-f. GPR pre-infiltration moisture content images and mean image.

at 6-to 7-m depth with the exception of a high moisture content area 2.5 to 3.5 m southwest of the plot center.

5.1.2 GPR Discussion

In unsaturated porous media, under unit gradient conditions, clay and silt tend to exhibit higher moisture retention than gravel or sand, due to higher capillary pressures associated with finer grain size. Therefore, under these conditions, low moisture content layers correlate to sand and gravel layers, while higher moisture content layers correlate to clay and silt layers. Based on this information plus the SW and NE stratigraphic columns (Figure 4), geological facies can be assigned to the moisture content layers in the mean GPR moisture content image (Figure 20f) and reproduced as Figure 21. The layer boundaries on the GPR image were drawn based on differences in moisture content and the general location of geologic units according to the SW and NE stratigraphic column.

The two stratigraphic columns provide a limited test on GPR's ability to image the spatial distribution of the in-situ moisture content. In general, the six geologic units correlate well with the six moisture content layers from the GPR image. Both the stratigraphic columns and the GPR images indicate that units 1 to 3 become thicker towards the northeast, unit 4 exists at a lower depth towards the northeast, and unit 5 pinches out in the northeast region. However, slight discrepancies between the GPR image and the stratigraphic column do exist, probably as a result of the distance between the access tubes and the core sample locations.

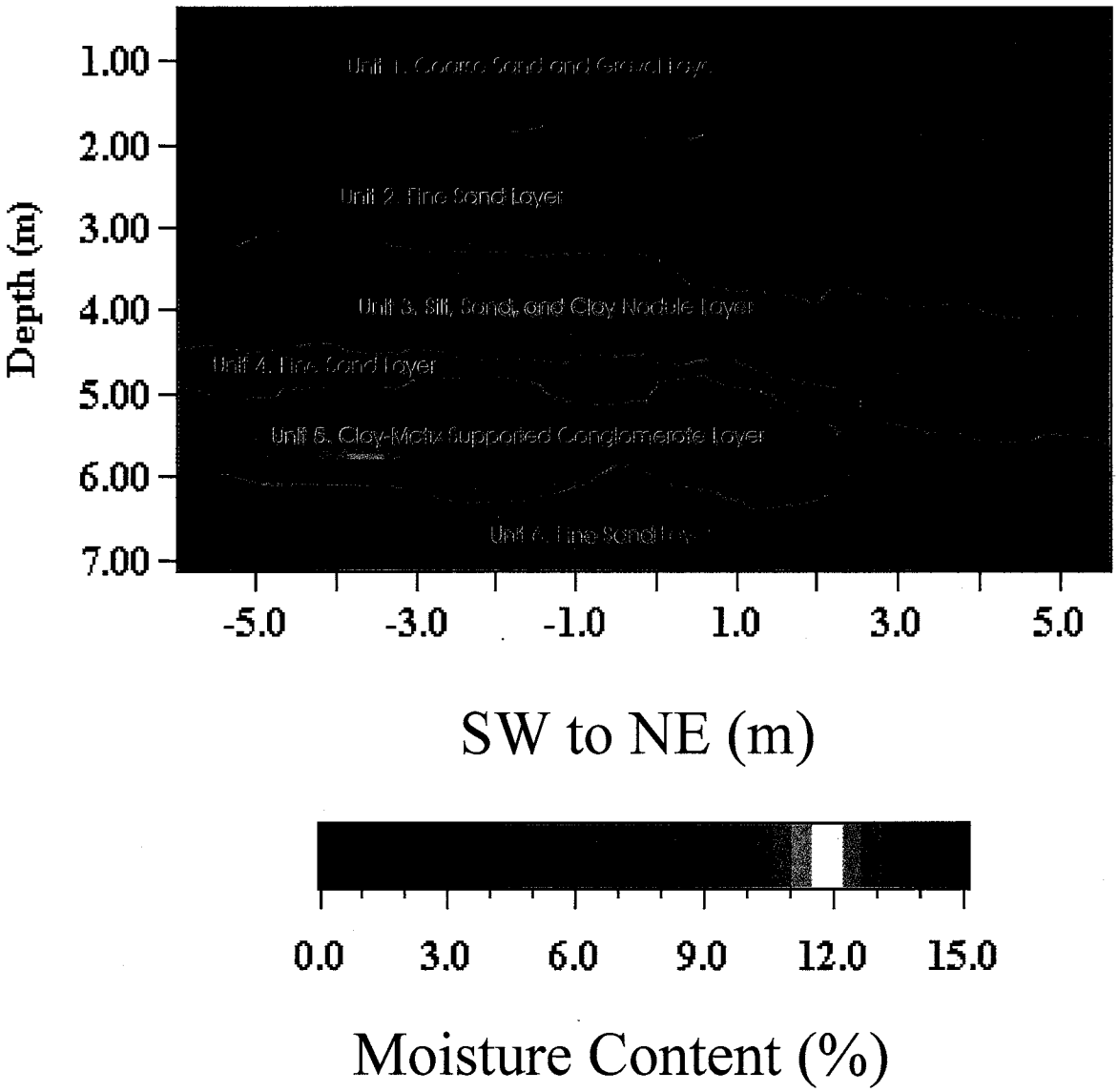

Figure 21. GPR mean pre-infiltration image with geologic interpretation based upon stratigraphic column data.

5.2 Comparison of Neutron and GPR Moisture Content Results and Discussion

Comparisons between the mean GPR image and five neutron moisture content logs provide a more rigorous test of GPR's capability to image the moisture content spatial distribution (Figure 22). Overall, the GPR and neutron measurements are very consistent. For example, both instruments measure areas of high moisture content at 4-, and 5-to 6-m depths. In addition, both record a low moisture content zone between 0- and 2-m depth.

One obvious discrepancy between neutron and GPR measurements occurs at the center access tube near the surface. This discrepancy is likely due to bentonite backfilling of the annulus around the center access tube that results in a higher retention of water in smaller pores. The neutron probe's sphere of influence decreases with increasing moisture content, and thus essentially takes a point measurement within the bentonite. The reason the GPR measurements do not record this small zone of high moisture content is that this area is poorly resolved, as will be further discussed in section 5.3.1.

The accuracy of GPR moisture content estimates was evaluated by comparing them to neutron measurements taken at the same borehole. Borehole B was chosen for this accuracy check. However, any of the other four boreholes could have been chosen since they exhibited the same general trends. In this study, the neutron values are considered the standard, since the neutron probe is a proven method of obtaining moisture content values. In Figure 23, both GPR borehole and neutron point measurements are plotted versus depth. Error bars are included for each measuring technique and were calculated based upon all the available GPR and neutron pre-

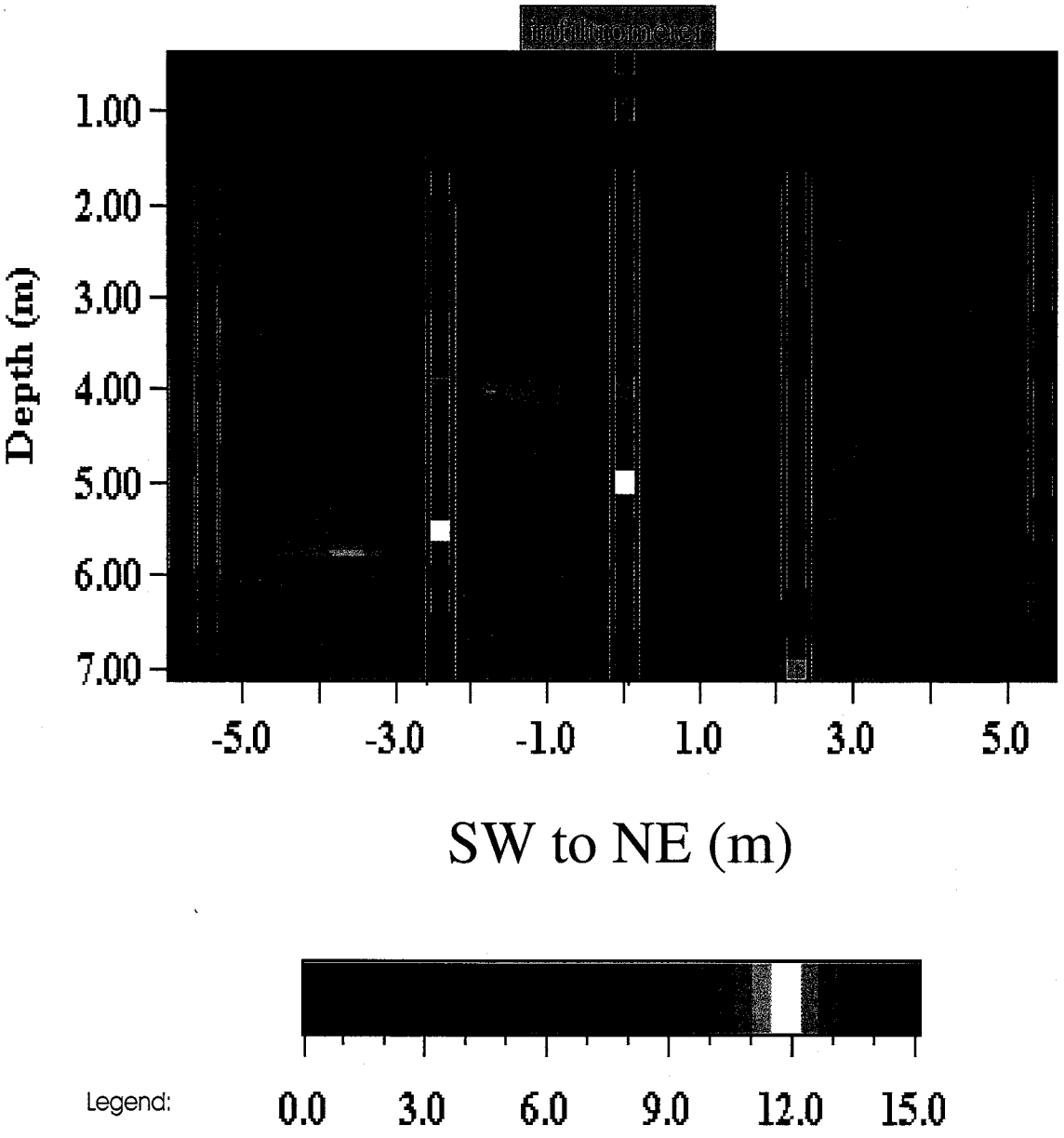

Figure 22. GPR mean pre-infiltration moisture content image with neutron moisture well logs superimposed on image. The moisture content scale is the same for both techniques.

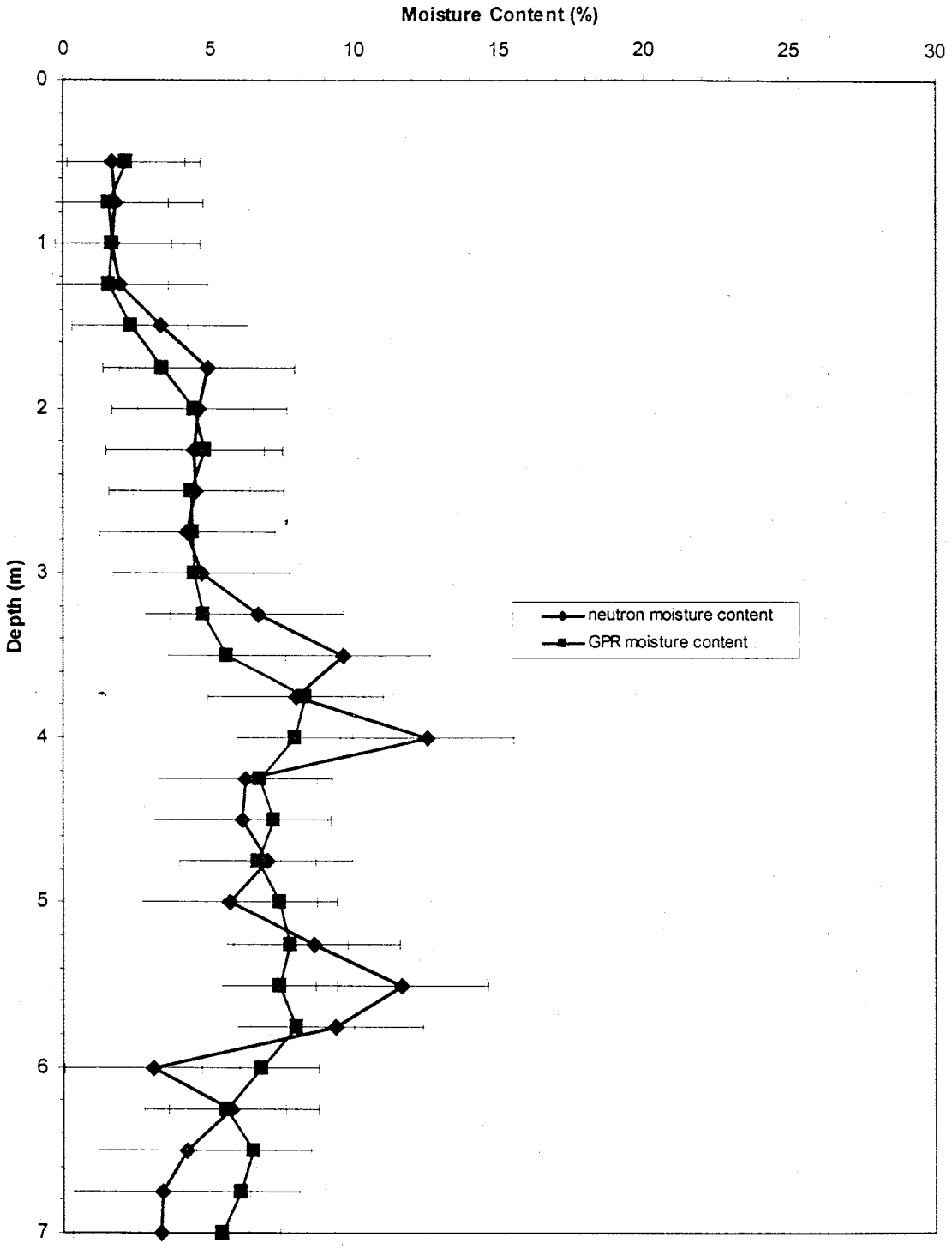

Figure 23. GPR and neutron probe pre-infiltration moisture content measurements versus depth for access tube B. Error bars included for both techniques. Data taken on 1/22/99.

infiltration data. The absolute error bars for GPR measurements are ± 2% moisture content and ± 3% moisture content for neutron measurements. Both sets of error bars were calculated from two standard deviations and therefore represent 95% measurement variability. The neutron error bar calculations are discussed in section 3.3. GPR error bar calculations are described in the following section.

The two sets of measurements are very consistent; however, the GPR does not measure the extreme high and low moisture content values that the neutron probe measures. If the error bars are included in the comparison between the two different methods, the measurements overlap in all cases. Thus, the moisture contents determined by the two methods are indistinguishable.

5.3 GPR Ray Density and Error Analysis

5.3.1 GPR Ray Density

Figure 24 is an image of the 2-D ray density of the first pre-infiltration data set. The other four pre-infiltration ray density images illustrate the same features as in Figure 24 and are contained in Appendix 4. The ray density for each cell is calculated by taking the total length of all the rays in the specific cell and then dividing that by the cell size. In our case the cell size is 0.25 m on a side which is based upon the level of resolution possible with a 0.25-m sampling interval. The EM rays take the fastest path between the transmitter and receiver. Therefore the rays curve around areas of low velocity or high moisture content. As a result the ray density is a function of the in-situ moisture content distribution and is not symmetrical.

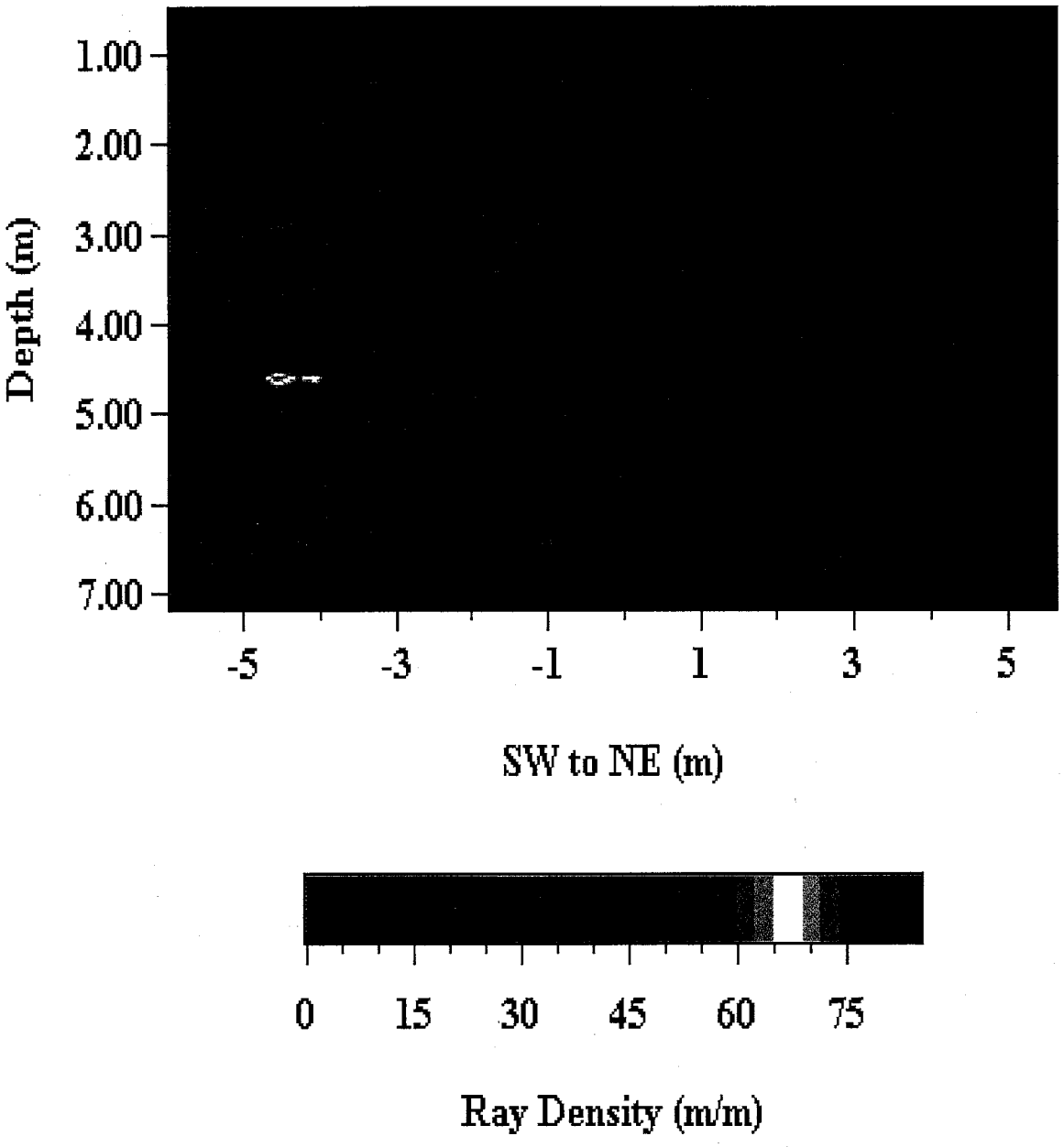

Figure 24. Ray density image for GPR pre-infiltration data set taken on 11/24/98.

Electromagnetic rays transmitted near the surface travel in the earth-air interface at the faster velocity of air, leaving few rays to travel between 0 to 1-m depth. Therefore, the upper meter has a low ray density and is poorly resolved. In general, however, the GPR image of the upper meter correlates well with the neutron measurements, except around the center well.

In addition to the upper meter, other low ray density areas occur at depths of 2 to 3, 4, and 5 to 6 m where low velocity or high moisture content areas exist. The southwest area exhibits the largest low ray density areas. In general, the high moisture content areas are poorly resolved and the low moisture content areas are well resolved. The level of resolution is important when evaluating the accuracy of the GPR images. This point will be revisited in the next section and in the next chapter.

5.3.2 GPR Error Analysis Results

By taking multiple baseline data sets, one is able to quantify the GPR precision error. The error was estimated by calculating the standard deviation of the travel time and the moisture content data for the five data sets. Since both the errors in the original data and the resulting moisture content images are determined, the translation of error from the raw image to the final image can also be determined in a general sense. Two standard deviations were calculated to represent 95% data variability. For the travel time error analysis, each well pair travel time was evaluated separately (Figures 25 a-d). The transmitter positions are plotted versus the receiver positions with zero representing the ground surface. The white areas in the upper left and lower right areas of the figure are blank due to the 45-degree data acquisition angle described in section 4.2.1. Bands of missing data are due to bad transmitter positions or noisy data in one of the five data sets.

A color scale is used to represent the two standard deviations and the scales vary with each well pair.

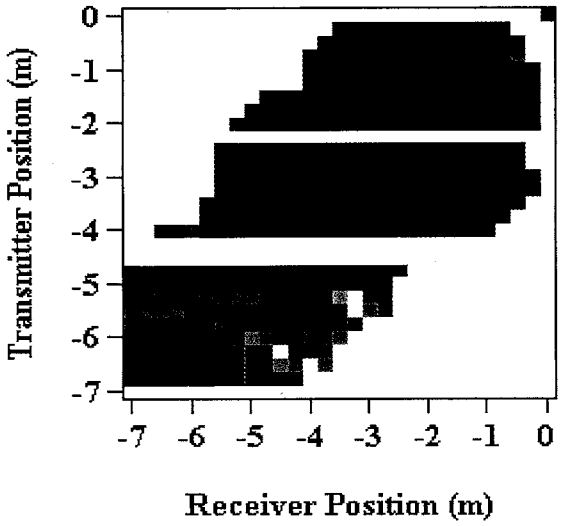

Figure 25a. Well pair AB

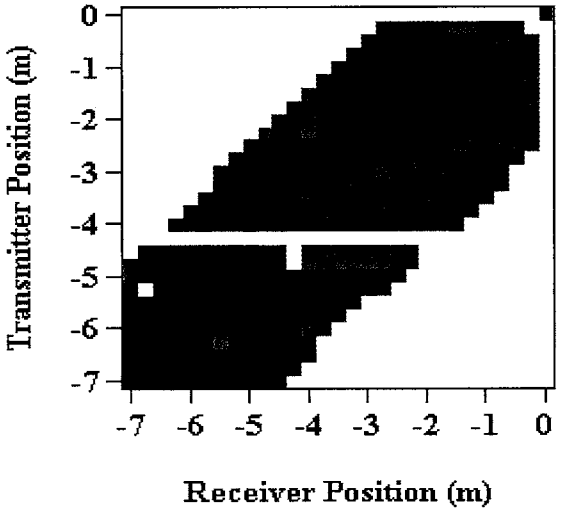

Figure 25b. Well pair BC

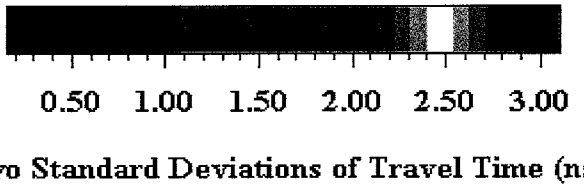

Figure 25a-b. Pre-infiltration travel time error analysis for well pairs AB and BC.

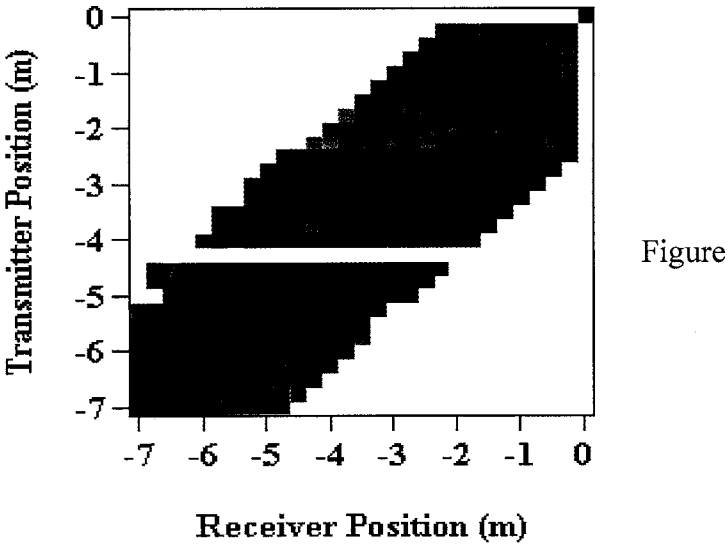

Figure 25c. Well pair CD

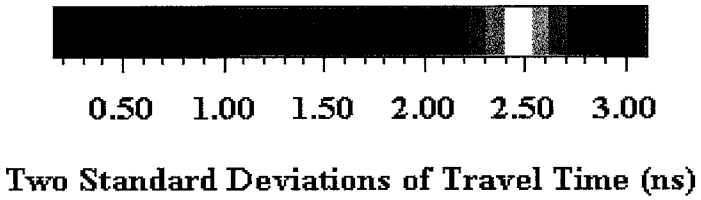

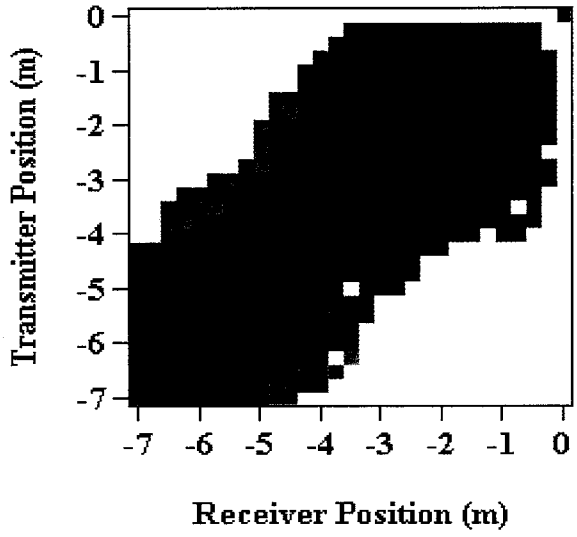

Figure 25d. Well pair DE

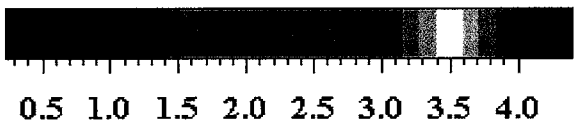

Figure 25c-d. Pre-infiltration travel time error analysis for well pairs CD and DE.

The average two standard deviations for each well pair are AB-1.62 ns, BC-0.81 ns, CD-0.89 ns, and DE-0.95 ns, and the overall two standard deviations for all four well pairs is 1.08 ns. Well pair AB has the highest error, which occurs when the transmitter is between 5.2 to 7 m and the receiver is between 3 to 5 m. The high error is due to one bad data set that had both significantly higher and lower travel times than the other four data sets.

Figure 26 shows two standard deviations of the moisture content variability displayed in the same format as the moisture content images. The absolute moisture content error ranges from 0 to 2.5 %; however, the majority of the values are less than 2%. Therefore, 95% of the time, GPR measurements have associated errors of ± 2% absolute moisture content. Higher error generally correlates with areas of higher moisture content or low ray density. For example, the highest error (2.5%) is found at 4-m depth where the first high moisture content layer occurs. In addition, the error is higher in the southwest around 4 and 6m where the two high moisture content layers occur. In the northeast area the higher error is more widespread, as is the higher moisture content. Overall, an average traveltime error of ± 1.08 ns generally translates to an average moisture content error of ± 2 %.

Once the baseline moisture content distribution and the measurement error was established, infiltration began and weekly measurements were taken in order to image the advancing wetting front. Results from these measurements are described in the next chapter.

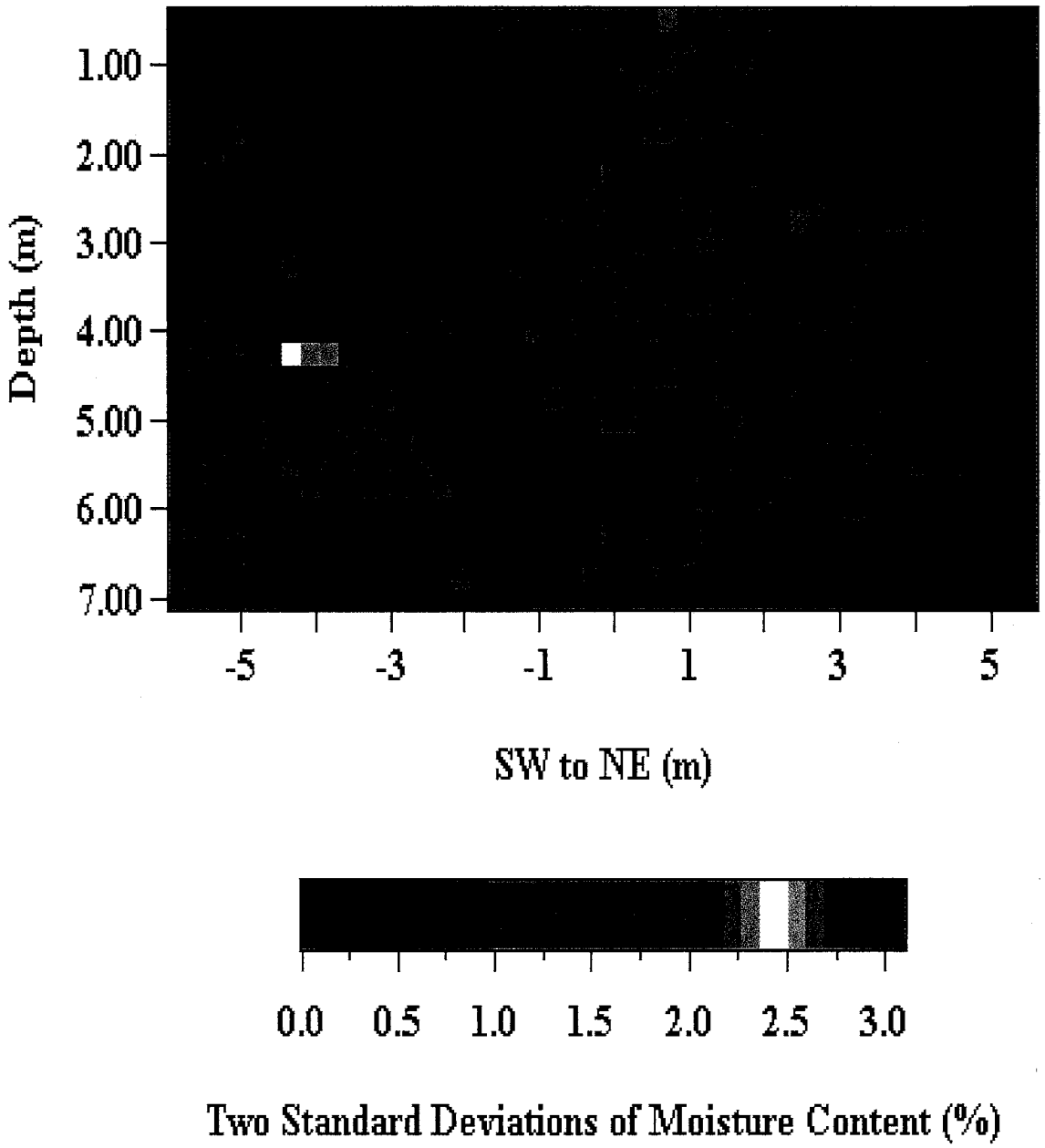

Figure 26. Moisture content error analysis: two standard deviations of five pre-infiltration GPR moisture content images.

6.0 INFILTRATION RESULTS AND DISCUSSION

6.1 Infiltration Schedule

Infiltration began on March 11, 1999 at noon and occurred twice daily for five minutes each at 12-hour intervals. The overall daily flux was approximately 2.7 cm/day. Infiltration is still occurring, however measurements taken for this thesis ceased on July 27, 1999.

6.2 GPR Raw Image Results and Discussion

Figures 27a-i show the mean pre-infiltration GPR moisture content image and eight infiltration images. The location of the infiltrometer is indicated at the top of each figure. Bottom time shifts were applied to each of the images as described in section 4.2.1. Corresponding images created without a time shift are provided in Appendix 5. Most time shifts were negative. However, for the 42-day image, a positive time shift was calculated for the DE well pair between 2.25 and 5.5-m. The time shift resulted in an increase of moisture content most noticeable from 1.5 to 7-m depth. The positive time shift may not be appropriate, especially since later images do not show the same increase in moisture content. Therefore, a second image was created in which a bottom time shift was applied to all of the well pairs except well pair DE (Figure 27h).

The GPR images illustrate that the wetting front has progressed vertically to 3 m after 8 days with only slight lateral spreading. After 14 days the wetting front has reached the first silt, sand, and clay nodule layer at 4 m. By 21 days the wetting front has reached the lower clay layer at 6-m depth. After 28 days the wetting front increased moisture content values to 15% in the center of the image. Increases in moisture content are evident at depths of 5 to 6 m in the 35-day image.

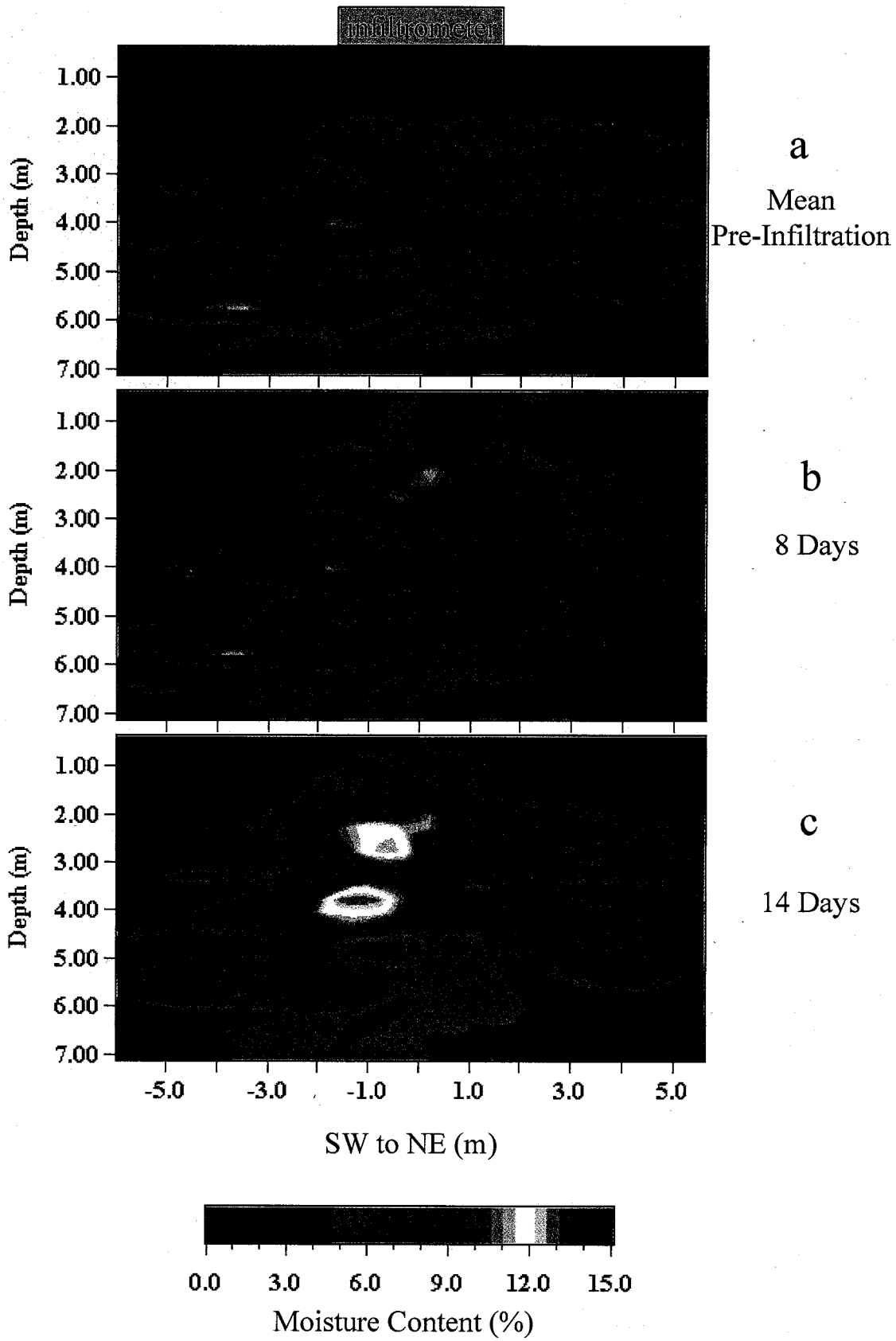

Figure 27a-c. GPR moisture content images: mean pre-infiltration to 14 days after infiltration began (with bottom time shift applied).

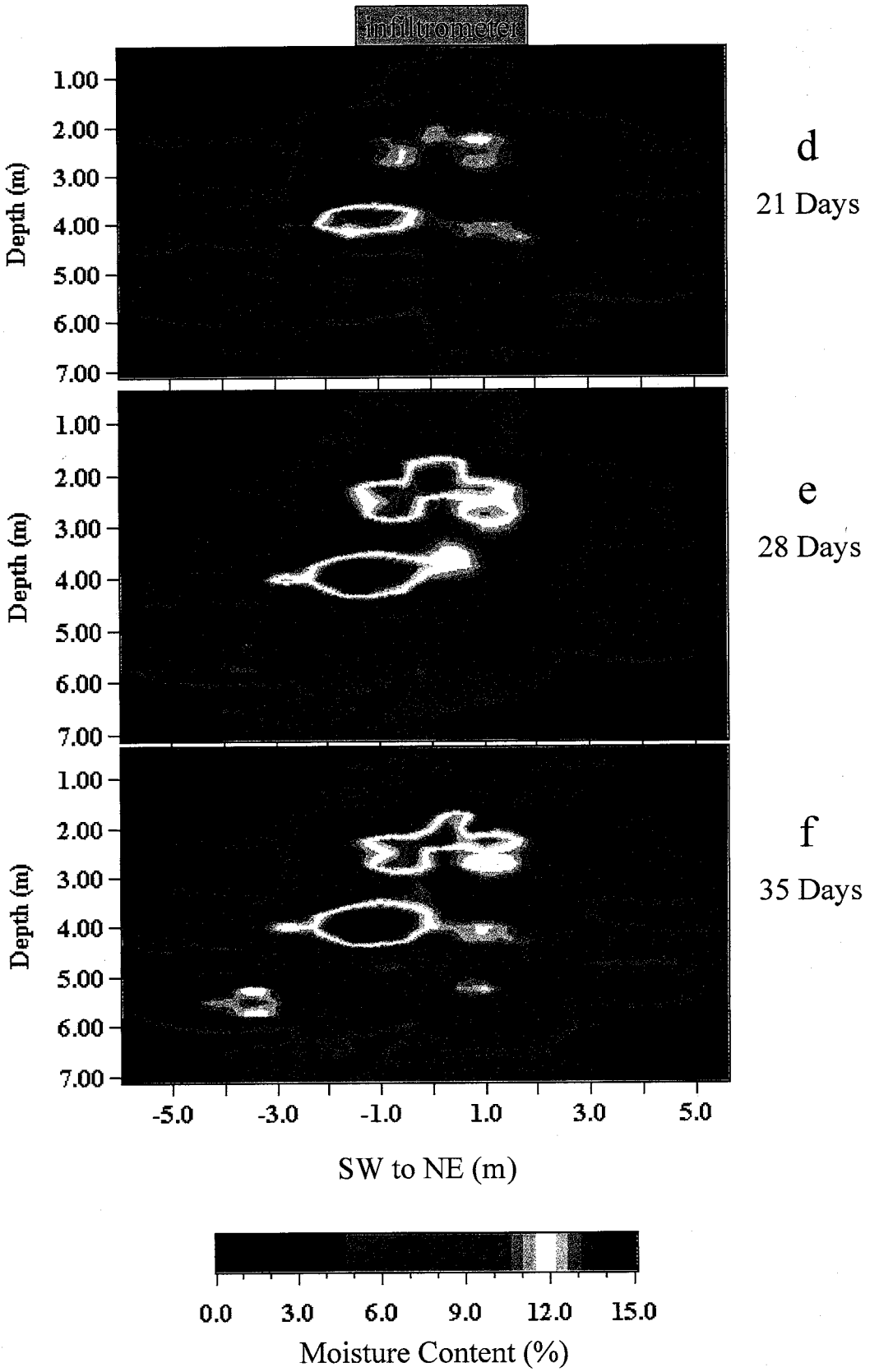

Figure 27d-f. GPR moisture content images: 21-35 days after infiltration began (bottom time shift applied).

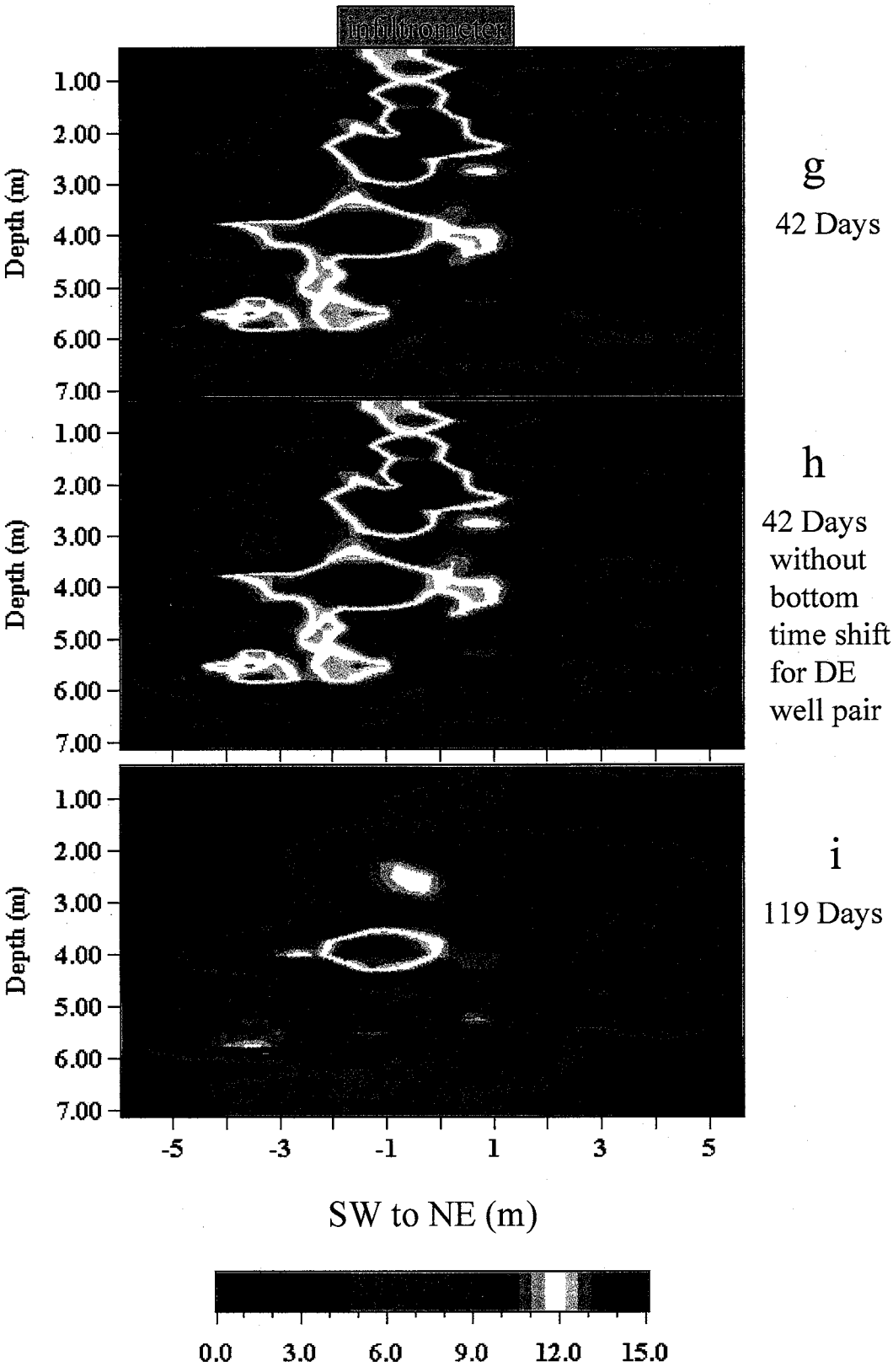

Figure 27g-i. GPR moisture content image: 42-119 days after infiltration began (bottom time shift applied).

The 42-day image shows a dramatic increase in moisture content which decreases significantly in the 119-day image. The accuracy of the 42-day image is questionable due to the previously mentioned connection problems during data acquisition. In addition, the 119-day image is dryer in some areas than the 28, 35, and 42-day images, indicating that the GPR problems may have begun earlier than was initially thought. The primary area of disagreement occurs in the center of the image from 1 to 3-m depth. With the exception of the 42-day image, the moisture content from 5 to 7-m depth in the 119-day image is generally greater than the moisture content at the same depth in the earlier images.

By comparing the mean pre-infiltration image to the 119-day image, the increase in moisture content is contained laterally between –2.8 m to 2.5 m along the SW to NE line. Since the infiltrometer extends from –1.5 to 1.5 m, the infiltrated water only spread 2.3 m laterally. Vertically however, the added water has traveled 7 m. The raw images illustrate a general location of the wetting front. However, the exact location is difficult to determine from these images.

6.3 GPR Normalized Image Results and Discussion

Normalized images were created in order to determine the exact location of the wetting front (Figures 28a-h). The images represent the temporal change in moisture content from the mean pre-infiltration moisture content values. The scale for the change in moisture content ranges from –10 % to 10% in which red represents a positive change. Since the GPR has a ± 2% moisture content error, changes greater than a 2% represent a significant change in moisture content.

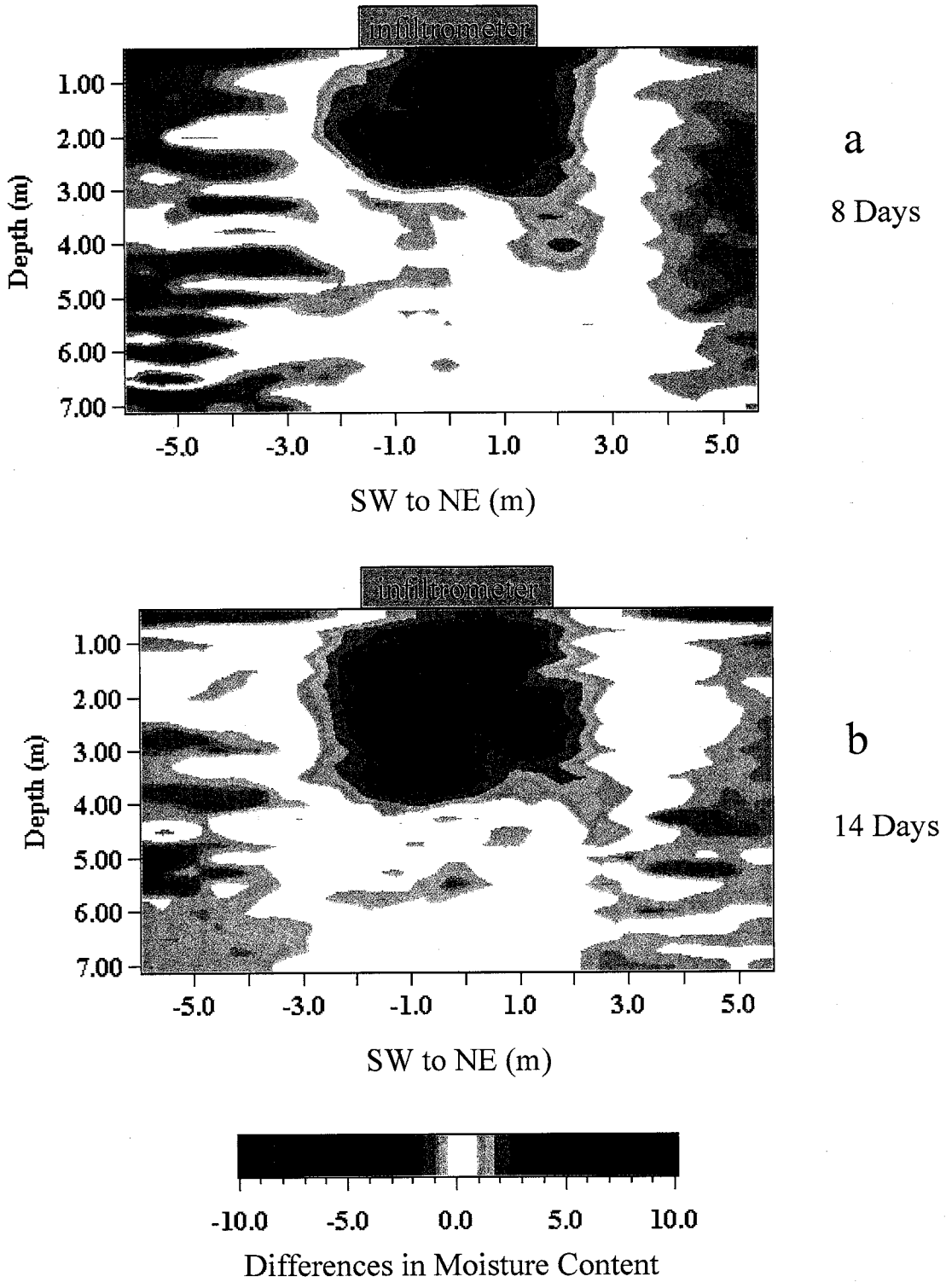

Figure 28a-b. GPR normalized moisture content images 8 and 14 days after infiltration began (bottom time shift applied).

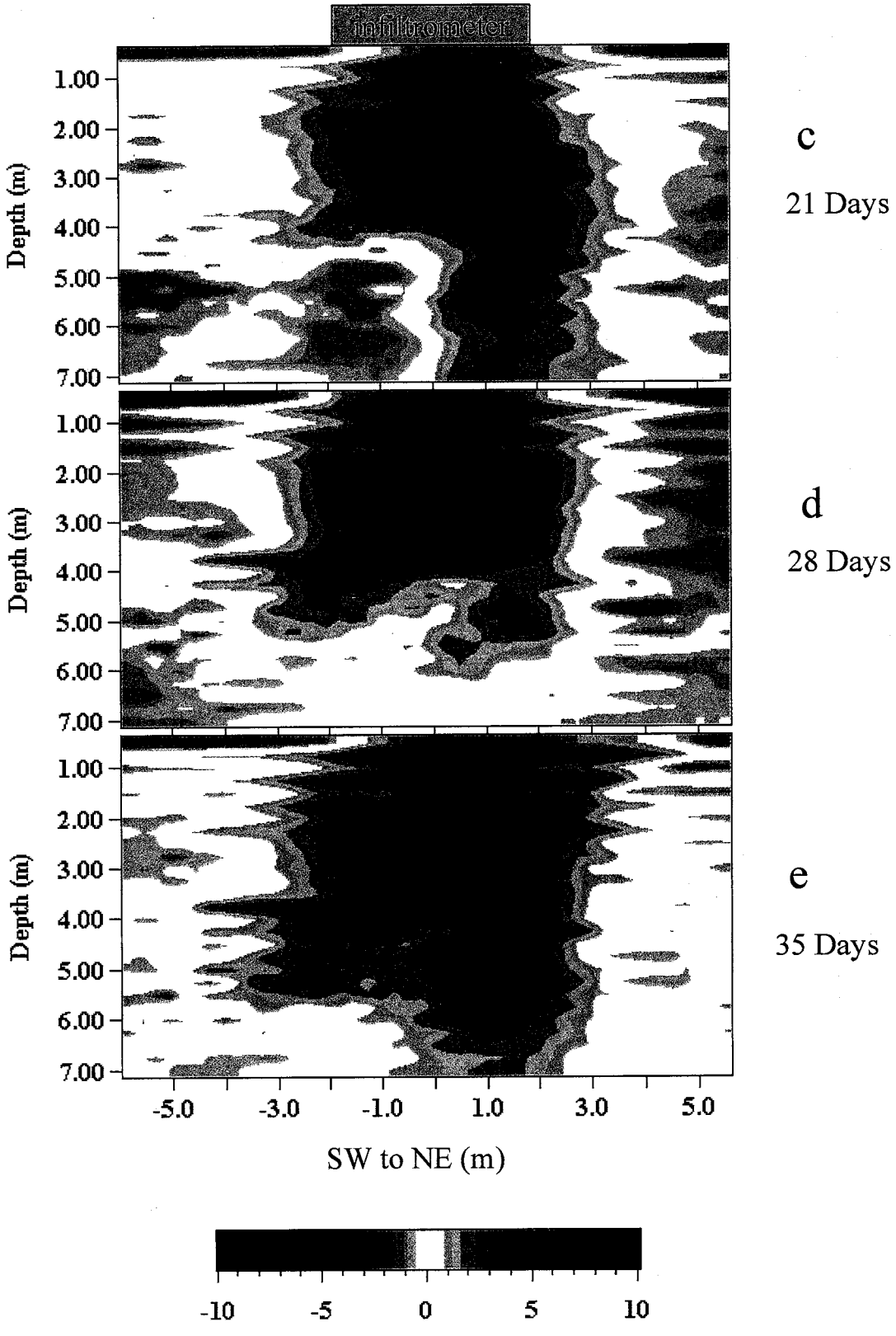

Figure 28c-e. GPR normalized moisture content images 21-35 days after infiltration began (bottom time shift applied).

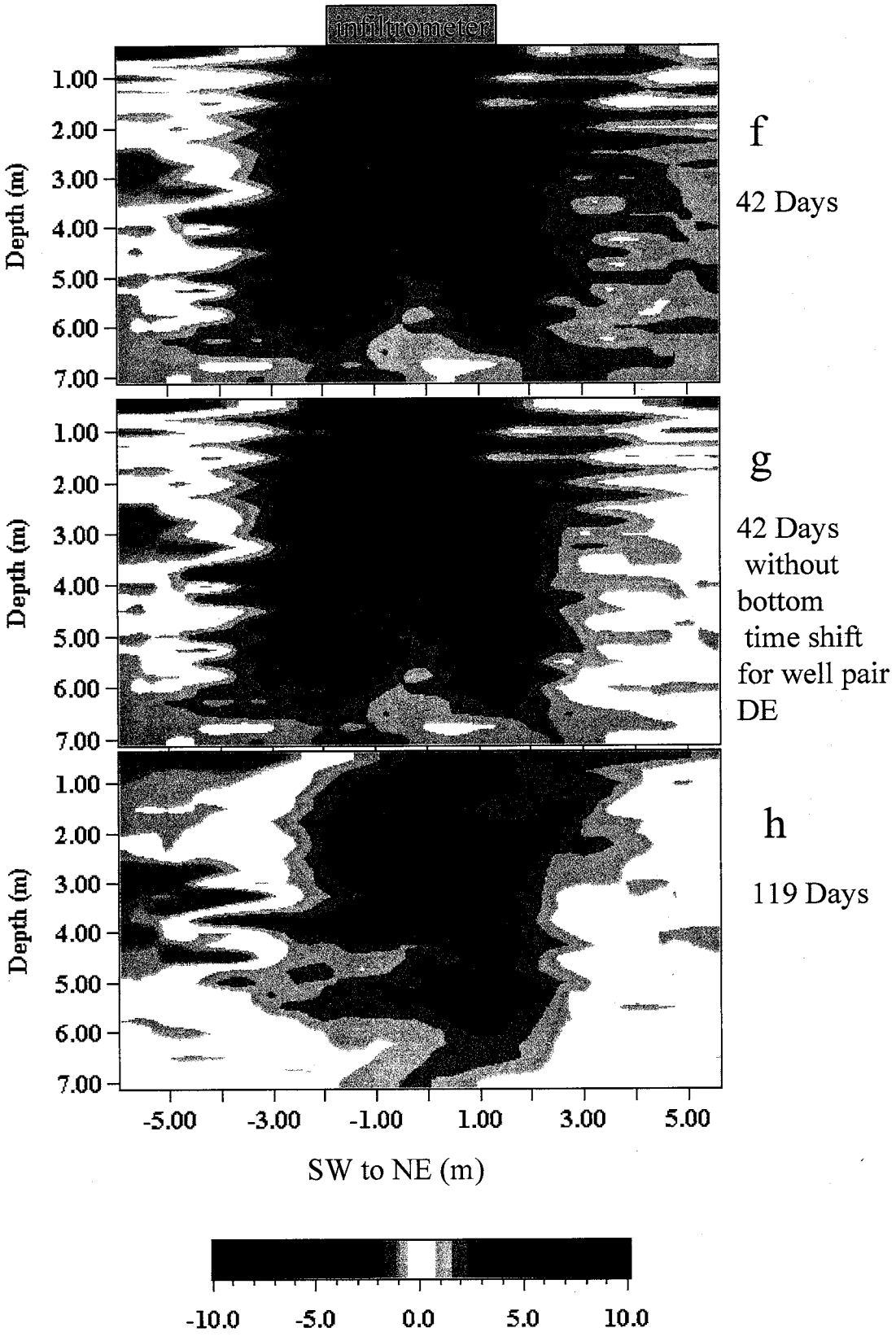

Figure 28f-h. GPR normalized moisture content images 42 and 119 days after infiltration began (bottom time shift applied).

According to the normalized images, after 8 days the wetting front has generally progressed to 3-m depth. However, in the northeast area the wetting front has progressed to 4-m depth. After 14 days, the wetting front has progressed to 4-m depth. In 21 days the wetting front has moved to 4.5-m depth in the southwest area, and down to 7 m in a portion of the northeast area. The 28-day image indicates that the wetting front has only advanced to approximately 5.5-m depth. The discrepancy between the wetting front images for 21 and 28 days is puzzling. In the 21-day image, the well pair from 0 to 2.25-m (SW to NE line) shows a positive moisture content change of about 4 to 6 % along the entire depth range. The uniform positive moisture content change may be attributed to an error in the data acquisition or in processing of this well pair. Another possible reason is preferential flow around the access tubes. However, this would not explain the high moisture content in the area between the access tubes.

The 35-day image indicates that the wetting front has reached 6 m in part of the SW area and 7 m in part of the NE area. Again, two 42-day images were created. Figure 28f with an applied time shift for all the well pairs shows considerable lateral spreading to the northeast. The 42-day image without the DE well pair time shift shows a more confined wetting front. The unusual positive time shift, the confined geometry of the wetting front before and after the 42-day image, and data from the neutron probe all suggest that Figure 28g may be a more accurate image of the wetting front after 42 days of infiltration. This 42-day image (Figure 28g) shows the entire wetting front reaching 7 m. The 119-day image shows slightly less vertical and lateral movement of the wetting front than the 42-day image. In addition, the 119-day image does not show the extreme

positive changes (+10%) in moisture content that the 28-, 35-, and 42-day images show. However, the 119-day image also shows the water moving down to 7 m.

6.4 GPR Ray Density Image Results and Discussion

Ray density images were created for each data set (Figures 29a-h). Only one image was created for the 42-day data set, because the two ray densities were very similar regardless of the time shift applied. Although the infiltration ray density images are similar to the mean pre-infiltration image, several exceptions exist. One exception occurs after 8 days. The center low ray density area originally located at 1.5 to 2.5-m depth shifts down to 3 m in response to the advancing wetting front. Another noticeable difference occurs in the 28-day image. A large "hole" in the ray density image occurs from 2.5 to 6.5-m depth at 0 to 2.25 m along the SW to NE line. The images before and after both have higher ray densities in this area. The low ray density in the 28-day image implies a increased poorly resolved area. Therefore, the moisture content values from this area may be inaccurate. The exact cause of the temporary decrease in ray density at that depth is unknown. However, it is possible that the decrease resulted due to a bad connection in the GPR system or from a large number of noisy traces that were unusable for processing. Therefore the discrepancy between the 21 and 28-day images could be due to the poorly resolved area in the 28-day image. After 119 days, the ray density decreases at 6 to 7-m depth in the NE area from 0 to 2.25 m due to the advancing wetting front.

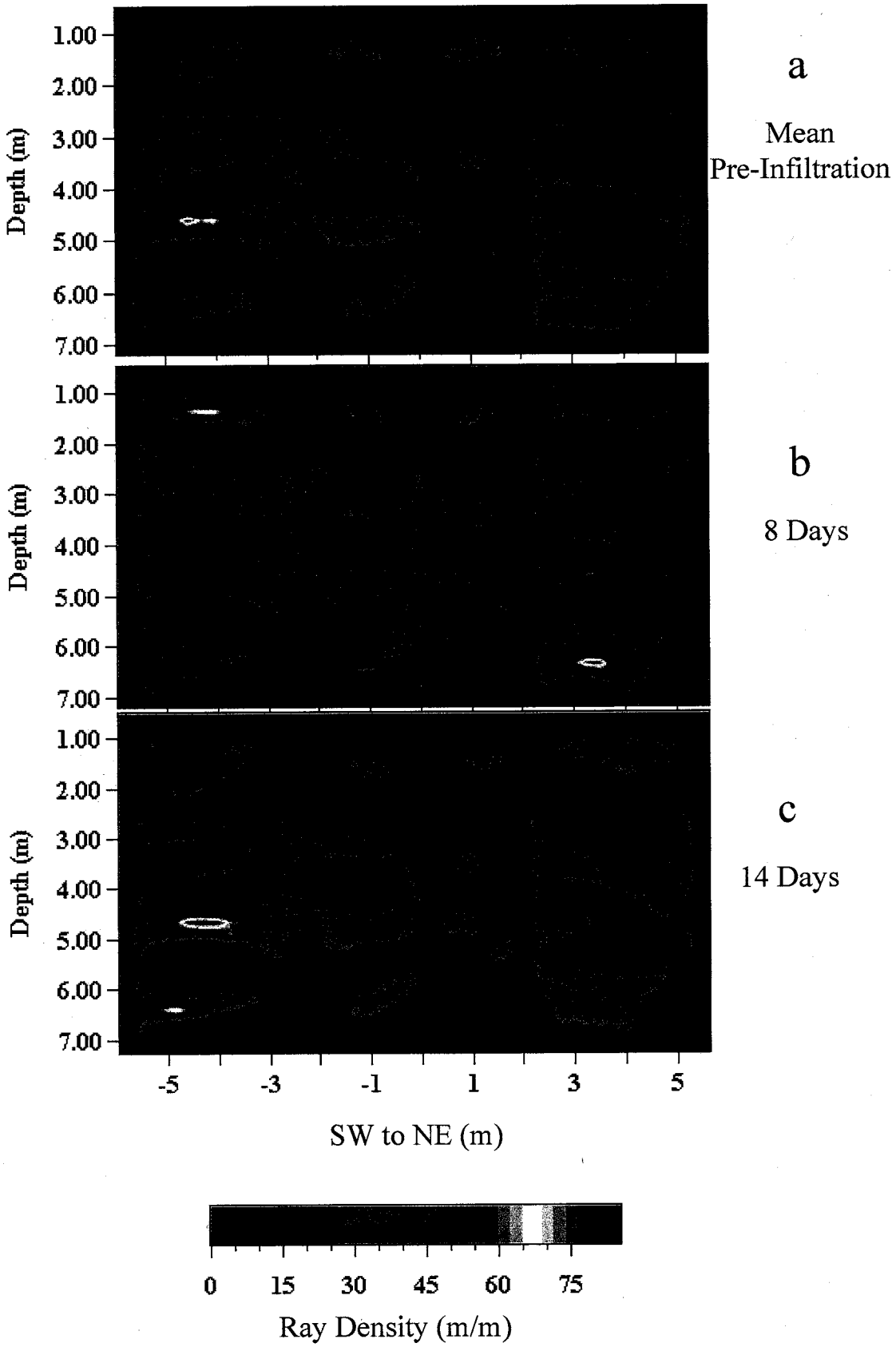

Figure 29a-c. GPR ray density images: mean pre-infiltration to 14 days after infiltration began.

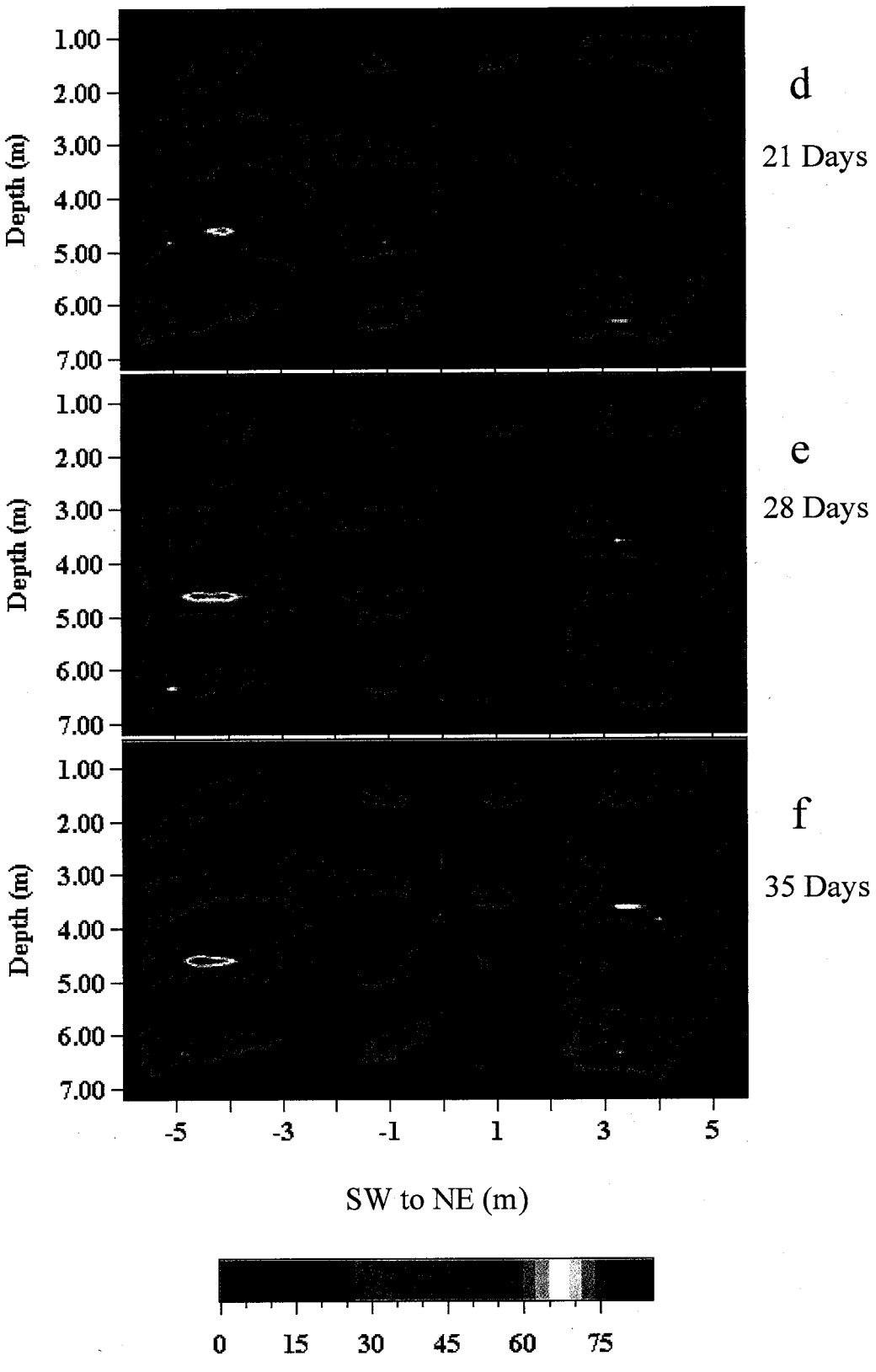

Figure 29d-f. GPR ray density images: 21-35 days after infiltration began.

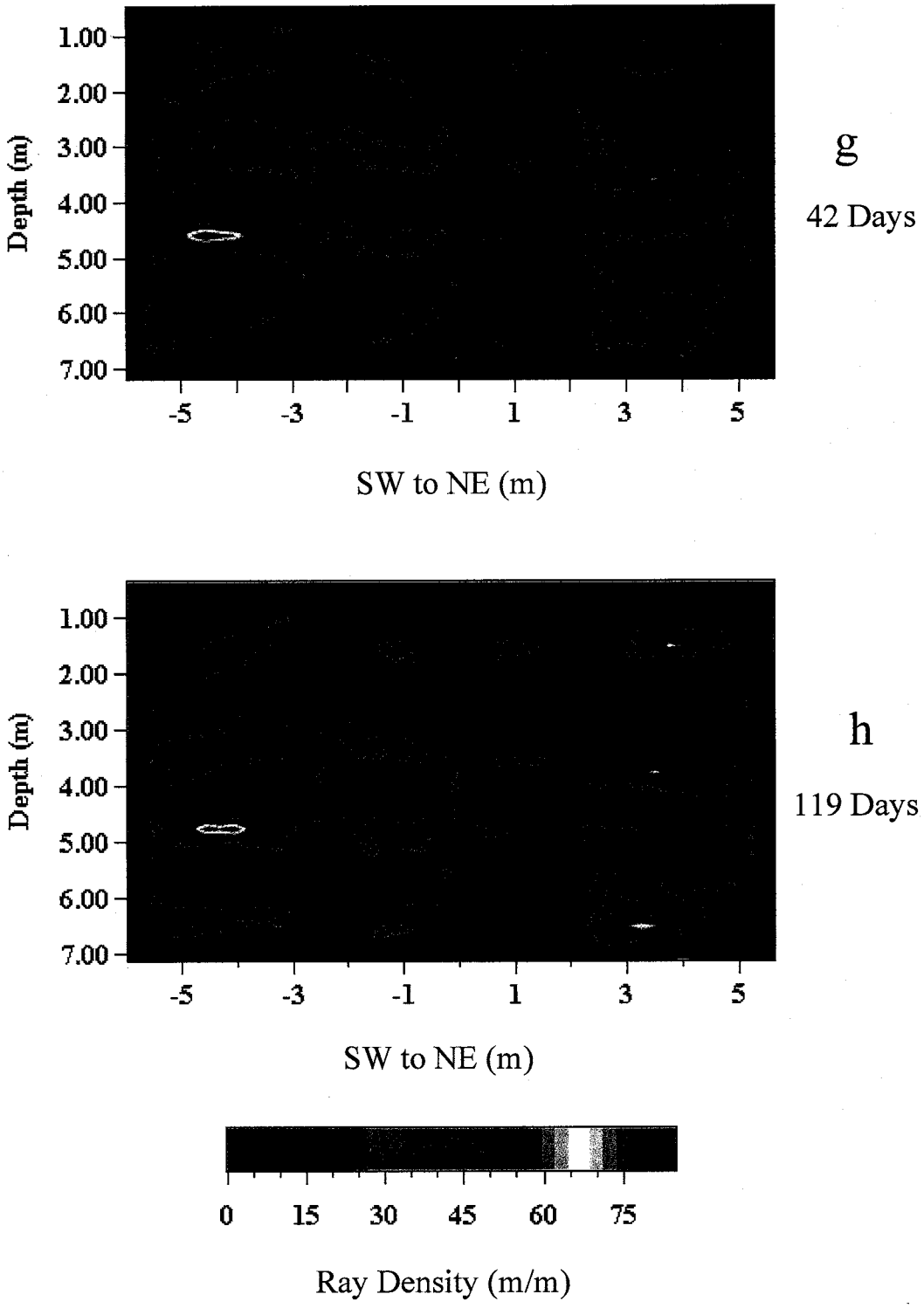

Figure 29g-h. GPR ray density images: 42 and 119 Days after infiltration began.

6.5 Comparison of GPR and Neutron Moisture Content Images

Figures 30-36 present the 7 infiltration GPR moisture content images with neutron moisture logs superimposed on the image. The GPR moisture content profile represents a smoothly varying image that maintains the general trend of the moisture content distribution according to the neutron probe. However, at the boundaries between high and low moisture content values, the GPR image appears to smear the values. For example the 8-day image (Figure 30) illustrates lateral and vertical GPR smearing. From 1.5 to 3-m depth, the GPR image indicates laterally smearing in the area of high moisture content in the center past the outer neutron logs. An example of vertical smearing can be seen by comparing the GPR image to the northeast neutron log at 3.5-m depth. The neutron probe records a low moisture content, whereas the GPR smears the high moisture content from above and below into one continuous high moisture content area. Lateral smearing is due to the smoothness constraints imposed within the inversion scheme, as well as the imaging limitations of the cross-borehole imaging geometry. Since the inversion process is ill-posed, unstable, and non-unique due to noisy data and a limited amount of data, smoothness constraints are imposed to help stabilize the inversion scheme and reduce non-uniqueness (Sharma, 1997). The imaging limitations arise because in order to recover an exact image of the region of interest, the data collected during the experiment must completely surround the region (Kak and Slaney, 1988). Therefore, because data are only available on two sides of the region (i.e., the two boreholes), lateral smearing results. Vertical smearing is a result of smoothness constraints and possible resolution constraints of the100 MHz frequency.

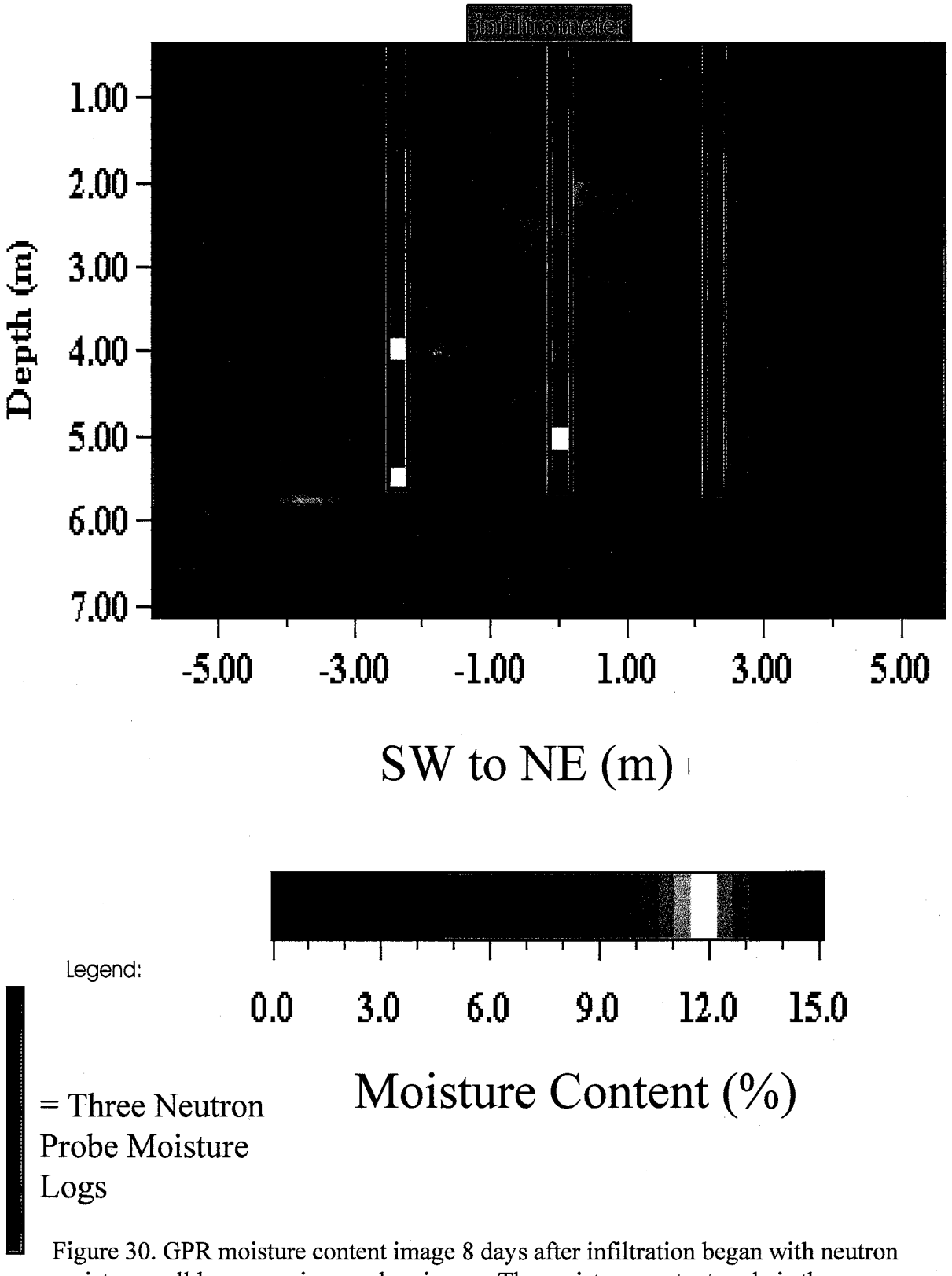

Figure 30. GPR moisture content image 8 days after infiltration began with neutron moisture well logs superimposed on image. The moisture content scale is the same for both techniques.

With the exception of smearing, the GPR and neutron measurements are in general agreement with only minor discrepancies. In the 8-day image, both the GPR and neutron probe record high moisture content areas at approximately 2-, 4-, and 5-m depths. However, the neutron moisture content values at 4 and 5 m are slightly higher than the GPR values. After 14 days, both the GPR and neutron probe measurements indicate an increase in moisture content at 2.5- and 4-m depths. In the GPR image, the increase in moisture content is present as a layer, whereas the neutron probe records just a point of high moisture content. After 21 and 28 days, the moisture content continues to increase at 4-m depth. In 28 days, the GPR image also shows a substantial increase in moisture content from 2 to 3-m depth that is sensed by the neutron probe as an area of only 0.25 m^2. After 35 days, the high moisture content at the 2 to 3-m depth area has decreased slightly according to the GPR. However, both the GPR 28- and 35-day images show higher moisture contents at 2- to 3-m depth than the corresponding neutron measurements. The discrepancy between the neutron and GPR measurements indicate that instrument problems may have led to an overestimation of moisture content. Instrument problems could have begun before 42 days of infiltration but went unnoticed due to a smaller magnitude of error. Poor antenna connections caused reduced signal amplitudes that made picking the first arrival more difficult and possibly led to inaccurate first picks.

In the 35-day image, the moisture content is increasing between 5 to 6 m, according to both neutron and GPR measurements. In the 42-day image the GPR results show a significant increase in moisture content at 1 to 3, 4, and 5 to 6-m depths. The GPR moisture content values at 4 and 5 to 6-m depth correlate fairly well with the neutron

values. However, at 1 to 3-m depth, the GPR values overestimate the moisture content according to the neutron values. In the 119-day GPR image, the moisture content at the three previously mentioned depths has decreased significantly. This again suggests that instrument problems were the cause of the overestimation of moisture content prior to the 119-day image. Overall, the GPR and neutron moisture content values are in general agreement with only isolated discrepancies.

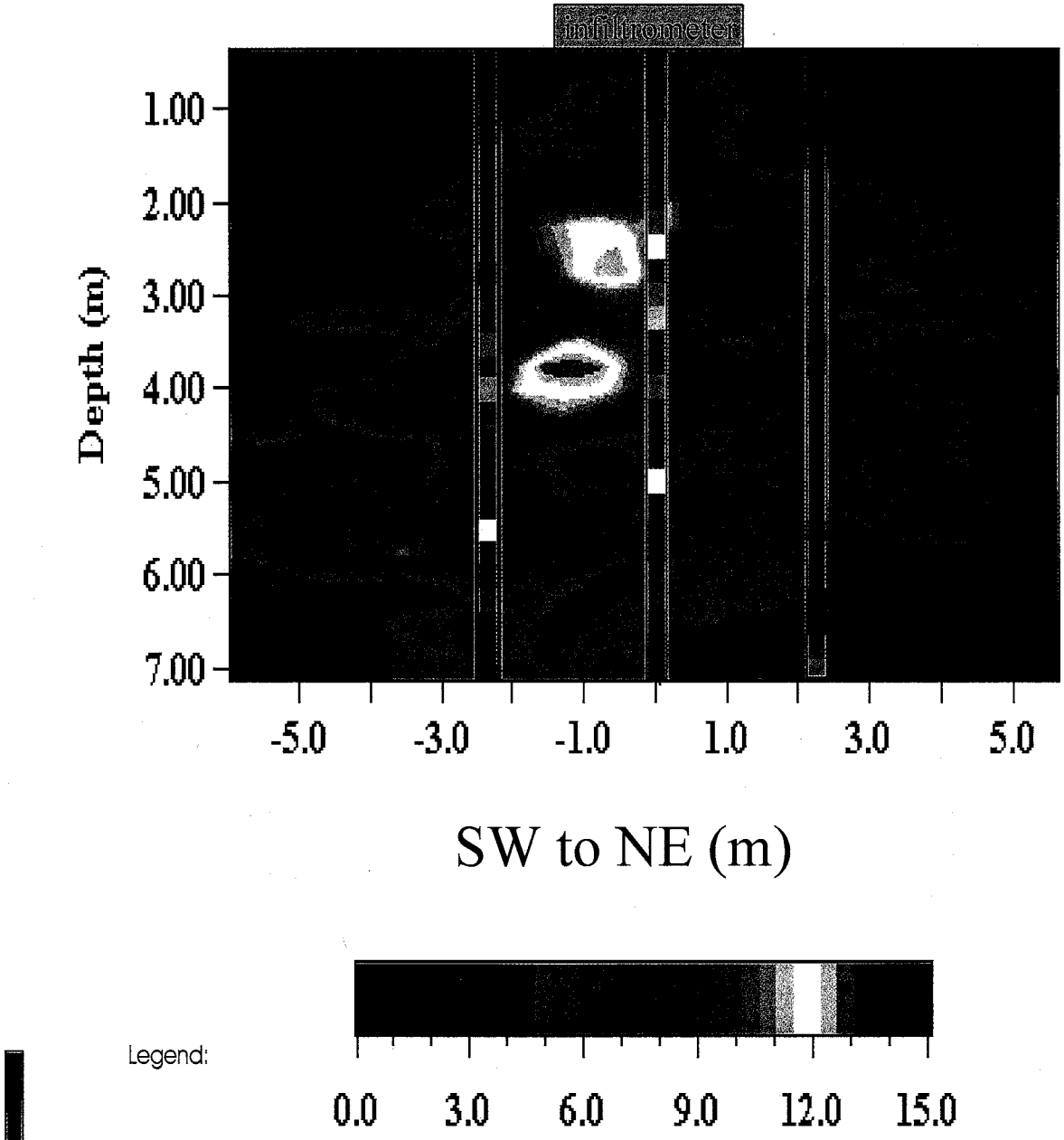

Figure 31. GPR moisture content image 14 days after infiltration began with neutron moisture well logs superimposed on image. The moisture content scale is the same for both techniques.

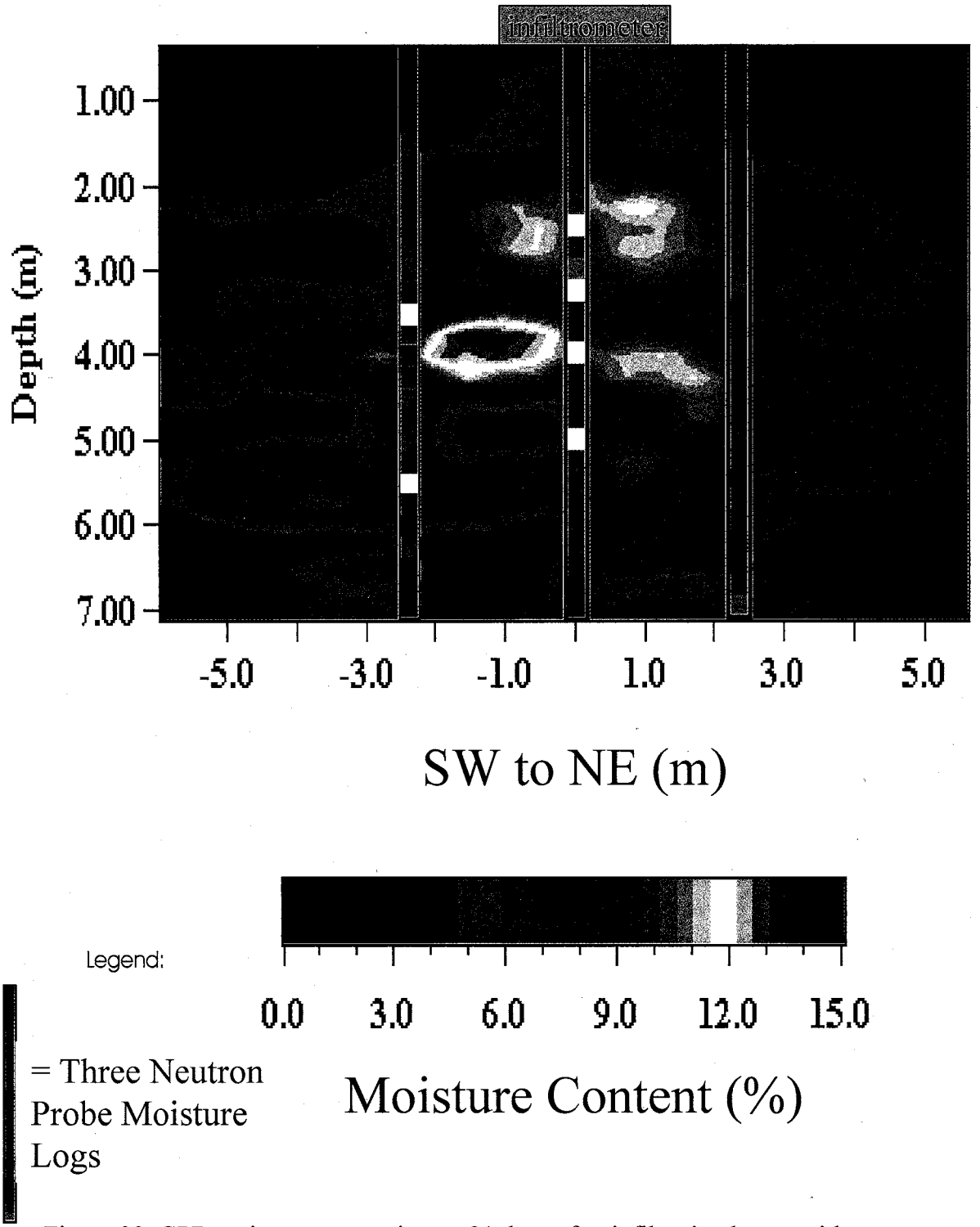

Figure 32. GPR moisture content image 21 days after infiltration began with neutron moisture well logs superimposed on image. The moisture content scale is the same for both techniques.

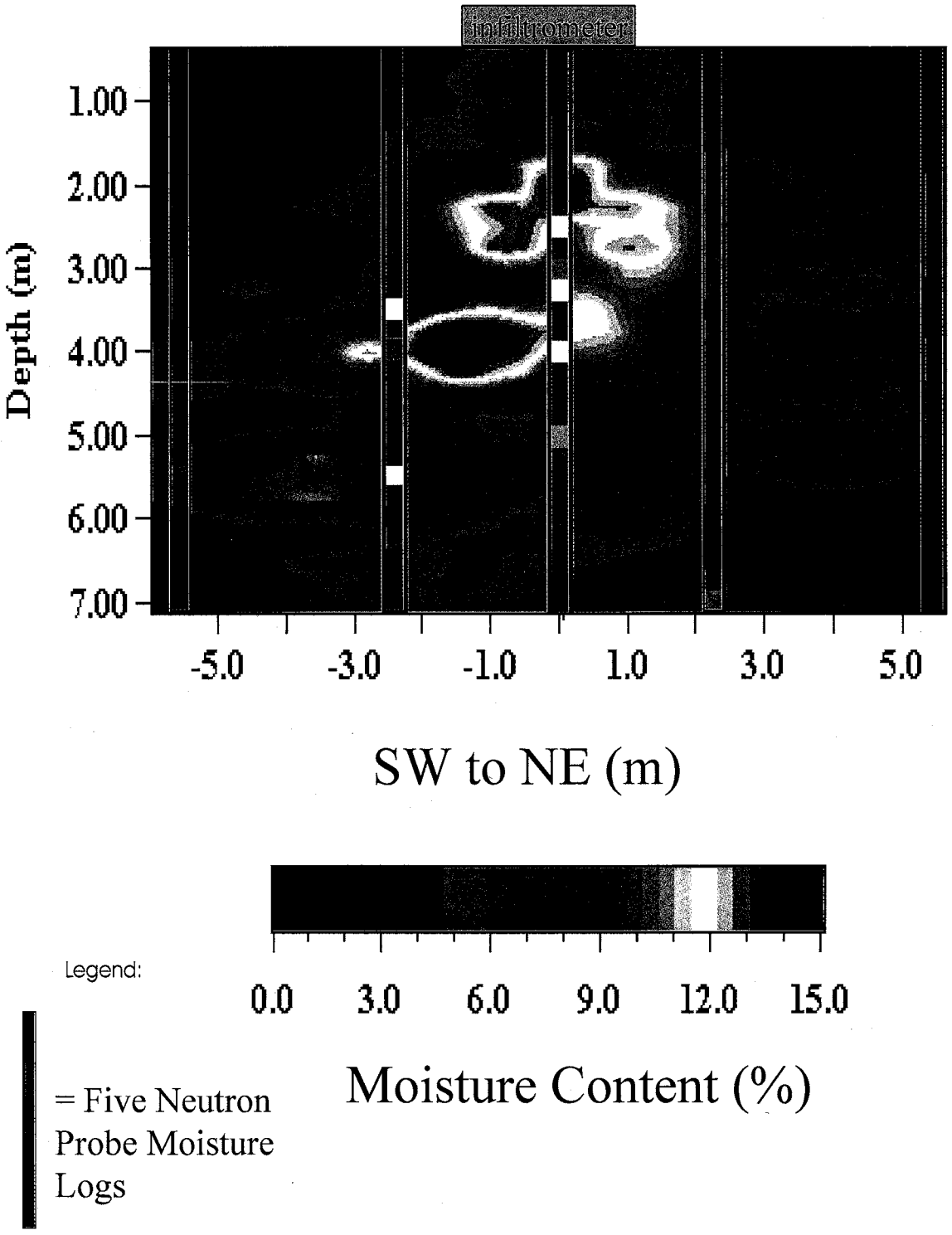

Figure 33. GPR moisture content image 28 days after infiltration began with neutron moisture logs superimposed on image. The moisture content scale is the same for both techniques.

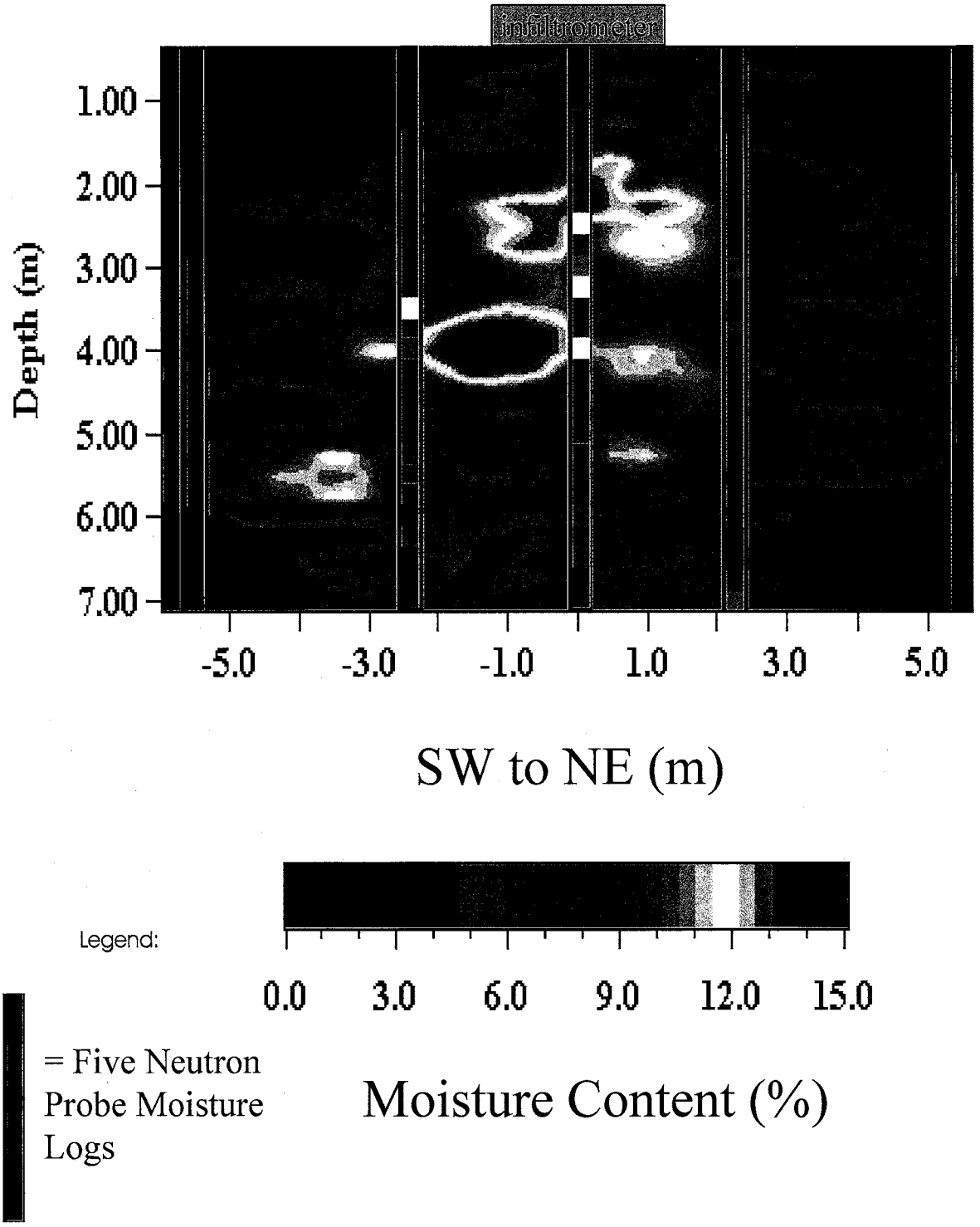

Figure 34. GPR moisture content image 35 days after infiltration began with neutron moisture well logs superimposed on image. The moisture content scale is the same for both techniques.

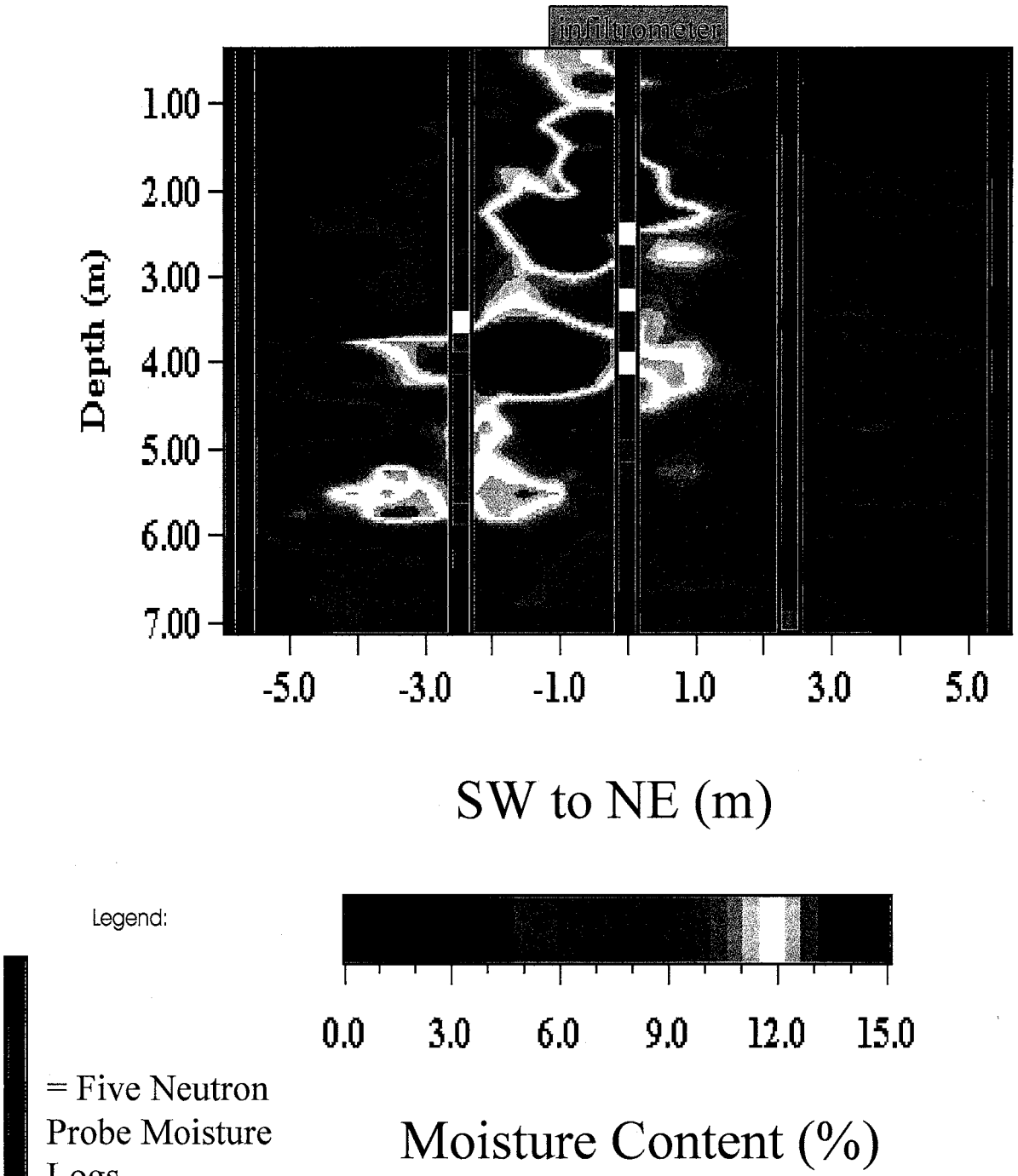

Figure 35. GPR moisture content image 42 days after infiltration began with neutron moisture logs superimposed on image. The moisture content scale is the same for both techniques.

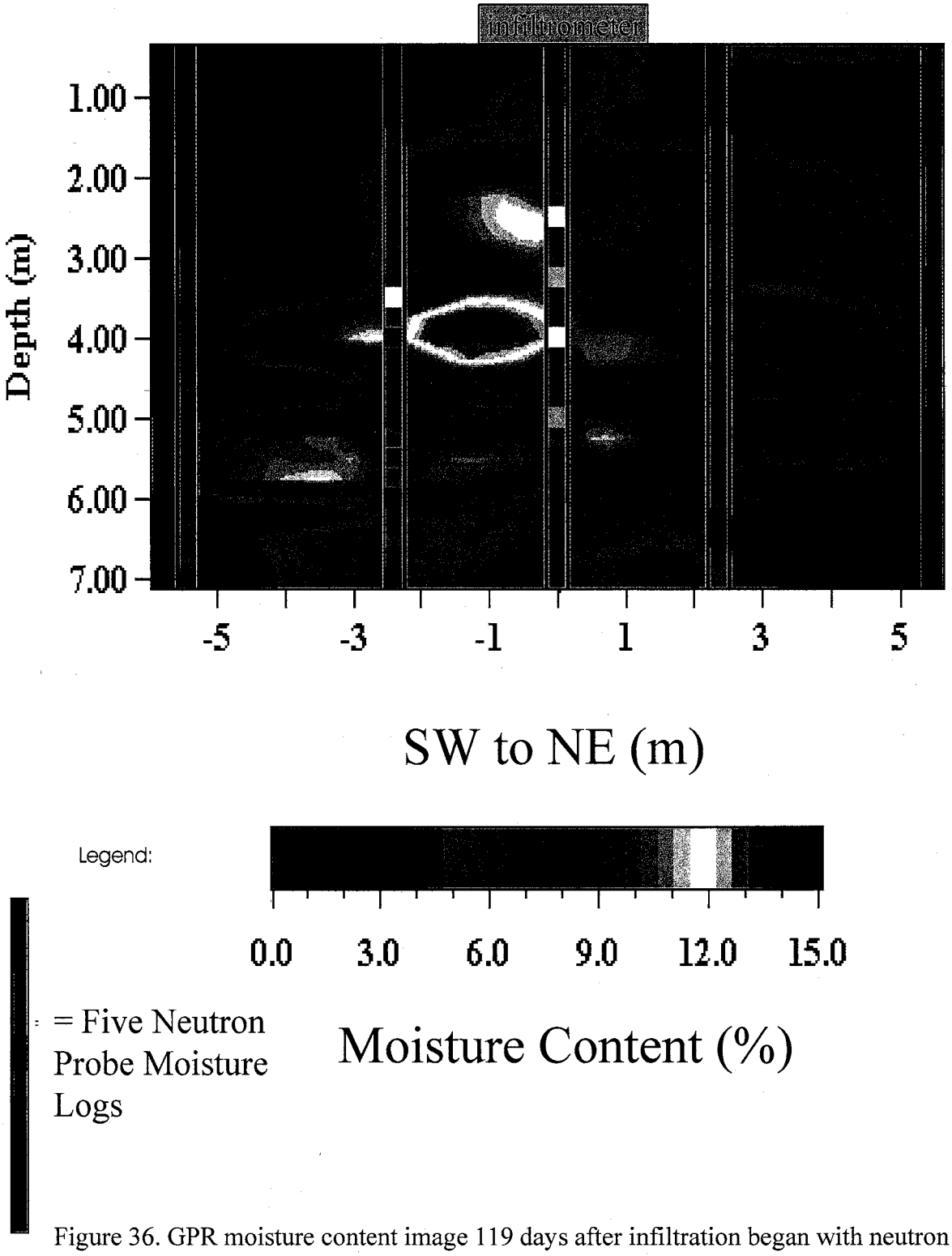

Figure 36. GPR moisture content image 119 days after infiltration began with neutron moisture well logs superimposed on image. The moisture content scale is the same for both techniques.

Figures 37-43 graphically compare the GPR and neutron measurements taken within access tube B for each of the seven infiltration data sets. The two sets of measurements correlate fairly well. Although the GPR does not measure the extreme high and low values recorded by the neutron probe, the GPR does measure the general trend of moisture content values according to the neutron probe. If the error bars are included as part of the measurement value, the GPR and neutron measurements overlap 100% of the time with the exception of one data set. The exception occurs in the 42-day image (Figure 42), where the values overlap 96% of the time. In Figure 42, the GPR measurements generally overestimate the moisture content. In addition, in all of the 42-day figures (28g+h, 29f+g, 36, and 43) the GPR moisture content is higher than the corresponding neutron values and the later GPR image values. However, in the 119-day image the GPR and neutron values are extremely similar, indicating that the GPR system problems were fixed. Overall, the GPR and the neutron probe measure the same moisture content values.

7.0 CONCLUSIONS

Pre-infiltration comparisons with both neutron moisture logs and stratigraphic column data indicate that, in general, cross-borehole GPR can accurately image the 2-D in-situ moisture content distribution in the vadose zone. A few exceptions exist. First, within the uppermost meter, cross-borehole GPR is unable to image the sharp increase in moisture content around the center access tube as a result of the low ray density in this area. However, with the exception of the area around the center access tube, the GPR accurately images the upper meter according to both the neutron probe measurements and the stratigraphic column data despite the low ray density in this area. Second, the GPR does not record the extreme high and low moisture content values that the neutron probe measures. However, it does measure the general trend of the increasing and decreasing moisture content.

Analysis of the five pre-infiltration data sets indicates that the average travel time error for the GPR measurements is 1.08ns, which in general translates to an average moisture content error of ± 2%. The neutron moisture content error is ± 3 %. Both error bars are calculated by taking two standard deviations of five pre-infiltration data sets representing 95% of measurement variability. If the error bars are considered in the comparison between the GPR and neutron values then the two sets of moisture content measurements are indistinguishable.

The infiltration results indicate that GPR is capable of imaging the advancing wetting front in 2-D. The GPR image represents a smoothly varying image that maintains the general trend of the moisture content distribution as compared to the neutron probe. However, smearing occurs at the boundaries between high and low moisture content

values within the GPR image. This smearing is due to the smoothness constraint imposed within the inversion scheme, as well as the imaging limitations of the cross-borehole imaging geometry.

An advantage of GPR is that it is capable of imaging the in-situ moisture content between the boreholes whereas neutron probe measurements only provide point values. A current disadvantage of the specific GPR system that I used is its lack of field durability, which can result in erroneous travel times. Instrument problems most likely resulted in erroneous travel times for one pre-infiltration data set that then resulted in high error measurement error. In addition, the overestimation of the moisture content in the 42-day image is also probably due to system problems. However, this study has demonstrated that cross-borehole GPR can be an effective and feasible technique for characterizing the vadose zone.

8.0 RECOMMENDATIONS

The two main system components that should be improved are the fiber optic cables and the antenna connections. Both are easily damaged during necessary movement of the system and result in data acquisition and data quality problems. Increasing the field durability of the Sensors and Software cross-borehole GPR system would greatly improve the ease of data acquisition, the overall data quality, and my personal confidence in the data. Specifically, the fiber optic cables and the antenna cable connections should be made to withstand movement within the field. A durable liner surrounding the fiber optic cables would increase the field durability of the cables.

Another recommendation that would have improved the quality of data is the use of a drill rig suited for the geologic conditions of the site. The NM Bureau of Mines and

Mineral Resources drill rig that was used to drill the PVC access tubes had difficulty drilling through the gravel layer located at 1.5 m. Vertical well deviations resulted as the bit hit boulders and was deflected. In contrast, the drill rig used to take the continuous cores was not deflected by the gravels and presumably resulted in straight boreholes. Vertical borehole deviations resulted in image artifacts and thus decreased the quality of the GPR images.

REFERENCES

Aldridge, D.F. and Oldenburg, D. W., 1993. Two-dimensional tomographic inversion with finite-difference travel times. Journal of Seismic Exploration, 2:257-274.

Annan, A.P. 1999. Ground Penetrating Radar Workshop Notes. Sensors & Software Inc., Mississauga, ON.

Baker, J.M., and R.R. Allmaras. 1990. System for automating and multiplexing soil moisture measurement by time domain reflectometery. Soil Sci. Am. J., 54:1-6.

Brainard, J. R., Glass, R. J., Alumbaugh, D., Paprocki, L., Labrecque, D, J,. Yeh, T.-C. j., Baker, K, E., Rautman, C. A., 2000, The Sandia-Tech Vadose Zone Facility: Experimental Design and Data Report for Development and Testing of the Hybrid-Hydrologic-Geophysical Inverse Technique, Sandia National Laboratories publication in process.

Bregman, N.D., 1989. Crosshole seismic tomography. Geophysics. 54:2:200-215.

Chanzy, A., Tarussov, A., Judge, A., and Bonn, F. 1996. Soil water content determination using a digital ground-penetrating radar. Soil Sci. Soc. Am. J., 60:1318-1326.

CPN Company. 1984. 503 dr hydroprobe moisture depth gauge operating manual. Version 503A-230. CPN Company, Martinez, CA.

Davis, J.L. and Annan, A.P., 1989. Ground-penetrating radar for high-resolution mapping of soil and rock stratighraphy. Geophysical Prospecting, 37:531-551.

Eppstein, M. J. and Dougherty, D. E., 1998. Efficient three-dimensional data inversion: Soil characterization and moisture monitoring from cross-well ground-penetrating radar at a Vermont test site. Water Resources Research, 34:(8):1889-1900.

Greaves, R. J., Lesmes, D. P., Lee, J. M., and Toksoz, M. N., 1996. Velocity variations and water content estimated from multi-offset, ground-penetrating radar. Geophysics, 61:3:683-695.

Hasted, J.B., 1972. Liquid Water: Dielectric Properties. p. 225. *In* Water, A Comprehensive Treatment Vol. 1, The Physics and Physical Chemistry of Water. F. Franks, ED., New York: Plenum Press.

Hawley, John W., 1983. Geomorphic Evolution of Socorro Area of Rio Grande Valley. p. 13. *In* Chapin, Charles E. (ed.) Socorro Region II. Thirty-fourth Annual Field Conference. New Mexico Geological Society. Socorro, NM.

Hubbard, S. S., Rubin, Y., and Majer, E., 1997. Ground-penetrating-radar-assisted saturation and permeability estimation in bimodal systems. Water Resources Research, 33:5):971-990.

Kak, A.A., and Slaney, M.S., 1988. Principles of Computerized Tomographic Imaging. IEEE Press, New York, NY.

Meyer, P.L., 1970. Introductory Probability and Statistical Applications. Addison-Wesley Publishing Company, Reading, MA. P. 141.

Rea, J., and Knight, R. 1998. Geostatistical analysis of ground-penetrating radar data: A means of describing spatial variation in the subsurface. Water Resources Research, 34:(3):329-339.

Sharma, Prem V., 1997. Environmental and engineering geophysics. Cambridge University Press, Cambridge, U.K.

Topp, G. C., Davis, J.L. and Annan, A.P., 1980. Electromagnetic determination of soil water content: Measurements in coaxial transmission lines. Water Resources Research, 16:(3):574-582.

Topp, G. C., Davis, J.L. and Annan, A.P., 1982. Electromagnetic determination of soil water content using TDR: I Application to wetting fronts and steep gradients. Soil Sci. Soc. Am. J., 46:672-678.

van Overmeeren, R. A., Sariowan, S.V., Gehrels, J.C., 1997. Ground penetrating radar for determining volumetric soil water content; results of comparative measurements at two test sites. Journal of Hydrology, 197:316-338.

Vidale, J., 1988 Finite-difference calculation of travel times. BSSA, 78:2062-2076.

Wilson, L.G., Everett, L. G., and Cullen, S. J., 1995. Handbook of Vadose Zone Characterization and Monitoring. CRC Press, Boca Raton. FL.

Young, M. H., Fleming, J.B., Wierenga, P.J., and Warrick, A.W. 1997. Rapid laboratory calibration of time domain reflectometry using upward infiltration. Soil Sci. Soc. Am. J., 61:707-712.

APPENDIX 1

sample ID	depth(m)	silt & clay	very fine sand	fine sand	medium sand	coarse sand	very coarse sand	granules
NW1	0.30	0.7	0.8	3.2	22.8	31.5	13.9	27.0
NW2*	0.61	1.0	1.7	6.5	27.6	27.8	10.8	24.4
NW4	1.52	0.4	1.8	10.4	55.7	28.4	2.6	0.6
NW5*	1.83	3.2	2.3	5.7	16.2	20.0	15.6	36.9
NW7	3.05	1.5	12.1	46.7	37.2	1.9	0.3	0.4
NW8	3.35	15.3	3.0	3.1	21.1	42.8	12.8	1.9
NW9	3.66	2.7	7.1	30.2	35.9	12.9	2.9	8.4
NW10	4.27	3.1	7.3	43.0	36.6	7.8	2.2	0.0
NW11	4.57	3.4	18.1	61.6	14.5	1.6	0.4	0.5
NW12*	4.88	2.1	13.3	62.9	19.2	1.1	0.4	1.0
NW16	6.40	2.0	24.5	72.0	1.0	0.1	0.0	0.4
NW17	6.71	1.7	15.7	78.8	3.8	0.0	0.0	0.0
NW18	7.31	9.1	28.1	59.6	2.5	0.4	0.1	0.2
NW19	7.62	1.1	14.1	81.8	2.9	0.0	0.0	0.0
NW20	7.92	0.8	8.9	80.2	9.7	0.3	0.0	0.0
NW21	8.23	1.0	9.0	76.4	12.2	1.2	0.1	0.0
NW22	8.84	2.2	17.9	72.2	7.2	0.4	0.1	0.0
NW23	9.14	2.3	12.2	54.3	25.6	4.3	0.8	0.6
NW24	9.75	2.8	9.0	45.1	35.7	4.5	0.0	2.9
NW25*	10.36	2.0	5.5	26.1	44.3	16.3	3.3	2.4
NW27	10.97	0.4	1.4	30.3	48.9	11.6	3.0	4.4

*=following core sample is missing or has not been analyzed yet

Table A-1. Northwest core particle size analysis in percent weight

APPENDIX 2

Neutron Moisture Content Error Analysis Procedure and Calculations

Moisture content error bars were calculated by determining the error from both neutron and TDR measurements. Neutron measurements were taken in sets of three and then averaged (Table A-2). The variance of each set of measurements was calculated. Then, the overall variance was calculated by summing the individual variances and dividing by 22, the number of average measurements.

Table A-2. Neutron measurements and variance calculations

NEUTRON MEASUREMENTS AND VARIANCE CALCULATIONS				
date and time of neutron measurements		measurements	variance of each	overall variance
date	time	in sets of three	measurement set	
13-Apr	5:00 PM	5704		5913
		5693		
		5662	474.	
14-Apr	9:00 AM	4239		
		4331		
		4342	3199	
	12:45	4064		
		4117		
		4139	1486.	
	3:45	4116		
		4110		
		4139	234.	
15-Apr	9:30AM	3731		
		3927		
		3781	10372	
	12ish	3768		
		3727		
		3818	2077	
	8:15PM	3757		
		3703		
		3574	8841	
16-Apr	9:10 AM	3671		
		3568		
		3676	3716.	

	7:20 PM	3526		
		3588		
		3542	1036	
17-Apr	9:00 AM	3510		
		3581		
		3435	5330.	
19-Apr	1:30 PM	3341		
		3365		
		3328	352.	
21-Apr	2:40 PM	3289		
		3322		
		3267	766.	
22-Apr	2:30 PM	3247		
		3195		
		3257	1108	
28-Apr	2:00 PM	3038		
		3087		
		3078	680.	
30-Apr	12:50PM	8116		
		7974		
		7866	15721.	
	1:05PM	7426		
		7362		
		7343	1891	
	1:22PM	6967		
		6902		
		6886	1840.	
	1:45PM	6604		
		6425		
		6650	14130.	
	2:20PM	5997		
		6127		
		5976	6690.	
	3:05PM	5726		
		5645		
		5659	1874.	
	3:33PM	8641		
		8723		
		8665	1777.	
	4:00PM	7999		
		8313		
		8412	46494.	

Table A-2. continued

Three TDR probes were installed in order to calibrate the neutron probe. Three measurements were recorded on each probe for each sampling interval (Table A-3). The TDR probe measures the dielectric constant (K). For each probe the three dielectric measurements were averaged and then the average dielectric constant was converted to moisture content via equation 8. Three moisture contents for each sampling interval were then averaged. This average TDR moisture content was then related to the corresponding average neutron value.

TABLE A-3. TDR MEASUREMENTS			
date	4/13		
probe #	1	2	3
k	8.25	9.05	6.56
k	7.91	8.98	6.56
k	8.27	9.01	6.57
avg k	8.14	9.01	6.56
moisture content	0.077	0.089	0.056
avg moisture content	0.074		
date	4/14		
probe #	1	2	3
k	5.95	6.22	5.22
k	5.88	6.24	5.17
k	5.98	6.3	5.27
avg k	5.94	6.25	5.22
moisture content	0.047	0.052	0.038
avg moisture content	0.046		
date	4/14		
probe #	1	2	3
k	5.55	6.09	5.13
k	5.66	6.25	5.07
k	5.55	6.29	5.11
avg k	5.59	6.21	5.10
moisture content	0.043	0.051	0.036
avg moisture content	0.0433133		
date	4/14		
probe #	1	2	3
k	5.31	5.89	5.04
k	5.5	5.88	5.04
k	5.38	5.99	5.15
avg k	5.40	5.92	5.08
moisture content	0.040	0.047	0.036
avg moisture content	0.041		

Table A-3. continued

TDR MEASUREMENTS			
date	4/15		
probe #	1	2	3
k	5.05	5.51	4.78
k	5.09	5.52	4.8
k	5.07	5.41	4.78
avg k	5.07	5.48	4.79
moisture content	0.036	0.041	0.031
avg moisture content	0.036		
date	4/15		
probe #	1	2	3
k	4.99	5.33	4.66
k	4.97	5.5	4.72
k	4.98	5.27	4.78
avg k	4.98	5.37	4.72
moisture content	0.034	0.040	0.030
avg moisture content	0.035		
date	4/15		
probe #	1	2	3
k	4.78	5.25	4.88
k	4.9	5.31	4.58
k	4.85	5.37	4.64
avg k	4.84	5.31	4.7
moisture content	0.033	0.039	0.030
avg moisture content	0.03		
date	4/16		
probe #	1	2	3
k	4.45	5.19	4.6
k	4.78	5.13	4.58
k	4.77	5.09	4.7
avg k	4.67	5.14	4.63
moisture content	0.030	0.037	0.030
avg moisture content	0.032		
date	4/16		
probe #	1	2	3
k	4.55	5.03	4.58
k	4.57	5.13	4.57
k	4.58	5.13	4.48
avg k	4.57	5.10	4.54
moisture content	0.029	0.036	0.028
avg moisture content	0.031		

Table A-3. continued

TDR MEASUREMENTS			
date	4/17		
probe #	1	2	3
k	4.47	4.96	4.55
k	4.49	5.06	4.5
k	4.26	5.09	4.5
avg k	4.41	5.04	4.52
moisture content	0.027	0.035	0.028
avg moisture content	0.030		
date	4/19		
probe #	1	2	3
k	4.08	4.69	4.18
k	4.31	4.57	4.32
k	3.89	4.7	4.34
avg k	4.09	4.65	4.28
moisture content	0.022	0.030	0.025
avg moisture content	0.026		
date	4/21		
probe #	1	2	3
k	4.03	4.49	4.2
k	4.21	4.44	4.15
k	3.88	4.58	4.2
avg k	4.04	4.50	4.18
moisture content	0.022	0.028	0.024
avg moisture content	0.024		
date	4/22		
probe #	1	2	3
k	3.89	4.41	4.13
k	3.94	4.59	4
k	3.97	4.47	4.05
avg k	3.93	4.49	4.06
moisture content	0.020	0.028	0.022
avg moisture content	0.023		
date	4/28		
probe #	1	2	3
k	3.94	4.32	3.94
k	3.74	4.24	3.97
k	3.73	4.28	3.98
avg k	3.80	4.28	3.96
moisture content	0.018	0.025	0.021
avg moisture content	0.021		

Table A-3. continued

TDR MEASUREMENTS			
date	4/30		
probe #	1	2	3
k	14.98	14.56	9.72
k	14.83	14.45	9.82
k	13.41	14.29	9.7
avg k	14.41	14.43	9.75
moisture content	0.163	0.163	0.010
avg moisture content	0.142		
date	4/30		
probe #	1	2	3
k	13.11	12.92	8.5
k	13.2	12.75	8.38
k	13.07	12.71	8.46
avg k	13.13	12.79	8.45
moisture content	0.145	0.141	0.082
avg moisture content	0.12		
date	4/30		
probe #	1	2	3
k	11.41	12.29	8.06
k	11.52	12.21	7.97
k	10.91	12.05	7.92
avg k	11.28	12.18	7.98
moisture content	0.120	0.132	0.075
avg moisture content	0.109		
date	4/30		
probe #	1	2	3
k	10.99	11.48	7.35
k	10.46	11	7.37
k	11.02	11.12	7.54
avg k	10.82	11.2	7.42
moisture content	0.114	0.119	0.068
avg moisture content	0.100		
date	4/30		
probe #	1	2	3
k	9.67	9.98	6.93
k	10.22	10.28	6.77
k	9.46	10.12	6.83
avg k	9.78	10.13	6.84
moisture content	0.010	0.10	0.060
avg moisture content	0.088		

Table A-3. continued

TDR MEASUREMENTS			
date	4/30		
probe #	1	2	3
k	9.02	9.14	6.63
k	8.92	9.32	6.51
k	8.94	9.42	6.63
avg k	8.96	9.29	6.59
moisture content	0.089	0.093	0.056
avg moisture content	0.079		
date	4/30		
probe #	1	2	3
k	14.63	11.73	10.9
k	15.81	12.6	10.97
k	15.15	13.32	11.21
avg k	15.20	12.55	11.03
moisture content	0.173	0.137	0.117
avg moisture content	0.142		
date	4/30		
probe #	1	2	3
k	12.86	13.79	10.72
k	14.04	13.56	10.77
k	14.93	14.16	10.83
avg k	13.94	13.84	10.77
moisture content	0.156	0.155	0.113
avg moisture content	0.141		

A regression analysis was calculated for TDR-determined moisture contents versus average neutron values (Figure 18) and the resulting statistics from this analysis are presented in Table A-4a-c.

Table A-4a-c. REGRESSION ANALYSIS SUMMARY OUTPUT

Table A-4a.

Regression Statistics	
Multiple R	0.939240301
R Square	0.882172342
Adjusted R Square	0.881571181
Standard Error	0.01512296
Observations	198

Table A-4b.

ANOVA					
	df	*SS*	*MS*	*F*	*Significance F*
Regression	1	0.335610	0.33561	1467.45	5.81325E-93
Residual	196	0.044825	0.00022		
Total	197	0.380436			

Table A-4c.

	Intercept	X Variable 1
Coefficients	-0.052696283	0.3788785
Standard Error	0.003178964	0.0098905
t Stat	*-16.576557*	*38.307263*
P-value	3.76142E-39	5.813E-93
Lower 95%	-0.058965644	0.3593730
Upper 95%	-0.046426923	0.398384
Lower 95.0%	-0.058965644	0.3593730
Upper 95.0%	-0.046426923	0.398384

Procedure for Calculating Variance of Moisture Content (Y)

As already established in section 3.3, $Y=\Upsilon + b\,(x-\chi) + \varepsilon$ (10)

where Υ is the mean moisture content, b is the slope of the regression line, χ is the mean average neutron count ratio, x is specific neutron count ratio value, and ε is the measurement error.

The variance of Y is then:

$\text{var}(Y) = \text{var}(\Upsilon) + \text{var}(b\,(x-\chi)) + \text{var}(\varepsilon)$

which is equivalent to:

$\text{var}(Y) \cong s^2/n + \text{var}(b\,(x-\chi)) + s^2$

where n is the number of TDR measurements, s^2 is the variance of the error, and var (x) is the variance of the neutron measurements.

Further approximations are calculated by propagation of error (Meyer, 1970) as follows:

$\text{var}(b\,(x-\chi)) \cong \text{var}(b)\,(x-\chi)^2 + b^2\,\text{var}(x-\chi) \cong s^2/\,9\,\Sigma^{n}_{i=1}\,(x_I-\chi)^2 * \,(x_I-\chi)^2 + b^2\,\text{var}(x-\chi)$

In addition, var $(x-\chi)$ can be approximated by:

$\text{var}(x-\chi) \cong \text{var}(x) + \text{var}(\chi) \cong \text{var}(x) + \text{var}(x)/m$

where m is the number of average neutron measurements

Putting all the approximations together, the var (Y) becomes:

$\text{var}(Y) = s^2/n + s^2 + s^2(x-\chi)^2/9\Sigma(x_I-\chi)^2 + b^2(\text{var}(x) + \text{var}(x)/m)$ (11)

Equation 11 can be rearranged and subdivided into 4 subsections for ease in solving.

$\text{var}(Y) = s^2 + s^2/n + s^2(x-\chi)^2/9\Sigma(x_I-\chi)^2 + b^2(\text{var}(x) + \text{var}(x)/m)$
(1) (2) (3) (4)

Solving for (1): $s^2 = SS*/df* = 0.044825969/\,196 = 2.287 \times 10^{-4}$

* both SS and df were obtained from table 3

Solving for (2): $s^2/n = 2.287 \times 10^{-4}/198 = 1.155 \times 10^{-6}$

Solving for (3): $s^2 *(x-\chi)^2/9\Sigma(x_I-\chi)^2 = (2.287 \times 10^{-4} (0.0521508 - 0.30249)^2)/ (9 * (0.259773)) = 4.6923 \times 10^{-6}$

Where b^2 is obtained from Table A-3c and x was chosen as 0.30249 to represent worst case (where large variability in measurements was observed in Figure 18).

Solving for (4): $b^2(\text{var}(x) + \text{var}(x)/m) = (0.3789)^2 * (2.14244 \times 10^{-5} + 9.73837 \times 10^{-7}) = 3.2156 \times 10^{-6}$

Since the var (x) = var counts/ (standard count)^2 = 5913.318182/(16613.5)^2 = 2.14244×10^{-5} and var (x)/m = $2.14244 \times 10^{-5} / 22 = 9.73837 \times 10^{-7}$

Now adding up all the subsections yields the following:

var (Y) = $2.287 \times 10^{-4} + 1.155 \times 10^{-6} + 4.6923 \times 10^{-6} + 3.2156 \times 10^{-6} = 2.3776 \times 10^{-4}$

Therefore one standard deviation of Y is 0.0154 and two standard deviations is 0.03 or 3% moisture content

APPENDIX 3

Neutron Probe Operating and Downloading Procedure

Performing the Standard Count

Attach the cable to both ends of the probe

Place the probe on top of the tube of the standard count barrel.

Lower the probe to the first silver stop

Press the STD key

Press step until the display asks "NEW STD?"

Press the Enter key and step away from the probe

Wait for S#### (S followed by a four digit number) to appear and for the beeping to stop.

Once the beeping has stopped, press the step button to step through the screen display mode.

The following will be displayed as you step through:

P ####- indicates the previous standard count
S ####- indicates the new standard count
Chi #.##- indicates the chi squared ratio of the new count

Write down all three of these numbers in the yellow book

If the Chi number is out of the range 0.75 to 1.25, repeat the standard count

Press Enter to save the new standard count

Selecting units

Select the units by pressing the Units key

Step through the options by pressing the Step key

To collect the raw data, press enter when "MUNT CNT" appears on the display.

Press the time key to select the sample time.

Step through the options by pressing the step key.

When "Time32" appears on the display, press the Enter key.

Setting the format

Every time we take data we want to clear the previous data that has already been downloaded. Clearing previous data is accomplished by setting the format.

To set the format, press the FMT key

It will display a rec number, press step to continue to the next parameter

Then a key data number will appear (Key data is for other parameters to be entered), just hit step.

Then depths will appear, we want 46 depths. To change depths just press the number of depths you want. Then press step.

The display will read "SET FMT?". Press Enter.

Taking data

Press log and it will give an ID number, push the number you want for the designated hole. ie 1 for the ctr access tube. Look in the yellow number 1 book for the order and identification of access tubes.

Press STEP and it will display K 1 0, press STEP.

The next display will show TAKE 46. Lower the probe to the cable stop labeled 46 and press START. If you forget to lower the probe before taking your first measurement, press CLEAR and start again.

The display will read COUNT 46. The probe is taking a measurement and at shallow depths you should keep a distance from the probe. Then it will beep and display M46.####. The number, #### is the raw count for that particular depth.

Press STEP to take a reading at the next depth. It will display TAKE 45. Lower the probe one stop and press START.

Continue this process until you either reach the bottom of the hole or you take the last depth, TAKE 1.

If you reach the bottom of the hole and there are several depths still to be taken, press STEP all the way through past take one.

Now if you've taken the last depth or you've pressed step to get there, the display will say, "DATA OK?" Press ENTER to save the data.
Then the display will read READY. It is ready to take measurements on another borehole.

Pull up the cable until the probe latches with the top and move the probe to another borehole.

Start the process over again by pressing log and repeat the procedure that was previously written.

Once all the boreholes are logged, bring up the probe.

Downloading Data to the Computer and Processing

Once data is taken hook up the probe to the computer by a cable in the data acquisition building.

In the computer go the directory c:/aadir/hhgit/neutron/neuinf

Type 123dump

Enter 2 at the com port prompt

Enter 2 for the 1200 baud rate

Enter the date using backslashes (ie 01/3/99)

Enter the path and file name based on the date, i.e., c/aadir/hhgit/ neutron/neuinf/n052798.csv for neutron probe data on May 27, 1998.

Enter N for hard copy (to avoid printing the data)

Press enter and data should start downloading

Press Y for data okay

Disconnect the cable

Then run the neutron data reduction program for processing the data

Go to the shortcut on the desktop called Neutron.exe, double click

Under file enter data file to be processed and then press RUN.

Next go the shortcut entitled Moisture.exe, double click, enter file name, enter standard count and press run.

APPENDIX 4

Four GPR Pre-Infiltration Ray Density Images

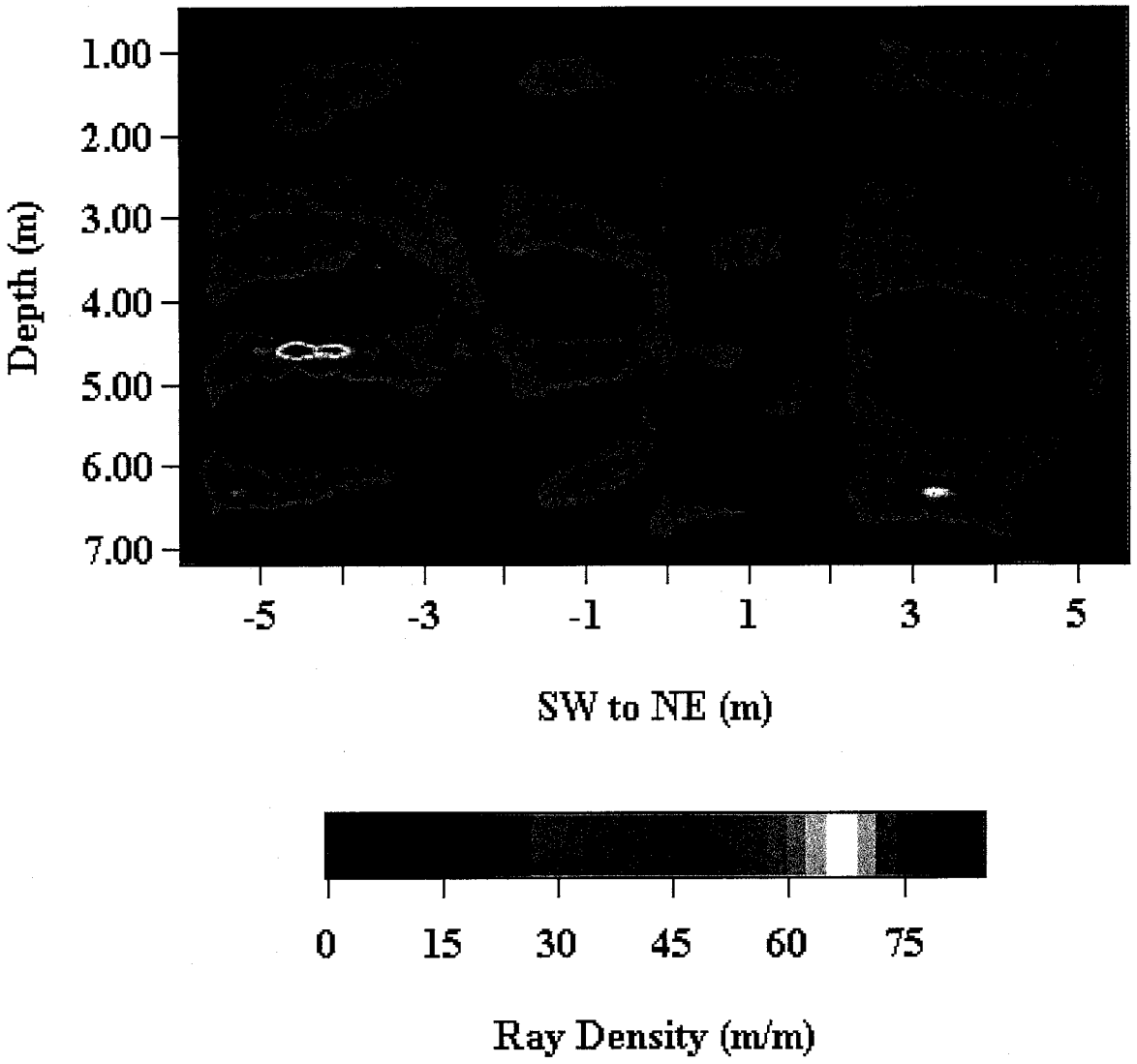

Figure A.1. Ray density image for GPR pre-infiltration data set taken on 1/22/99

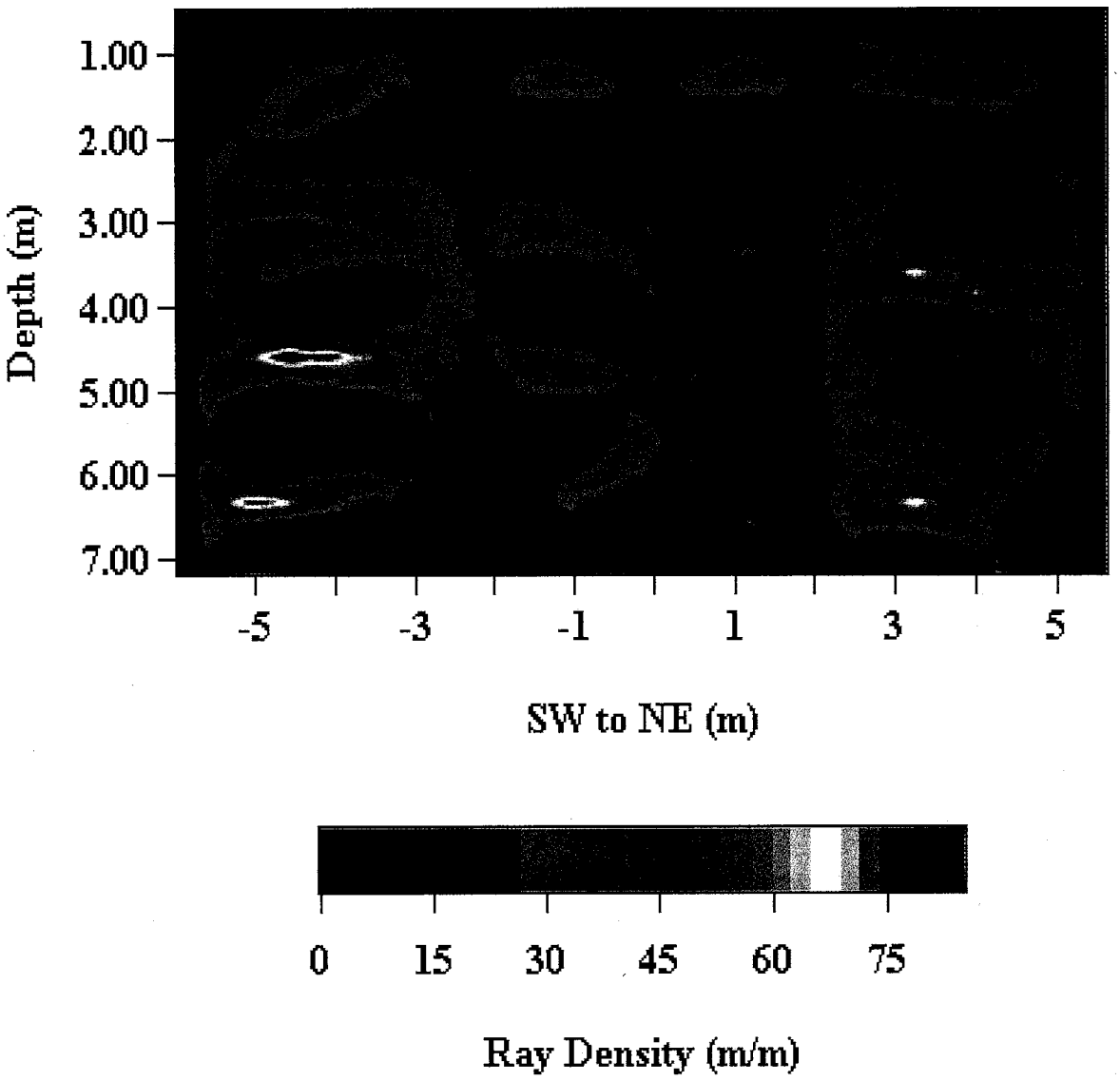

Figure A.2. Ray density image for GPR pre-infiltration data set taken on 2/1/99

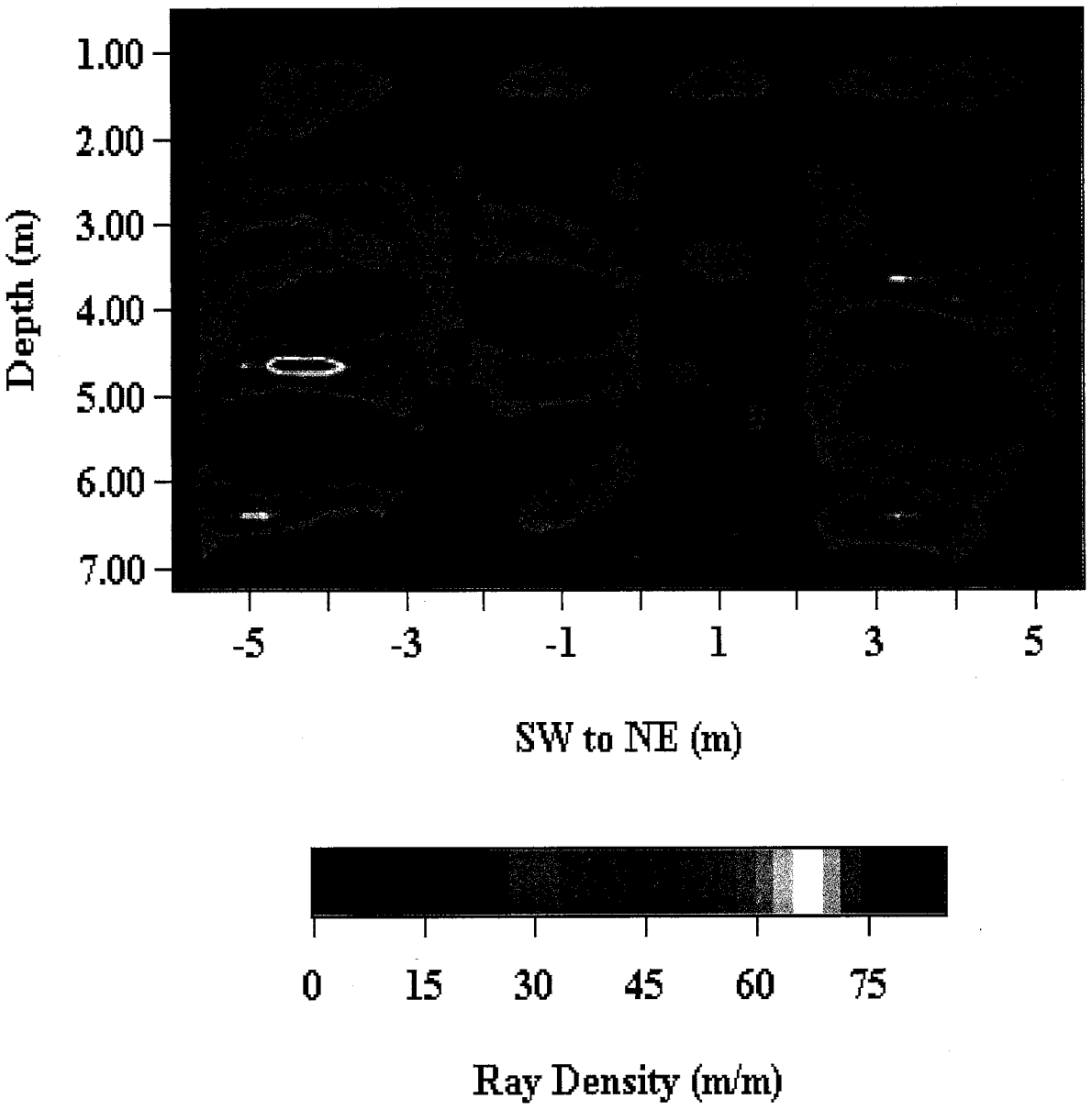

Figure A.3. Ray density image for GPR pre-infiltration data set taken on 2/11/99

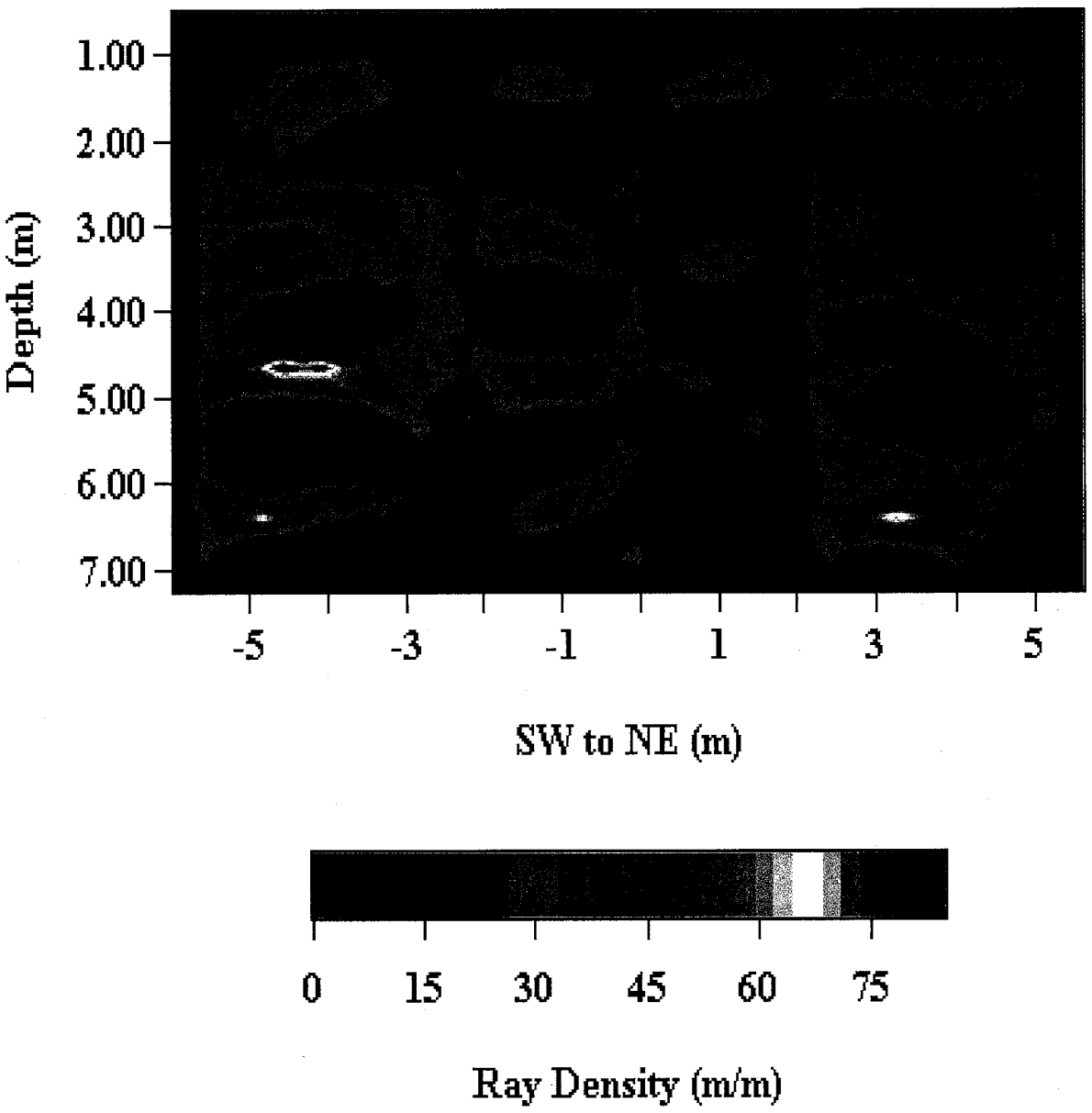

Figure A.4. Ray density image for GPR pre-infiltration date set taken on 2/18/99

APPENDIX 5

GPR Moisture Content Images: Mean Pre-Infiltration Image and Seven Infiltration Images Processed without a Time Shift

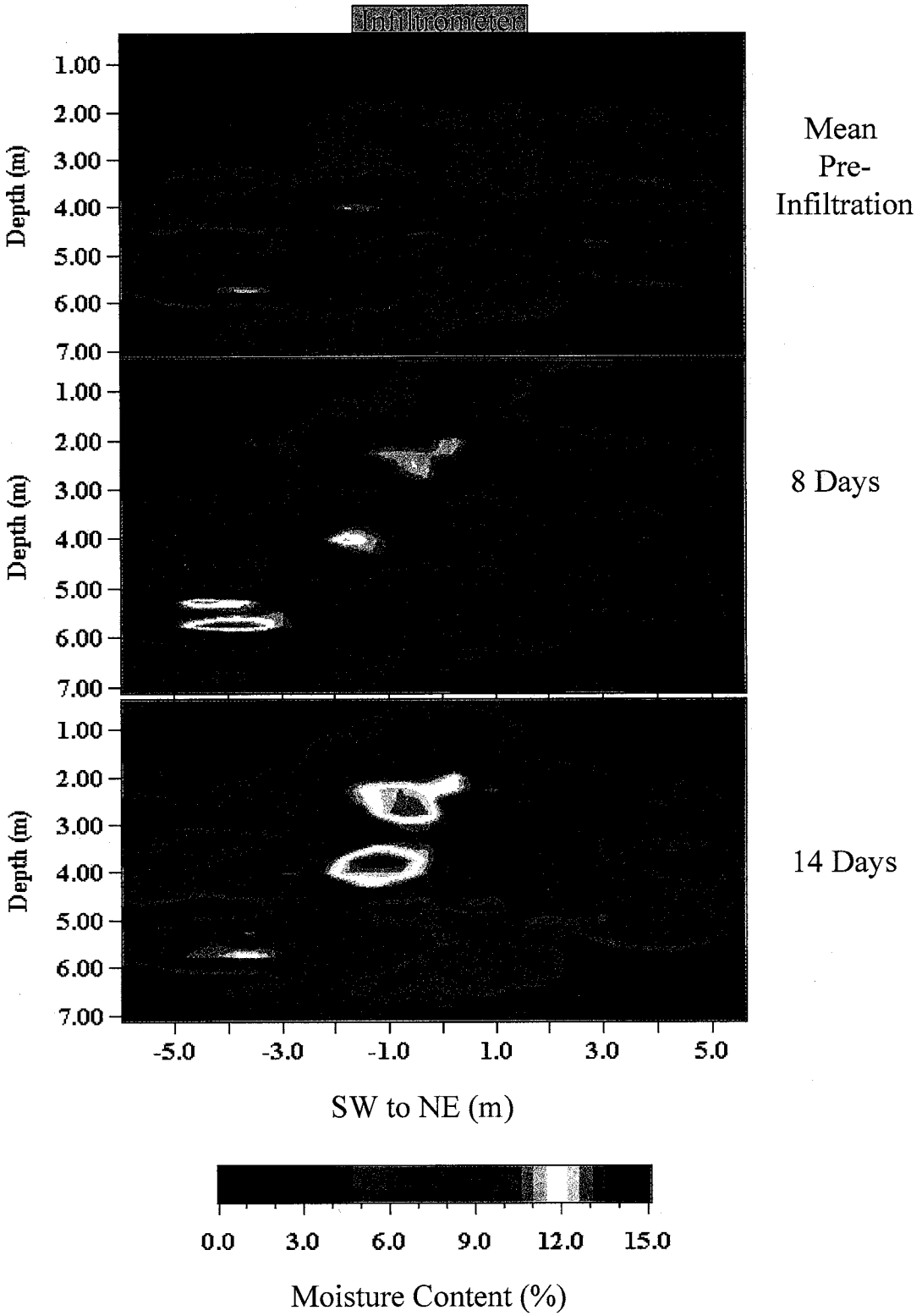

Figure A.5a-c. GPR moisture content images: pre-infiltration to 14 days after infiltration began (no time shift applied)

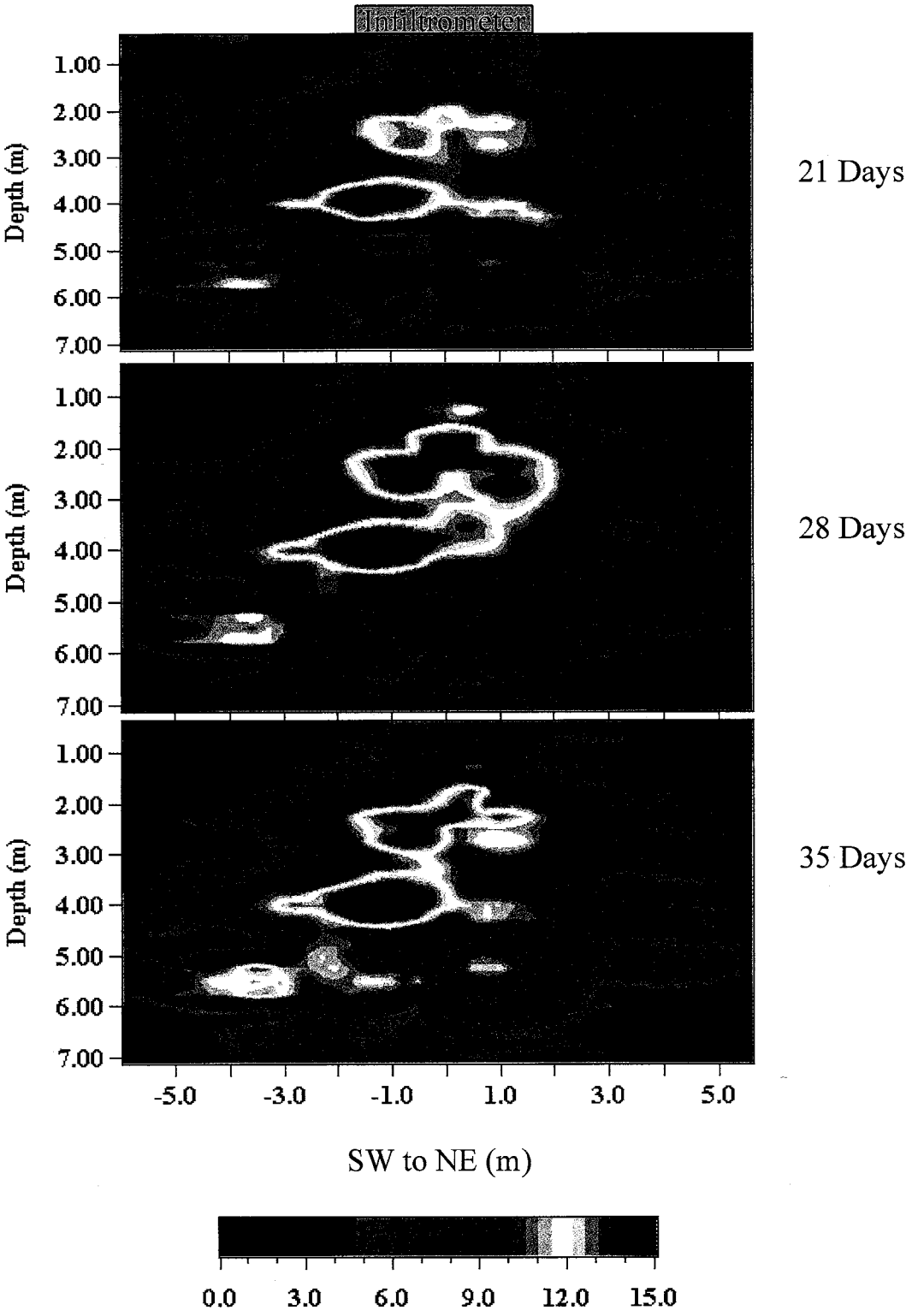

Figure A.5d-f. GPR moisture content images:21- 35 days after infiltration began (no time shift applied)

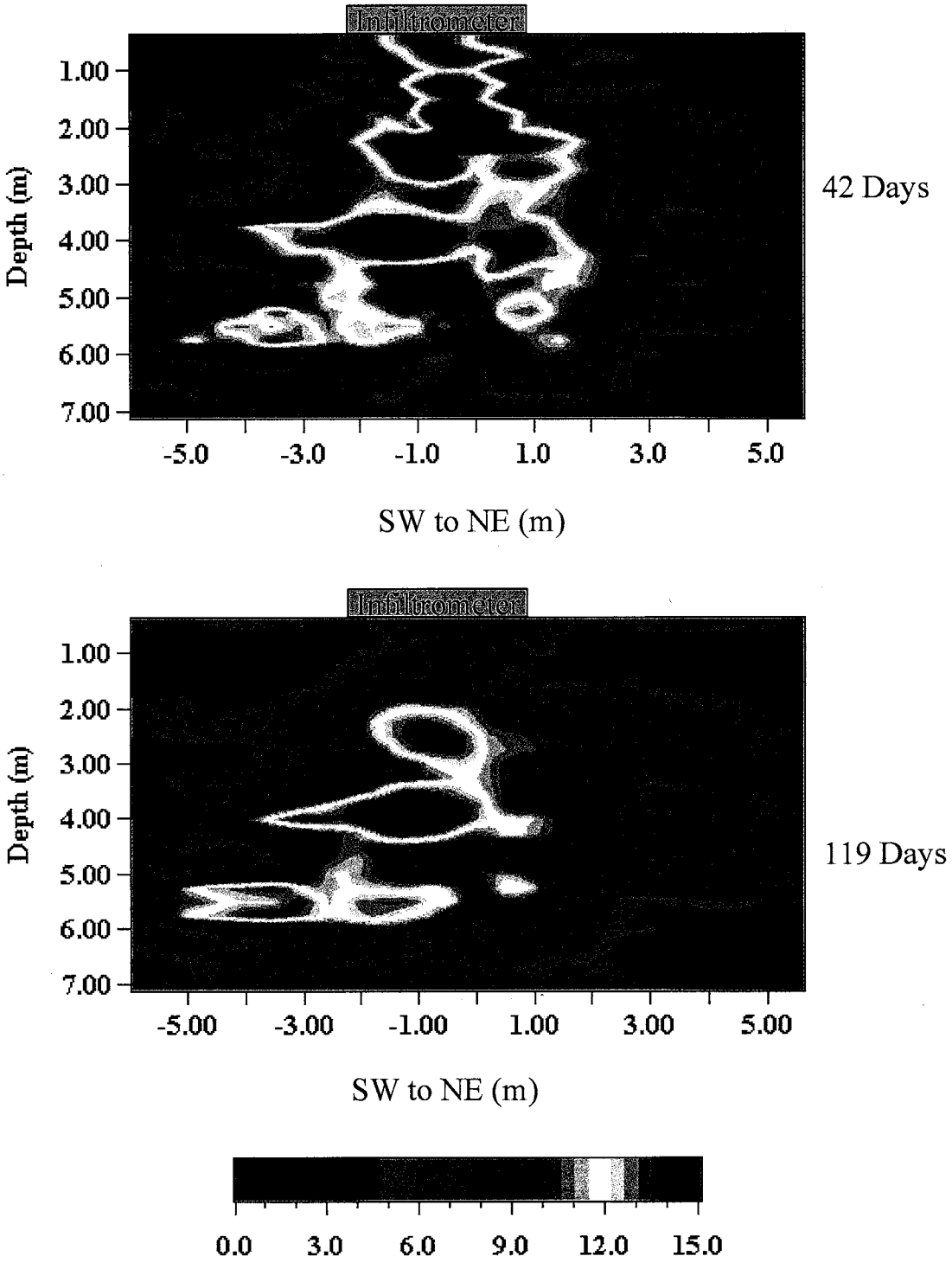

Figure A.5g-h. GPR moisture content images: 42 and 119 days after infiltration began (no time shift applied)

APPENDIX 6

Normalized GPR Moisture Content Infiltration Images Processed without a Time Shift

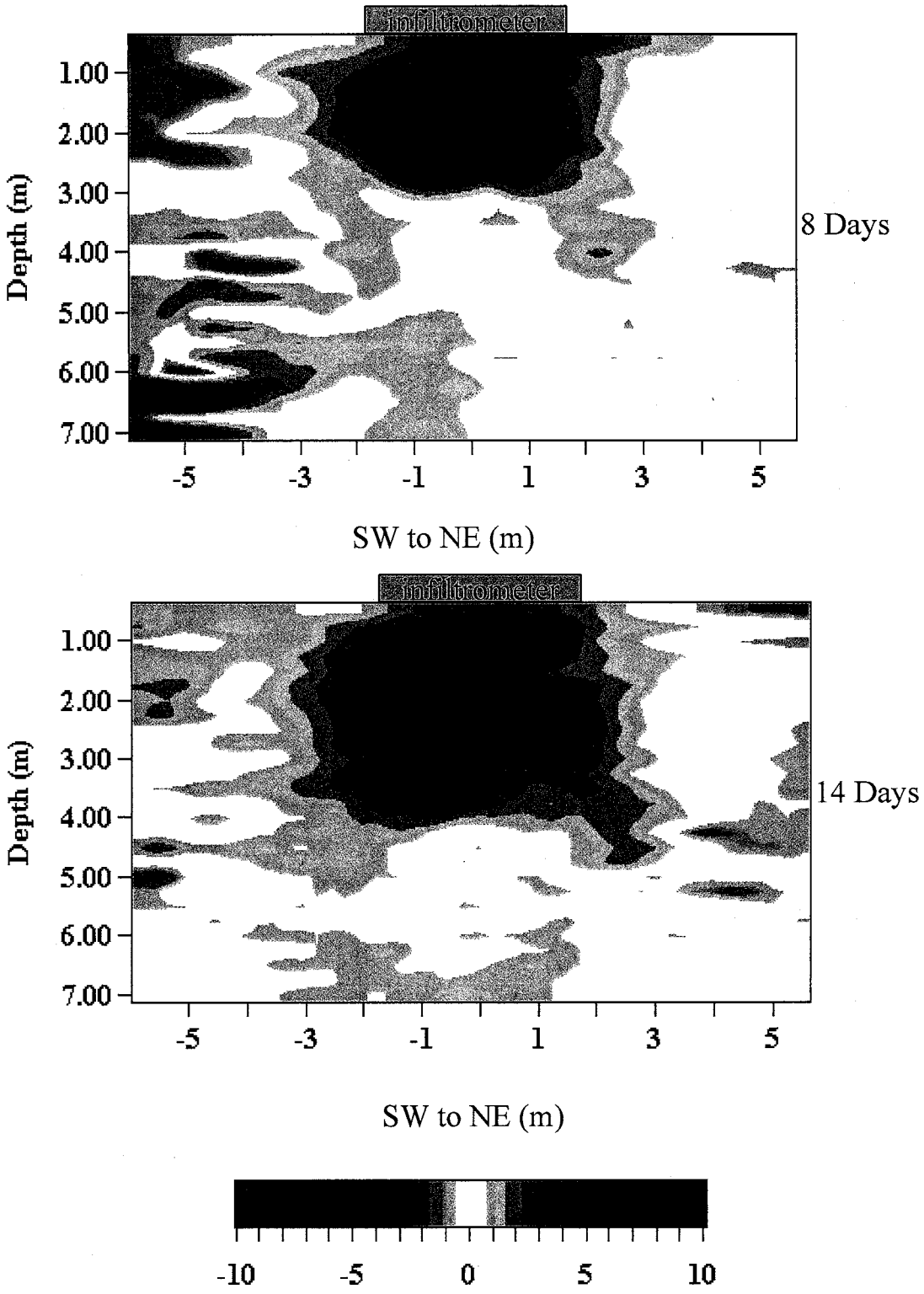

Figure A.6a-b. GPR normalized moisture content images 8 and 14 days after infiltration began (no time shift applied)

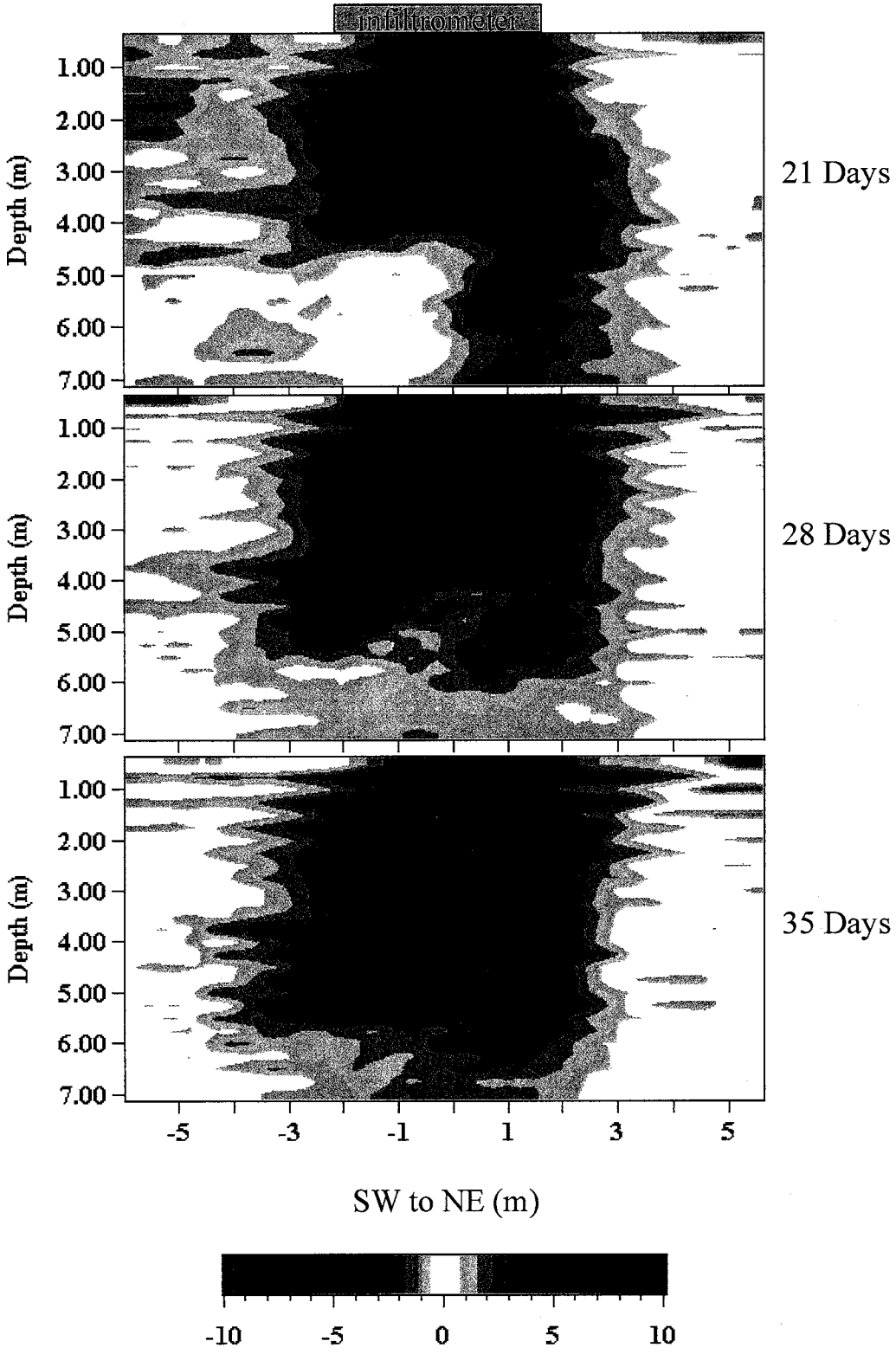

Figure A.6c-e. GPR normalized moisture content images 21-35 days after infiltration began (no time shift applied)

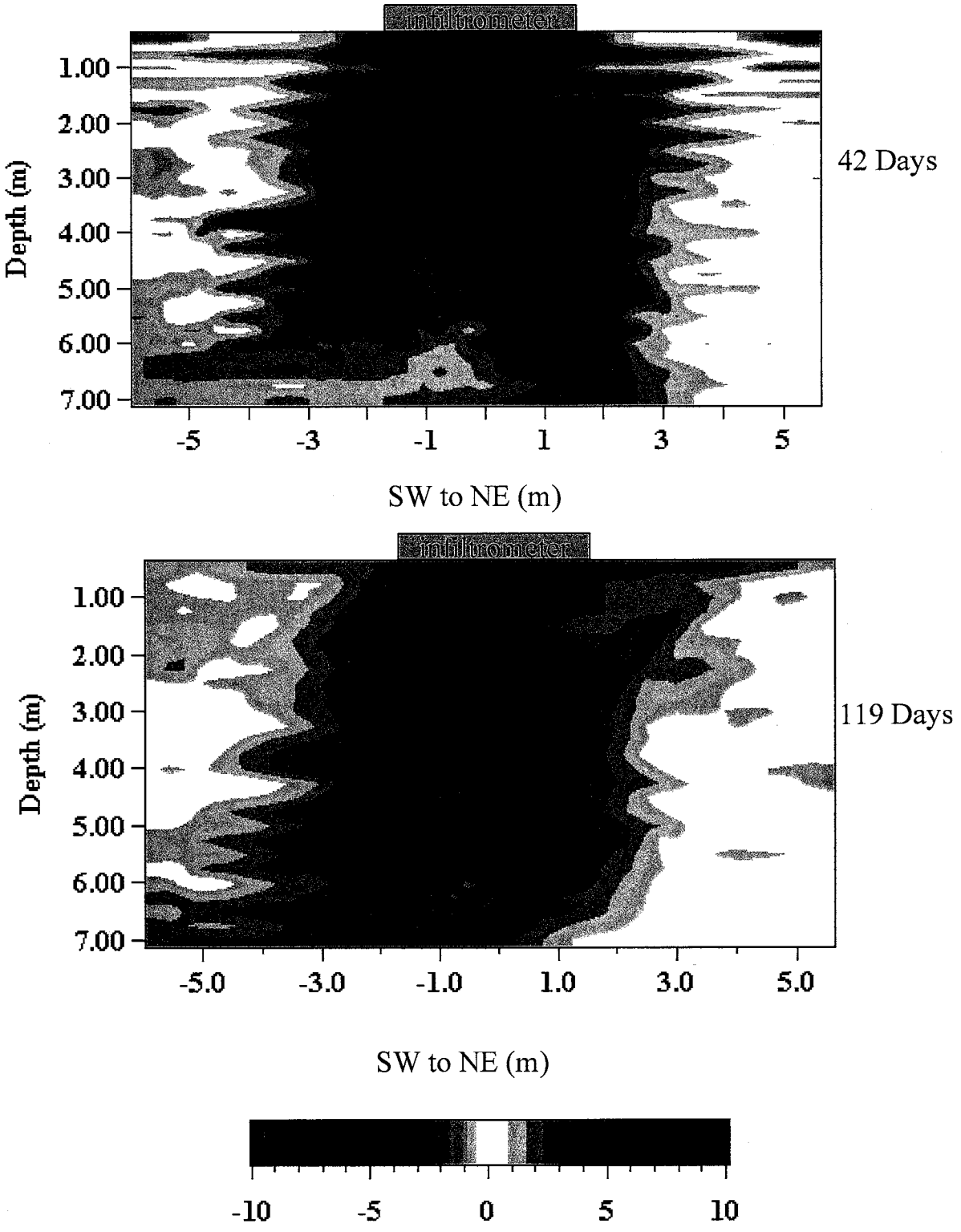

Figure A.6f-g. GPR normalized moisture content images 35 and 42 days after infiltration began (no time shift applied)

This thesis is accepted on behalf of the faculty

of the institute by the following committee:

Robert A. Bowman

Advisor

Brian J. C. L. McPherson

Harold James Tal

David L Alumbaugh

25 February 2000

Date